

Universität Hamburg
DER FORSCHUNG | DER LEHRE | DER BILDUNG

On the origin and survival of circumbinary planets in Post Common Envelope Binaries

Dissertation
zur Erlangung des Doktorgrades
an der Fakultät für Mathematik, Informatik und Naturwissenschaften
Fachbereich Physik
der Universität Hamburg

vorgelegt von

Deepali

Hamburg
2026

Gutachter/innen der Dissertation:	Prof. Dr. Robi Banerjee Prof. Dominik R. G. Schleicher
Zusammensetzung der Prüfungskommission:	Prof. Dr. Robi Banerjee Prof. Dominik R. G. Schleicher Prof. Dr. Peter Hauschildt Prof. Dr. Thomas Kupfer Prof. Dr. Jochen Liske
Vorsitzende/r der Püfungskommission:	Prof. Dr. Jochen Liske
Datum der Disputation:	16/09/2026
Vorsitzender des Fach-Promotionsausschusses PHYSIK:	Prof. Dr. Johannes Haller
Leiter des Fachbereichs PHYSIK:	Prof. Dr. Markus Drescher
Dekan der Fakultät MIN:	Prof. Dr.-Ing. Norbert Ritter

Declaration on oath

I hereby declare and affirm that this doctoral dissertation is my own work and that I have not used any aids and sources other than those indicated.

If electronic resources based on generative artificial intelligence (gAI) were used in the course of writing this dissertation, I confirm that my own work was the main and value-adding contribution and that complete documentation of all resources used is available in accordance with good scientific practice. I am responsible for any erroneous or distorted content, incorrect references, violations of data protection and copyright law or plagiarism that may have been generated by the gAI.

Place, Date: HAMBURG 10.07.2026

Signature of the doctoral candidate

Contents

Acknowledgements **iv**

Abstract **v**

Zusammenfassung **vi**

1 Introduction **1**
1.1 Observations of exoplanets orbiting binary stars . . . 1
1.1.1 Eclipse Timing Variations . . . 1
1.2 Theoretical Background . . . 3
1.2.1 Single Star Evolution . . . 3
1.2.2 Evolution with a close companion . . . 5
1.2.3 Common Envelope Evolution (CEE) . . . 6
1.3 Orbital evolution during host star mass loss . . . 13
1.4 Circumbinary discs post CE . . . 17

2 Methods **21**
2.1 Simulation Setup . . . 21
2.2 Initial Conditions . . . 21
2.3 Simulation setup for Circumbinary disc . . . 24

3 Impact of CEE on first generation CBP orbits **27**
3.1 Aim . . . 27
3.2 Parameter study . . . 27
3.3 Results . . . 29
3.3.1 Varying initial radial and rotational support to CE . . . 40
3.4 Summary and Conclusions . . . 43

4 Properties of Post-CE Circumbinary Discs **44**
4.1 Aim . . . 44
4.2 Parameter study . . . 44
4.3 Results . . . 46
4.4 Summary and Conclusions . . . 57

5 Conclusions and Outlook **58**

A Choice of frame of reference **60**
A.1 For orbital properties of planets . . . 60
A.2 For properties of post-CE structures . . . 62

B Circumbinary discs **64**
B.1 Hot ambient medium . . . 64
B.2 Power law indices . . . 64

Bibliography **66**

Acknowledgements

The past few years have been a huge learning curve for me, both personally and professionally. I am indebted to more people than I can name here.

First and foremost, I would like to thank Prof. Robi Banerjee for giving me the opportunity to pursue PhD under his guidance. I am grateful for his support, patience and feedback throughout this journey. I am thankful to Prof. Dominik Schleicher for his guidance, support and insightful discussions. I want to thank Prof. Paul Ricker for sharing his enthusiasm and deep knowledge on the subject of Common Envelopes and Flash code. Many thanks to Christiane, whose simulation setup helped me accelerate the development of my model in Flash code.

I greatly appreciate the opportunity to have scientific discussions with Prof. Dimitri Veras, Dr. Luke Chamandy, Prof. Ondřej Pejcha, Dr. Marcel Völschow and Prof. Rebecca Martin over the past years.

Though it is impossible to convey in words, my heartfelt thanks to my parents and brother for their immense love, encouragement and their sacrifices which made this milestone possible. To my beloved partner and biggest cheerleader Poshak, your love, patience and unconditional acceptance have been my biggest strength through all these years. I am forever grateful for you. To my grandparents who filled my life with happiness, love and life lessons, I miss you every day. A very special thanks to my dearest friends Garima, Jayatee, Akisha, Naman and Ujwal who have always been there for me through the highs and lows.

Thanks to my colleagues and friends from observatory, Raghav, Vanesa, Felipe, Carolina, Jorinde, Lovorka, Pia, Subarna, Giulia, Marco, Philipp, Diego, Pranjal and Paulo, for the scientific discussions, the laughs and the conversations. Last but definitely not least, I am thankful for the kind and supportive friends I've made here in Hamburg from outside of academia, who made my stay memorable and helped me adjust to the rhythms of a new country and culture.

I gratefully acknowledge the funding by the Hamburg State Graduate Funding Program (HmbNFG) to support the completion of my studies.

Abstract

With around 6300 extra solar planets observed till date, only a handful of these exist around binary stars. A few circumbinary planets have been proposed to orbit tight binaries including a compact object and a main sequence star, using eclipse timing variations. Existence of such planetary systems poses the question of whether these planets can survive the common envelope (CE) phase of host binary or they form out of the bound material via gravitational instability, after the violent mass ejection phase.

Close binaries with an evolved star can form through the CE channel during binary star evolution. As the primary fills its roche lobe, it starts to transfer mass onto the companion. In case of unstable mass transfer, companion is engulfed into primary's envelope. Due to gravitational drag effects, companion spirals deeper into the shared envelope leading to ejection of envelope gas. The timescale and amount of ejection is still an open problem, which are governed by several physical processes.

This thesis explores the two proposed scenarios behind existence of circumbinary planets in post-CE binaries using 3D hydrodynamic simulations of mass ejection events. The first generation planets on initially circular orbits end up in wider and eccentric orbits in case of instantaneous and intermediate mass loss events. Despite the planets being embedded in asymmetric and extended envelope during mass loss phase, they are ejected when mass enclosed within the orbits is reduced by half or more, in case of instantaneous mass loss. During the same CE event, each planet in the system responds to the change of mass depending on its orbital separation at the time of the ejection.

To explore the possibility of second generation planet formation, properties of post ejection structures are studied for two ideal thermodynamic scenarios. In the case of no cooling (adiabatic equation of state), post ejection remnant is non-spherical, pressure supported and the gas is in sub keplerian motion. For instantaneous cooling, remnant material flattens into a rotation supported disk with steep surface density profiles and spiral arm features. In the ideal scenario of globally isothermal simulations, the disks appear unstable to gravitational instability indicating the possibility of formation of clumps.

Zusammenfassung

Von den bislang beobachteten rund 6300 Exoplaneten umkreisen nur wenige Doppelsterne. Anhand von Eclipse Timing Variations wurde vermutet, dass einige wenige zirkumbinäre Planeten enge Doppelsterne umkreisen, die aus einem kompakten Objekt und einem Hauptreihenstern bestehen. Die Existenz solcher Planetensysteme wirft die Frage auf, ob diese Planeten die Phase der gemeinsamen Hülle (Common Envelope, CE) ihres Muttersystems überstehen können oder ob sie sich nach der Phase heftiger Massenauswürfe aus dem gebundenen Material durch gravitative Instabilität bilden.

Eng beieinanderliegende Doppelsterne mit einem entwickelten Stern können sich im Verlauf der Entwicklung eines Doppelsternsystems über den CE-Kanal bilden. Wenn der Hauptstern seinen Roche-Lappen füllt, beginnt er, Masse auf den Begleitstern zu übertragen. Bei einem instabilen Massentransfer wird der Begleitstern in die Hülle des Hauptsterns eingebettet. Aufgrund von Gravitationswiderstandseffekten spiralisiert der Begleitstern tiefer in die gemeinsame Hülle hinein, was zum Ausstoß von Hüllengas führt. Die Zeitskala und das Ausmaß des Ausstoßes sind nach wie vor ein offenes Problem, das von mehreren physikalischen Prozessen bestimmt wird.

In dieser Arbeit werden die beiden vorgeschlagenen Szenarien für die Existenz von um ein Doppelsternsystem kreisenden Planeten in Post-CE-Doppelsternsystemen anhand von 3D-Hydrodynamik-Simulationen von Massenausstoßereignissen untersucht. Planeten der ersten Generation auf ursprünglich kreisförmigen Umlaufbahnen gelangen im Falle von sofortigen und intermediären Massenverlustereignissen in weiter ausgedehnte und exzentrische Umlaufbahnen. Obwohl die Planeten während der Massenverlustphase in eine asymmetrische und ausgedehnte Hülle eingebettet sind, werden sie im Falle eines sofortigen Massenverlusts ausgestoßen, sobald die in ihren Umlaufbahnen eingeschlossene Masse um die Hälfte oder mehr abnimmt. Während desselben CE-Ereignisses reagiert jeder Planet im System auf die Massenänderung in Abhängigkeit von seinem Abstand zum anderen Planeten zum Zeitpunkt des Ausstoßes.

Um die Möglichkeit der Planetenentstehung der zweiten Generation zu untersuchen, werden die Eigenschaften von Strukturen nach dem Ausstoß für zwei ideale thermodynamische Szenarien untersucht. Im Fall ohne Abkühlung (adiabatische Zustandsgleichung) ist der nach dem Ausstoß verbleibende Rest nicht-sphärisch, das Gas ist druckgest ützt und in subkeplerischer Bewegung. Bei sofortiger Abkühlung flacht das verbleibende Material zu einer durch Rotation gestützten Scheibe mit steilen Oberflächendichteprofilen und spiralförmigen Strukturen ab. Im idealen Szenario global isothermer Simulationen die Scheiben scheinen hinsichtlich gravitativer Instabilitäten leicht instabil zu sein. Dies deutet auf die Möglichkeit der Klumpenbildung hin.

Chapter 1

Introduction

First detection of planets outside our solar system dates back to 1992 (Wolszczan and Frail [1992]), where two terrestrial planets were found to orbit around a millisecond pulsar PSR1257+12. Unlike our sun, the host star is an evolved and rapidly rotating neutron star. These planets were found at close orbital separations of 0.47 AU and 0.36 AU in approximately circular orbits. Mayor and Queloz [1995] presented the confirmed detection of a Jupiter-like planet orbiting a solar-type star 51 Pegasi at orbital distance of 0.05 AU. Since then around 6300 exoplanets[1] have been confirmed at the time of writing this thesis. The diversity of planetary systems is astonishing, be it in the mass and orbital properties of the planets or in the evolutionary properties of the host stars.

1.1 Observations of exoplanets orbiting binary stars

Not all stars evolve in isolation like our sun, some stars have companions. When two stars orbit each other under their mutual gravitational force, it is called a binary system. Some of these binaries have been found to harbor planets in two possible planetary configurations, namely S-type where planet orbits one of the binary components and P-type where planet orbits both the stars, also called circumbinary planets (CBPs).

Majority of planets in binaries are in S-type configuration (651 systems) and only 31 systems have been confirmed to be in P-type configuration (Thebault and Bonanni [2025]). Many of these confirmed CBPs orbit main-sequence (MS) binaries, detected in transit by TESS and Kepler mission along with radial velocity method from BEBOP survey. A handful have been proposed to exist around evolved binaries without a confirmed detection till date. These evolved binaries mainly comprise of a white dwarf (WD) as the primary star and a MS star as the companion (or secondary) with orbital separations of the order of solar radius. Such systems (also called Post Common Envelope Binaries, PCEBs) form after the host MS-MS binary goes through a complex and dramatic phase of common envelope evolution, details of which are presented in the section 1.2.3.

1.1.1 Eclipse Timing Variations

Indirect observations of planets around tight PCEBs have been made using Eclipse Timing Variations (ETV) method for several systems (discussions in Zorotovic and Schreiber [2013] , Lohr et al. [2014]). When observed from earth, two components of the binary star eclipse each other as they orbit. Their measurements are called observed (O) eclipse times. These are also calculated assuming keplerian motion of the components (assuming the evolution of binary is decided by mutual gravitational force), called calculated (C) eclipse times. In case, the orbital motion is purely Keplerian, the O-C difference should be zero. When non-zero differences occur, another physical mechanism is at play which is altering the eclipse times. An example of O-C diagram for NN Ser PCEB is shown in Fig. 1.1.

[1] https://exoplanetarchive.ipac.caltech.edu

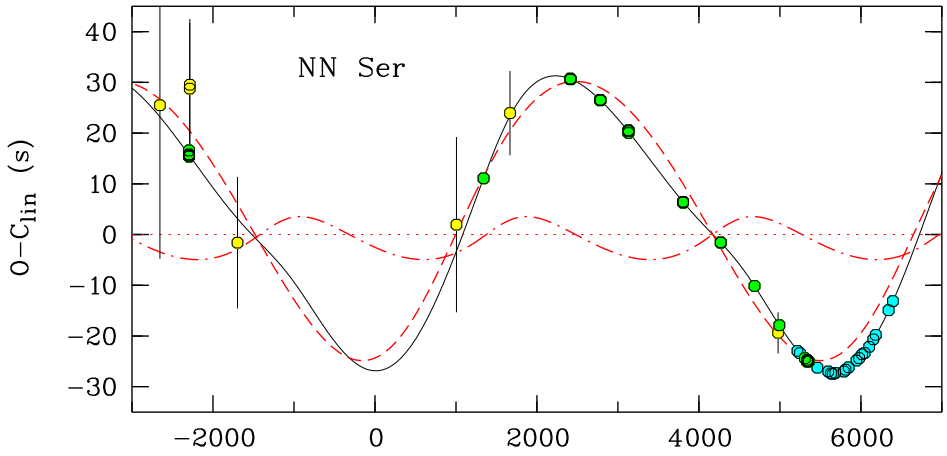


Figure 1.1: Observed - Calculated eclipse times (O-C) diagram for NN Ser. The x-axis is BJD-2450000. Circles represent the observations, black line shows the best fit Keplerian model including two planets and the red curves are the variations due to inner (dash-dot) and outer (dash) planet. Figure from Beuermann et al. [2013].

Physical processes proposed to explain these period variations are magnetic activity of the MS component of the binary or presence of third body in circumbinary orbit, among others. Applegate [1992] presented the first model where magnetic field changes the quadrupole moment or internal density distribution of the star, which in turn modifies the orbital period of the binary. However, this mechanism has been found to require higher energy than what is available to the active star for some systems such as NN Ser (Brinkworth et al. [2006], Völschow et al. [2016]). MHD simulations of dynamo process in active star performed by Navarrete et al. [2022] have shown reduced quadrupole moment variations than those expected from Applegate mechanism. A new mechanism based on magnetic activity of the active binary component was put forward by Lanza [2020] and the MHD simulations (Navarrete et al. [2022]) found the same order of magnitude of variations in orbital period for V471 Tau, using this mechanism. The planetary hypothesis was rejected upon direct imaging of V471 Tau system, with no successful planet detection Hardy et al. [2015]. Recently, Navarrete et al. [2026] presented an N-body framework for evolution of binary star by incorporating quadrupole moment of the active component and computed the O-C diagrams. They find that the variations produced by the Azimuthal Dynamo Waves offer a possible explanation for the ETVs.

NN Ser is one of the most studied PCEB systems showing ETV. The favored mechanism in this system is considered to be the presence of one or two planets. ETV produced through magnetic activity require high energy which is unavailable for the secondary component (Brinkworth et al. [2006], Völschow et al. [2016], Pulley et al. [2022]). NN Ser includes a WD primary and a low mass M dwarf secondary. Multiple planetary models have been developed for this system over the past few years, making it the well studied test case. A dynamically stable two-planet solution was proposed by Beuermann et al. [2010, 2013]. Recent investigations of ETVs on longer timeline till 2023 for NN Ser were conducted by Özdönmez et al. [2023]. They proposed a new model with only one planet of mass $\sim 9.5\ M_J$ in a distant circumbinary orbit with better results obtained on addition of second planet. The two-planet solution was found to be stable for about 10 Myr for only a small parameter range. Single planet model with greater orbital stability put forth by Özdönmez et al. [2023] appear to deviate with the subsequent observations, although by small margin Pulley et al. [2025].

Mechanisms behind ETVs are an active area of research, where one or multiple of those could be generating the observed signals in different systems. Extended ETV baselines are needed to validate the existing models. Observation methods independent of ETVs could help detect the planetary signatures in evolved binaries. Recently, proper motion anomaly method was applied by Baycroft et al. [2023] to the HW Vir PCEB system using the Hipparcos and Gaia catalogues alongside new fits to ETV data. They identified a tentative signal of planetary origin but no conclusive solution for all the four signals was found. High-precision astrometric solutions from Gaia could help support or reject the existence of CBPs in short period evolved binaries in near future ([Baycroft et al., 2023]).

While the planets predicted through ETVs are yet to be confirmed, orbits of circumbinary planets around MS binaries will also go through the stage of reconfiguration as the binary evolves. Moreover planets found in single white dwarf systems or around evolved Pulsars challenge the existing planet formation and evolution theories. Therefore, it is timely to understand the survival and origin of planets around evolved stars.

A few scenarios have been explored over the past few years to explain the presence of planets around evolved stars. First, the planets formed along with the MS binary and survived the non-linear mass loss phase of common envelope evolution (see section 1.2.3). These are referred to as first generation planets. Second scenario is the formation of new planets (second generation) from the material remaining bound to the tight binary, post the violent mass transfer phase (Perets [2010]). Another mechanism of bringing planets in tight orbits around the evolved star through planet migration is Kozai-Lidov effect (Kozai [1962], Lidov [1962]). This is one of the proposed mechanisms for systems such as WD 1856 b (Vanderburg et al. [2020]) where the planetary orbit is suggested to be perturbed by the presence of other companions leading to eccentric orbits and close periastron passages.

The focus of this thesis is to explore the scenarios based on the common envelope channel. Both the study of orbital dynamics of first generation planets during common envelope evolution and formation of second generation planets require 3D hydrodynamic simulations for detailed analysis. It is important to describe the evolutionary stages of binary which affect the orbital properties of already existing planets and may lead to formation of new planets.

1.2 Theoretical Background

1.2.1 Single Star Evolution

To describe the evolution of properties of a single star in isolation, it is assumed to be a non-rotating non-magnetic sphere of gas with self-gravity where only the internal composition is considered. In this case, the forces governing the evolution and structure are due to pressure gradient and gravity. Assuming the stars to be spherically symmetric to first approximation, (preferred configuration in the case of central forces such as gravity) helps reduce the problem to one dimension. Therefore, the structural evolution presented below uses radial coordinate (contents presented below follow Kippenhahn et al. [2013]). Mass distribution inside the star is given by:

$$\frac{\partial\, \mathrm{m(r)}}{\partial\, \mathrm{r}} = 4\pi \mathrm{r}^2 \rho(\mathrm{r}) \tag{1.1}$$

where m(r) and $\rho(\mathrm{r})$ are the mass and density profile of the sphere of radius 'r' at a time 't' and $\mathrm{m}(0) = 0$. Since a star spends long time periods in a phase where no significant acceleration of stellar material is found, a star can be assumed to be in mechanical equilibrium where the forces acting on it balance each other called hydrostatic equilibrium. Here, the force due to pressure gradient acts outwards and the one due to gravity acts inwards. In order to produce no net acceleration, total force should be zero resulting in the following condition,

$$\frac{\partial \mathrm{P(r)}}{\partial \mathrm{r}} = -\frac{\mathrm{Gm(r)}}{\mathrm{r}^2}\,\rho(\mathrm{r}) \tag{1.2}$$

here P(r) is the pressure distribution inside the star. It results in three unknown variables r, P and ρ and only two differential equations. To solve for the variables, another equation of the form $\mathrm{P} = \mathrm{P}(\rho, \mathrm{T})$ is obtained from the thermal state of the star for a particular chemical composition, called as an equation of state (EoS). In case of ideal gas, $\mathrm{P} = \rho\,\mathrm{k_b}\,\mathrm{T}/\mu\,\mathrm{m_u}$ where $\mathrm{k_b} = 1.38065 \times 10^{-16}\,\mathrm{erg\,K^{-1}}$, T is the temperature profile, μ is mean molecular weight and $\mathrm{m_u}$ is the atomic mass unit. For neutral hydrogen gas, $\mu \approx 1$. For general composition where $\mathrm{Z_i}$ is ionization state, $\mathrm{X_i}$ is mass fraction and $\mathrm{A_i}$ is atomic mass number of the species i,

$$\frac{1}{\mu} = \sum_{\mathrm{i}} \frac{\mathrm{X_i}(1 + \mathrm{Z_i})}{\mathrm{A_i}} \tag{1.3}$$

Dynamics of stellar material is now coupled to the temperature distribution of the star, which in turn, is decided by the production of energy (nuclear reactions), loss of energy from the surface and its transport in star. When the rates of energy loss and generation are same then the star is said to be in thermal equilibrium, as found in the case of Main sequence stars. How fast a star ages depends on the rates of thermonuclear reactions. Energy conservation then becomes (Kippenhahn et al. [2013]):

$$\frac{\partial\, l(r)}{\partial \mathrm{r}} = 4\pi r^2 \rho(r)\,(\varepsilon_{\mathrm{nuc}} - \varepsilon_\nu - \mathrm{T}\frac{\partial \mathrm{s}}{\partial \mathrm{t}}) \tag{1.4}$$

where l(r) is the total energy flux, $\varepsilon_{\mathrm{nuc}}$ is the nuclear energy released, ε_ν is the energy removed from the star due to neutrinos and s is the entropy of sphere of radius 'r' for time 't'. Transport of energy from hot to cold regions happens through three processes - conduction, convection and radiation. The energy transport equation is given as follows which sets the temperature gradient under hydrostatic equilibrium:

$$\frac{\partial \mathrm{T(r)}}{\partial \mathrm{r}} = -\frac{\mathrm{G\,m(r)}}{\mathrm{r}^2}\rho(\mathrm{r})\frac{\mathrm{T(r)}}{\mathrm{P(r)}}\nabla \tag{1.5}$$

where $\nabla = \mathrm{d}\log \mathrm{T}/\mathrm{d}\log \mathrm{P}$, depends on the dominant transport process. The rate of change of chemical composition inside a star depends on nuclear reactions and mixing (details can be found in Kippenhahn et al. [2013]), given as:

$$\frac{\partial X_i}{\partial\, t} = \frac{m_i}{\rho}(\sum_j r_{ji} - \sum_k r_{ik}) \tag{1.6}$$

where X_i is mass fraction of nuclei (mass m_i) of specie 'i', first term in brackets denotes the reaction rates which create the element and those which destroy are given by second term. Equations presented above form the complete set that needs to be solved simultaneously to describe the structural evolution of a single star. Below a qualitative description of various stages in the lifetime of an isolated star are presented.

Phases of stellar evolution: A star in main sequence stage can be approximated to evolve in hydrostatic and thermal equilibrium. It typically burns hydrogen (comprises of major elemental fraction) into helium in the central region, and spends the longest time in MS phase until the hydrogen fuel is exhausted. Stages occurring in the lifetime of a star are mainly governed by its initial mass. The luminosity and radius depend on this mass and the chemical composition. In this work, focus is on low mass binary systems with primary component of initial mass of around 2 $\mathrm{M}_{\odot}$ and therefore the following description is for the stars of around that mass.

Once hydrogen is exhausted, the stellar core comprises of helium with hydrogen burning in the adjacent shell (as the only source of nuclear energy). As hydrogen fuses to produce helium, the mass of helium core increases. This results in contraction of the core and increase in its density. Contracting core releases gravitational energy and deposits it in the envelope. The envelope tries to restore thermal equilibrium and expands on thermal timescale so as to cool. This stage is called Red Giant (RG) phase. During this phase radius and luminosity of the star increases. Mass and temperature of the core keeps on rising slowly to the point where it is sufficient to ignite helium. Due to degenerate core (of mass $\sim 0.5\,\mathrm{M}_{\odot}$) and high temperatures, nuclear reactions of helium fusion become violently rapid and increase the core temperature leading to a runaway nuclear process, called Helium flash. At a particular high temperature, helium burning is stabilized in the core and hydrogen is burning in the shell outside it.

As the helium fuel is exhausted, mass fraction of carbon/oxygen increases in the core. Shells immediately above the core comprise of helium burning and hydrogen burning respectively. In case of inert C/O core (of $\sim 0.5\,\mathrm{M}_{\odot}$) not running nuclear reactions, pressure support is reduced and the core begins to contract leading to expansion of the convective envelope. This stage is called asymptotic giant branch where the star is puffed up to even larger radii ($\sim 200\,\mathrm{R}_{\odot}$) with greater luminosity than the red giant phase. Loosely bound envelope may be ejected in the form of stellar winds from the surface expanding outwards from the star. Exposed degenerate carbon/oxygen core contracts till it is supported by electron degeneracy pressure and heats up in the process. Eventually the star ends up being a white dwarf with no nuclear burning and cools down for rest of its lifetime.

1.2.2 Evolution with a close companion

In a detached binary system, two stars (assumed to be point masses or spherically symmetric) orbit their common center of mass under mutual gravitational attraction and follow keplerian laws of motion. The evolution of binary system is governed by the mass of the components and their orbital properties, namely, semi-major axis and eccentricity. Depending upon the evolutionary stage of the components and the orbital separation, a binary can interact via mass transfer. Since the AGB stage can extend up to the radius of around 200-300 $\mathrm{R}_{\odot}$, binaries with similar orbital separations might go through mass transfer phase. In case of close binaries, the assumption of spherical symmetry breaks down due to effects of tidal interactions and asymmetry introduced by rotation of the stars. For detailed explanation on evolution of binary systems, refer to the textbook by Hilditch [2001].

Roche model provides the framework for effective gravitational potential comprising of gravitational potential due to point masses and rotation potential due to synchronous rotation of the binary with zero eccentricity. Using this model, surfaces of constant gravitational potential can be obtained within the rotating frame, depending on the mass ratio of binary

components. The points in 3D space around the binary system where the gradient of effective gravitational potential becomes null are called the Lagrange points. One such point, called L1 point is located on the line joining the center of mass of two stars, at the intersection point of the equipotential surface of the individual stars. The region enclosed by a closed equipotential surface around a binary component, passing through L1 point is called Roche lobe. Size of roche lobes depend on the orbital separation and the mass ratio of the system.

As the more massive star evolves earlier than its companion, it expands and fills it Roche lobe with material flowing over the L1 point which can be accreted by the companion. This initiates the mass transfer phase. The timescale of mass transfer decides further evolution of the binary, in terms of their orbital separation or change in the mass of its components which in turn affects the mass transfer. When mass and angular momentum lost from one component is accreted by the other such that the total mass and orbital angular momentum of the binary remains constant, such an event is called Conservative mass transfer and the opposite scenario is called Non-conservation mass transfer. Ratio of mass of the components changes during mass transfer phase leading to change in the roche lobe radii. In case the donor star is expanding on a faster rate than that of its roche lobe, an unstable mass transfer is set in. This can be found in the cases of high mass-ratios or in case of donors with deep convective envelopes (in RGB or AGB stage). In this case, the mass transfer occurs on dynamical timescale of the donor where the companion is not able to accrete the incoming material and could be engulfed into the envelope of the primary donor leading to the Common Envelope stage.

1.2.3 Common Envelope Evolution (CEE)

Compact objects observed in pair with MS or evolved companion at small separations of a few solar radii, raised the question of how such orbital separations are achieved when the progenitor would have been much larger during its late evolutionary stage of giant branch, typically of the size of a several hundred solar radii. In order to explain the observations of evolved and compact binaries, Paczynski [1976] (and references therein) suggested a transient stage during the binary interaction where the core of the progenitor and the companion orbit each other inside an envelope, called the Common Envelope (CE) phase. One channel of forming common envelope is where the more massive component of the two main sequence stars expands and fills its roche lobe. It begins to transfer mass to the companion on short timescales such that companion cannot accrete all the material and the latter starts to pile up layers. Soon the companion is embedded into the envelope of the donor star and the core-companion pair orbit each other inside the shared envelope of gas (CE).

The mechanism of bringing two stars into tighter orbits through the effect of frictional drag force was proposed by Paczynski [1976]. It was shown through analytical estimates that once the companion is inside the envelope, it experiences torque due to frictional drag force which leads to dissipation of angular momentum from the orbit of the binary to the gas surrounding it. The transfer of angular momentum and orbital energy to the gas surrounding the companion leads to the reduction of orbital separation of the core and companion. As more energy is deposited into the envelope, the envelope is lifted and may be ejected eventually resulting in a close binary system.

Common envelope evolution (CEE) can be divided into physically different stages, each governed by characteristic timescale (Ivanova et al. [2013]). A subset of relevant timescales are presented below (following notation of Ivanova et al. [2020]), followed by description of

the temporal evolution of the common envelope:

- Dynamical timescale ($\tau_{\rm dyn}$) - varies depending on the stage being investigated, for example, when binary components are distinct objects:

$$\tau_{\rm dyn} \approx {\rm P_{orb}} = 2\pi \sqrt{{\rm a^3/GM_{tot}}} \tag{1.7}$$

  whereas when both stars share the envelope, it is equivalent to the free-fall time ($\tau_{\rm ff,\,env}$):

$$\tau_{\rm dyn} \approx \tau_{\rm ff,\,env} \approx \sqrt{{\rm R_{env}^3/GM_{encl}}} \tag{1.8}$$

- Thermal timescale ($\tau_{\rm th}$) - time taken to radiate the entire internal energy of the envelope at the rate of its current luminosity (before CE it is equivalent to the Kelvin-Helmholtz timescale of a star associated with its cooling or contraction, $\tau_{\rm KH} \approx {\rm GM^2/2RL}$ (Kippenhahn et al. [2013])):

$$\tau_{\rm th} = \frac{1}{\rm L_{env}} \int_{\rm env} {\rm u(m)dm} \tag{1.9}$$

where $\rm P_{orb}$ is the orbital period of the binary, a and $\rm M_{tot}$ are the binary separation and the total mass, $\rm R_{env}$ and $\rm M_{encl}$ are the envelope radius and mass enclosed within that radius respectively, u(m) and $\rm L_{env}$ is the specific internal energy and the surface luminosity of the envelope at the corresponding time.

Unstable mass transfer to the companion or Darwin Instability (Eggleton [2011]) can result in the loss of co-rotation of secondary's orbit with the rotation of the giant. This orbital instability leads to onset of a CE by shrinking the orbit of the companion to the point where it is engulfed by the donor's envelope. It progresses over thermal timescale initially to over several dynamical timescales towards the end. This stage is already expected to reduce the donor's mass, angular momentum of the system and the binary separation. Definite distinction of one phase to another is still unclear and studies usually investigate one phase at a time with physically motivated initial conditions. When inspiral timescale (rate of decrease in binary orbital separation) is around a few hundred times the orbital period of the binary, system is expected to enter the next phase, called the plunge-in phase (Ivanova et al. [2020]).

Binary now enters the rapid spiral-in phase which occurs on dynamical timescales where the orbit shrinks fast over several orbital periods of the binary and the orbital energy and angular momentum is transferred locally into the envelope, leading to its expansion. This dynamical inspiral phase results in a partial or full envelope ejection. In case of partial ejection, the system enters a slow (self-regulated) inspiral. Due to substantial expansion of the envelope leading to decrease in the envelope density surrounding the core and companion, along with the gas slowly achieving co-rotation with the orbit, frictional drag force reduces leading to decrease in inspiral rate (Sand et al. [2020], Lau et al. [2022a], Reichardt et al. [2019]). The rate at which the orbital energy is now released in the envelope might be comparable to the rate at which this excess heat in the envelope is transported to the surface of the envelope and radiated away. This phase evolves over thermal timescale of the extended CE where the left-over material is redistributing. Processes occurring on thermal timescale should be included for the study of this phase such as convection and radiation loss, along with the dynamical. Towards the end, entire envelope could be removed resulting in a tight post-CE binary or a merger as the product, with unbound ejecta in the vicinity expanding out.

CEE is a multi-physics and multi-scale problem in both time and space, requiring hydro-

dynamics, gravity, thermodynamics (equation of state and ionization), radiation, convection and high resolution three dimensional simulations for accurate predictions of its outcomes. Three different methods have been utilized so far - parametric models for energy and angular momentum, 1-dimensional drag force based models and 3-dimensional (3D) hydrodynamic simulations as the computational power increased (detailed discussion in review paper by Röpke and De Marco [2023]). First, the parametric models based on energy and angular momentum are detailed and then the 3D numerical simulations are discussed.

Webbink [1984] proposed a formalism based on conservation of total energy. The total energy comprises of the binding energy ($\mathrm{E_{bind}}$) of the donor's envelope at the onset of mass transfer and the orbital energy released due to inspiral ($\Delta \mathrm{E_{orb}}$). Binding energy of the envelope depends on the evolutionary stage of the primary star prior to mass transfer, where λ parameter characterizes the effects of core-envelope boundary and stellar density distribution (de Kool [1990], Dewi and Tauris [2000]). Without studying the dynamical interaction of the binary components, model by Webbink [1984] uses the energy reservoir available for ejection to calculate the orbital separation of the surviving binary ($\mathrm{a_f}$) for given initial parameters - $\mathrm{a_i}$ being the separation at the onset of CE, $\mathrm{M_1}$ and $\mathrm{R_1}$ are the mass and radius of the primary, $\mathrm{M_2}$ is mass of the companion,

$$\mathrm{E_{bind}} = \frac{\mathrm{G M_1 M_{env}}}{\lambda \mathrm{R_1}} \tag{1.10}$$

$$\Delta \mathrm{E_{orb}} = \frac{\mathrm{G M_c M_2}}{2\mathrm{a_f}} - \frac{\mathrm{G M_1 M_2}}{2\mathrm{a_i}} \tag{1.11}$$

where $\mathrm{M_c}$ and $\mathrm{M_{env}}$ are the mass of the core and gaseous envelope of the primary respectively.

$$\mathrm{E_{bind}} = \alpha_{\mathrm{CE}}\, \Delta \mathrm{E_{orb}} \tag{1.12}$$

Not all of orbital energy released is expected to be converted to mechanical energy. A part of orbital energy might go into heating the envelope, could be radiated away and the unbound material could also have non-negligible kinetic energy upon ejection. Therefore, an efficiency parameter (α_{CE}) was defined as the fraction of orbital energy converted to mechanical energy used in unbinding the envelope, with just enough amount to escape (Livio and Soker [1988]). This implies that $\alpha_{\mathrm{CE}} \leq 1$, if only orbital energy is the energy source for unbinding, whereas for extra sources $\alpha_{\mathrm{CE}} > 1$ (Ivanova et al. [2020]). The energy formalism is widely used in binary population synthesis studies for predicting the parameters of post-CE systems.

Internal energy of the envelope was first included in the binding energy calculation (eq. 1.10) by Han et al. [1995], thereby reducing the amount of energy needed to unbind. They considered several components that make up the total internal energy such as, ionization energy released during recombination of charged particles, thermal motion of gas particles and energy in radiation. Another parameter α_{th} was introduced which denotes the fraction of internal energy utilized in envelope ejection and different outcomes were found, with no internal energy contribution ($\alpha_{\mathrm{th}} = 0$) to partial and complete utilization ($\alpha_{\mathrm{th}} = 0.5, 1$).

This energy formalism is a simplified framework for CEE occurring at dynamical timescale, where the contributions from various energy components need to be studied in detail. Originally, it does not account for internal energy budget. Along with this, uncertainties in the

core-envelope structure at the onset of CEE leads to uncertainties in estimating λ and $\alpha_{\rm CE}$ parameters (Ivanova et al. [2013], Röpke and De Marco [2023]). Detailed discussion of all the energy components involved in a CE process is given in chapter 3 of Ivanova et al. [2020].

Alternative parametric formalism based on the angular momentum balance of the system was presented by Nelemans et al. [2000] in order to understand the evolution of double helium white dwarfs. The observed orbital properties of these systems could not be explained by the energy formalism (negative values found for efficiency parameter, $\alpha_{\rm CE}$) for the first mass transfer episode. Upon comparing the pre- and post- mass transfer properties of the binary assuming that the entire envelope is ejected and that the angular momentum is reduced linearly:

$$\mathrm{J_i} - \mathrm{J_f} = \gamma\, \mathrm{J_i}\, \frac{\Delta \mathrm{M}}{\mathrm{M_{bin}}} \tag{1.13}$$

where $\mathrm{J_i}$ and $\mathrm{J_f}$ are the angular momenta of pre- and post- mass transfer binary respectively, $\mathrm{M_{bin}}$ is the total mass of the binary and $\Delta \mathrm{M}$ is the mass lost from the binary. They obtained the range of γ to be $\sim$ [1.4, 1.7] which results in different post-CE parameters. These two simplified parametric models do not reveal the underlying physics of the CEE. A variety of outcomes from CE may be possible depending on the initial mass-ratio, initial separation, evolutionary state of the primary giant (depth of the convective envelope developed prior to in-spiral). Addressing these uncertainties requires detailed numerical investigations of CE phase to study the physical processes involved and whether the binary settles into the observed orbital separations.

With the increase in computational power and development of numerical tools, CEE was studied using both Eulerian grid and SPH schemes in two-dimensional numerical simulations from mid-1980s to mid-1990s (Bodenheimer and Taam [1984], Livio et al. [1990], Yorke et al. [1995]). Detailed reviews of the common envelope evolution field can be found in Iben and Livio [1993], Ivanova et al. [2013], Röpke and De Marco [2023] and Ivanova et al. [2020]. The progress made using state of the art three-dimensional (3D) simulations of CEE are summarized below.

First 3D global hydrodynamic simulations of dynamical inspiral phase using nested grid approach were performed by Sandquist et al. [1998]. They used ideal gas equation of state along with radiation pressure and performed five simulations using combinations of 3 parameters: the companion mass (0.4 or 0.6 $\mathrm{M_\odot}$), the giant star mass (3 or 5 $\mathrm{M_\odot}$) with radius $\sim$ 1 AU and the amount of rotation of the giant envelope (synchronous rotation or no rotation). They found rapid reduction in the orbital separation of binary cores due to drag forces. These simulations revealed spiral density waves due to the orbital motion of the core-companion binary transporting energy and momentum to the outer layers of the envelope. Their results showed pressure-supported differentially rotating thick disk-like structure before the gas is lifted to larger radii. They found the initial degree of rotation of the giant envelope only affected the initial stages of CEE and not the later outcomes. Mass ejection was found to be concentrated to the equatorial plane with 20% to 30% mass unbound from the system with mass loss rates of 0.3 $\mathrm{M_\odot\,yr^{-1}}$ by the end of the simulation.

First high resolution adaptive-mesh-refinement (AMR) simulation was performed by Ricker and Taam [2008] for a red giant primary of mass 1.05 $\mathrm{M_\odot}$ and companion of mass 0.6 $\mathrm{M_\odot}$, using FLASH code. They quantified hydrodynamic and gravitational drag force contributions using simulation and compared them to the analytical drag formalism, showing

that analytical framework overestimates the mass accretion rate and inspiral time. Ricker and Taam [2012] followed up on this work by extending the simulations of a similar system till 56.7 days of inspiral, resulting in unbinding of 25% of CE mass. Their results indicate a reduction in orbital separation by a factor of seven and confirm that the gravitational drag is dominant by 1-2 orders of magnitude than the hydrodynamic drag. By the end of the simulation, the flow around the core and companion is found to be subsonic and CE gas is identified as anisotropically distributed, largely concentrated within the 30° of the equatorial plane with the gas density depicting an approximately $\mathrm{r}^{-5/3}$ profile. Authors note the clear presence of spiral shocks transporting angular momentum outwards in the envelope with the tangential component of the velocity of the envelope being greater than the radial. Almost constant mass loss rate of $\sim 2\,\mathrm{M}_{\odot}\,\mathrm{yr}^{-1}$ is obtained. The simulations performed before and by Passy et al. [2012] could not result in substantial ejection of the envelope and the final separations obtained by the end were found to be greater than those from observations.

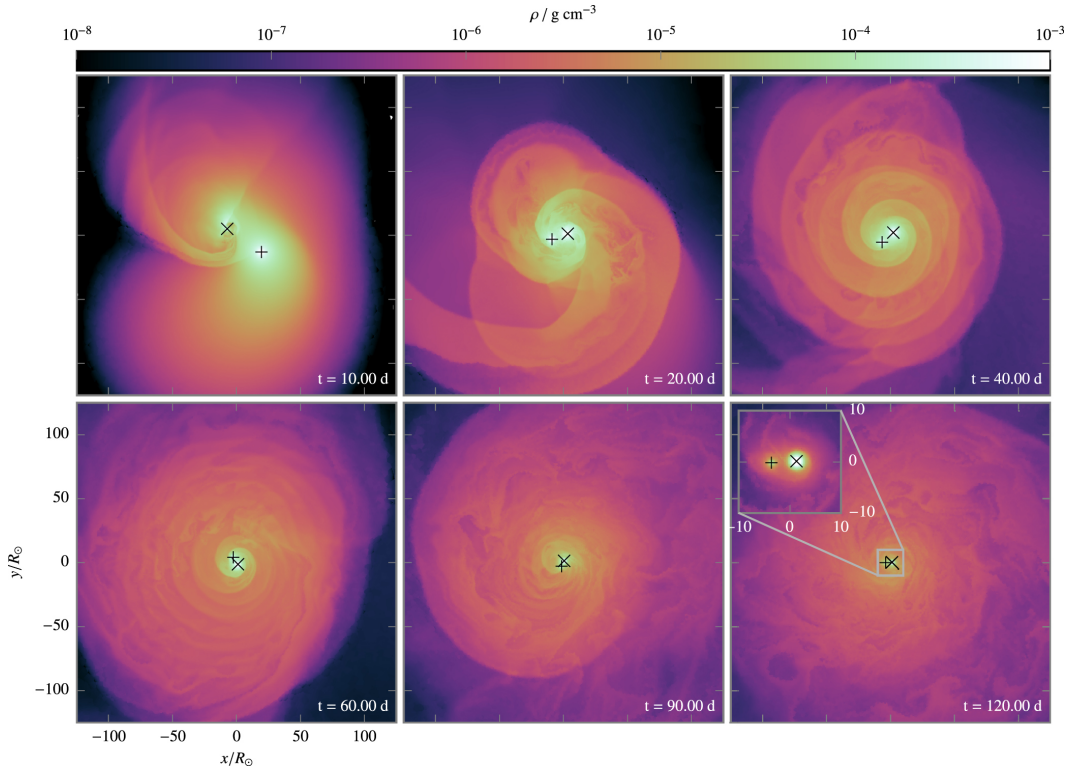


Figure 1.2: 3D Hydrodynamic simulation of dynamical inspiral stage of common envelope phase performed for $2\mathrm{M}_{\odot}$ primary and $0.99\mathrm{M}_{\odot}$ companion using Arepo. Density maps in x-y plane presented at various times. '$\times$' denotes the companion position and '$+$' represents Red giant core. Energy and angular momentum is transported in envelope through spiral shocks and only 8% of envelope mass is removed in the simulation time of 120 days. Figure from Ohlmann et al. [2016].

Ohlmann et al. [2016] performed the first 3D hydrodynamic simulations of dynamical inspiral phase for a low-mass binary in finite volume moving mesh code, AREPO. Red giant donor of mass 2 $\mathrm{M}_{\odot}$ (core mass 0.4 $\mathrm{M}_{\odot}$) undergoing CEE with the companion of mass 1 $\mathrm{M}_{\odot}$ is studied with the core and companion initiated as point particles, interacting only gravitationally. Simulations are run for 120 days of evolution with the ideal gas equation of state. This work was able to achieve the highest resolution of 0.01 $\mathrm{R}_{\odot}$ which allowed them to resolve the onset of turbulent convection over small scales. Only 8% of envelope mass was

found to be ejected and the orbital separation did not shrink to those found in observations. Figure 1.2 shows the time evolution of density distribution during the inspiral phase of the common envelope stage. They find that spiral shocks initially dominate the entire envelope but as the system evolves, Kelvin-Helmholtz instabilities develop in the outer parts of the envelope.

Ideal gas EoS with $\gamma = 5/3$ depicting the common envelope gas as monoatomic has been widely used in the simulations with a few exceptions (Nandez et al. [2015], Nandez and Ivanova [2016], Sand et al. [2020], Reichardt et al. [2020], Lau et al. [2022a,b], Vetter et al. [2024]). This does not account for the partially ionized fraction of the envelope which are present at temperatures of $\sim 10^4 - 10^5$ K, where Hydrogen and Helium are found to be in ionized states of H^+, He^+, He^{2+}. As the common envelope expands and cools this ionized material starts recombining to give hydrogen and helium atoms and releases energy that could help eject parts of the envelope, as first proposed by Han et al. [1995]. Passy et al. [2012] estimated the amount of recombination energy available but did not implement it into the model used for simulations. While they found it to be comparable to the binding energy of the envelope, the unanswered questions such as fraction of recombination energy available for mechanical work and the location and rate of its release into the envelope, remained open.

Subsequent 3D hydrodynamic simulations attempted to address these questions by incorporating more realistic equations of state while simultaneously studying the effects of varying initial parameters such as mass of the binary components, evolutionary stage of the primary (extent of deep convective envelope developed: Red Giant, Asymptotic Giant Branch, Red Supergiant), orbital separation and eccentricity, dust formation, other energy sources such as jets and accretion by the companion, impact of magnetic fields and radiative transfer (see Röpke and De Marco [2023] for review). Reason and conditions behind the halt of inspiral towards the end of simulations have also been an important area of investigation.

On inclusion of recombination energy:
Nandez et al. [2015] and Nandez and Ivanova [2016] performed the first 3D hydrodynamic simulations including recombination energy using the SPH code STARSMASHER for red giants. The numerical experiments were performed with two EoS, ideal gas (including contribution of radiation pressure) and tabulated EoS from MESA including recombination energy. For the ideal gas EoS, their results of partial unbinding of envelope confirm the findings from previous works. They found almost complete envelope ejection for the recombination energy case when it is assumed to be locally thermalized, but no detailed analysis of the underlying ejection mechanism was discussed.

Almost entire envelope ejection in the simulations including recombination energy for OPAL and tabulated EoS, when all internal energy is considered in unbinding was found in the 3D simulations performed by Sand et al. [2020] for AGB phase, Reichardt et al. [2020] for RG phase and Lau et al. [2022a] for RSG stage using different numerical codes: moving mesh, Arepo and SPH code, Phantom respectively for ideal gas, OPAL and tabulated EoS. Sand et al. [2020] and Lau et al. [2022a] found deeper inspiral for companions of different masses in ideal gas EoS case as compared to that for OPAL EoS because the envelope expands slowly in simulation with ideal gas. They found that most of the recombination energy might be released in optically thick regions behind the spiral shock fronts, thereby enhancing the expansion and ejection of material. In all the three studies, Hydrogen recombination fronts are found in the outer optically thin layers of the envelope and helium fronts in the deeper

optically thick layers, such that it cannot be transported/radiated away. Lau et al. [2022b] systematically studied the effects of hydrogen, helium and molecular hydrogen recombination energies assuming the released energy thermalises locally. On inclusion of both the H and He recombination, $\sim 87\%$ of envelope mass is ejected with $\sim 0.1\,\mathrm{M}_{\odot}\,\mathrm{yr}^{-1}$ mass loss rate by the end of the simulation.

Although the above mentioned simulations show that recombination energy helps in ejecting the envelope when the inspiral slows down. The assumption of full thermalization is itself debated. Grichener et al. [2018], Soker et al. [2018] used 1D evolution code MESA to mimic CEE involving a low-mass AGB star and Ivanova [2018] used theoretical constraints, to give estimates on the utilization of hydrogen recombination energy during the dynamical plunge-in phase with contrasting results of negligible usage and efficient usage respectively. On comparing the envelope expansion timescale with the time taken by convection and radiative diffusion to transport recombination energy outwards, Grichener et al. [2018], Soker et al. [2018] found that the hydrogen recombination energy can be easily inhibited from thermalizing locally and be removed from the location of release. They found that 90% of hydrogen recombination energy is not efficiently utilized in envelope ejection and is rather radiated away. They do not study the energy released in Helium recombination which occurs in deeper and optically thick parts of the envelope where the energy cannot be transported away through convection or radiated away, rather it can be efficient in driving the expansion of envelope, may be not the loss of envelope material. Therefore, the complete envelope ejection found in 3D Hydro simulations involving recombination energy could be an upper limit where full calculations should include radiative transport, dust formation (which makes the material optically thick) and resolution sufficient enough to resolve convection.

On the inclusion of radiation transport:
It has only been investigated in a handful of studies for massive primaries evolving into red supergiants. Ricker et al. [2019] were the first to conduct the 3D hydrodynamic simulations of dynamical inspiral phase for massive binary with and without radiative transfer using AMR code, FLASH. They find that the convective flows are present in the adiabatic run only. Radiation was found to carry away part of the heat flux as the thermal timescale is comparable to that of the dynamical.

Effects of radiative transport on a massive CE event were studied by Lau et al. [2025] using SPH code Phantom by implementing implicit flux-limited diffusion. As compared to their adiabatic simulations (where $\sim 80\%$ material is bound by the end of 9 yrs according to the kinetic energy criterion), they found that radiation transport results in $\sim 90\%$ bound mass. They find negligible difference in the amounts of material ejected during the initial years of dynamical inspiral phase for the adiabatic and radiative diffusion scenarios. Mass ejection is strongly obstructed during the slow inspiral stage. Their simulations with radiation transport suggest longer timescales for CEE as compared to the adiabatic simulations. There is almost no difference found between the orbital separations after the dynamical inspiral phase.

On the inclusion of convection:
Due to the presence of deep convective envelopes in RGB and AGB phase, it is important to model this process in 3D simulations in order to get accurate outcomes of CEE but this is currently limited due to high resolution required. Wilson and Nordhaus [2019, 2020, 2022] performed the first set of studies using 1D stellar evolution code, MESA for CE events in both low-mass and high-mass binaries. They compare the timescales for orbital energy deposition

and the convective transport and identify the regions where orbital energy can be utilized in accelerating the envelope and where convection efficiently transports the released orbital energy to the surface from where it is radiated away, assuming static models for primary during inspiral. They noted that convection naturally leads to reduced orbital separation since the companion has to spiral deeper (less massive secondary component spirals deeper than more massive) into the envelope to release large amount of orbital energy. They found the orbital energy released to be sufficient in unbinding, without requiring extra energy sources.

On the role of dust in CEE:
Glanz and Perets [2018] suggested that dust formation right after the dynamical inspiral phase where outer parts of the envelope have expanded beyond the dust condensation radius, could help eject the envelope over long timescales through dust accelerated winds. Iaconi et al. [2020] used the outputs of 3D hydrodynamic simulations and coupled it to a dust formation model, reporting that the dust formation is efficient in the cooler expanded CE parts and forms right after the dynamical inspiral phase, within about a year and a total dust mass of $\sim 10^{-3}\,\mathrm{M}_\odot$ is found in the ejecta by the end of the simulations (neglecting dust destruction). Bermúdez-Bustamante et al. [2024] are the first to self-consistently model dust formation and growth during CE phase including AGB primary of varying masses and tabulated EoS in 3D SPH code, Phantom. They find that dust formation occurs with high efficiency and begins during the inspiral phase itself, starting with a thin shell at around 40 AU (at 5 yr in simulation time). They obtained dust mass of $\sim 10^{-2}\,\mathrm{M}_\odot$ but do not find it to substantially contribute to envelope ejection on dynamical timescale because it forms at large radial separations to the binary where the gas is already unbound. They found amount of mass ejection to be greater due to recombination energy released than that from dust-driven winds.

Other sources and sinks of energy and angular momentum during a CE event are discussed in detail in Röpke and De Marco [2023] and Ivanova et al. [2013, 2020]. Study of common envelope evolution is an active field of research using numerical simulations. Lack of observations of this short-lived phase make it difficult to constrain the simulation models.

1.3 Orbital evolution during host star mass loss

In order to understand the dynamical evolution of orbits of first generation planets during common envelope phase of the host binary, theoretical progress on orbital evolution as the host star loses mass is presented.

The contents for Kepler problem in this section follow Tremaine [2023]. Two-body problem or Kepler problem is to solve for the equation of motion of two point masses orbiting each other under their mutual gravitational attraction. Total energy and angular momentum of the particles are conserved for this system. Orbit of particle of mass m_1 with respect to mass m_2 under the potential of the form $\Phi_\mathrm{K}(\mathrm{r}) = -\mathrm{G\,M/r}$, is called a Kepler orbit. Here M is the sum of mass of the particles and r is their orbital separation. Angular momentum of the particle in Kepler orbit is constant due to central gravitational force. Specific energy of particle m_1 is given by $\mathrm{E} = \mathrm{v}^2/2 - \mathrm{GM/r}$ where v is the speed of the particle. For $E < 0$, orbits are considered bound and in case of $E > 0$, they are referred to as unbound. Angular momentum of the orbit is given by $\mathrm{L}^2 = \mathrm{G\,M\,a\,(1-e^2)}$ where a is the semi-major axis and

e is the eccentricity of the orbit. For bound orbits, semi-major axis is always positive and eccentricity is less than unity. Orbital elements can be obtained from position and velocity vectors of the particle. Semi-major axis is given by $-\mathrm{G\,M/2\,E}$, eccentricity of the orbit is the magnitude of eccentricity vector, $\vec{e} = (\vec{v} \times (\vec{r} \times \vec{v}))/\mathrm{G\,M} - \vec{r}/\mathrm{r}$ and the inclination of the orbit is given by $\cos^{-1}(\mathrm{h_z/h})$ where $\vec{h} = \vec{r} \times \vec{v}$ and $\mathrm{h_z}$ and h are the z-component and magnitude of the specific angular momentum vector, $\vec{h}$.

The two-body problem described above was applied to planetary systems by Hadjidemetriou [1963, 1966a,b]. When mass of the central star is changing with time, M(t), the gravitational potential becomes time dependent. Orbital evolution is now governed by the rate of change of mass and whether the gravitational potential remains spherically symmetric (as asymmetric mass loss would result in recoil force on the central object and torque the orbit of the planet). Hadjidemetriou [1963] performed the first calculations of evolution of orbital elements for the case of isotropic mass loss, which was treated as a tangential perturbative force to the Kepler orbit. This force was found proportional to the rate of mass loss and the velocity vector. Author showed that the angular momentum of the planet (L) is conserved under the assumption of isotropic mass loss independent of the mass loss rate. Energy of the planet is not constant anymore. Since the perturbative force only acts in the orbital plane, inclination of the orbit also remains constant, independent of the rate of change of mass for isotropic loss.

Delaunay variables (a set of coordinate-momentum pairs) are the angle-action variables for the Hamiltonian of the Kepler problem. Since actions are adiabatic invariants (Tremaine [2023]), momenta $\Lambda = \sqrt{GMa}$, L (planet's angular momentum) and $\mathrm{L_z}$ (z-component of angular momentum vector) are almost conserved over one orbital period in the limit of slow mass loss (compared to the orbital period of the planet), acting as negligible additional force. With Λ being nearly conserved, product of mass of central object and semi-major axis is almost constant. From the ratio of Λ/L, eccentricity is found to be nearly constant. Hadjidemetriou [1963] recovered the result of expansion of orbit with loss of mass keeping the eccentricity constant through perturbative force analysis, which was first obtained by Jeans [1924]. In the rapid (mass loss timescale is less than the orbital period of the planet) and isotropic mass loss limit, Hadjidemetriou [1966a] found that both semi-major axis and eccentricity grow depending upon the amount of mass lost, keeping the angular momentum conserved. Following are the semi-analytical relations between initial (subscript 'i') and final (subscript 'f') orbital parameters for planets in initially circular orbit as presented in Völschow et al. [2014], where μ is the mass-loss factor defined as ratio of final to initial central mass:

For adiabatic mass loss -

$$\mathrm{a_f} = \mathrm{a_i}\,\mu^{-1} \quad , \quad \mathrm{e_f} = 0 \tag{1.14}$$

For instantaneous mass loss -

$$\mathrm{a_f} = \mathrm{a_i}\,/(2\,-\,\mu^{-1}) \quad , \quad \mathrm{e_f} = \mu^{-1} - 1 \tag{1.15}$$

Upon discovery of planets in post-MS systems, the attention of community shifted to applying the above findings to planetary systems, in order to explain the orbital configurations. Veras et al. [2011] provided the foundational analytical framework for the orbital evolution of a single planet around a star losing mass isotropically. By introducing a dimensionless

mass-loss index Ψ, a normalized ratio of the orbital period to the mass-loss timescale, they covered distinct regimes from the adiabatic ($\Psi \ll 1$) to runaway ($\Psi \gtrsim 1$). For each regime, they assumed constant mass loss rate and neglected tidal effects and planet-ejecta interactions. They found that the fate of a planet depends critically on the amount and time scale of mass loss phase and planet's initial orbital properties whereas the semi-major axis of planet always increases for monotonic mass loss.

Impact of asymmetric mass loss during asymptotic giant branch stage was first investigated by Parriott and Alcock [1998] but for the cometary orbits, by modeling it as net recoil velocity gained by the central star. This simple parametrization led to unbinding of a significant fraction of comets. Veras et al. [2013] formally derived the general equations for time-evolution of orbital elements, accounting for anisotropy (their eq. 34-38) for single star-planet system. The time-dependent anisotropic mass loss is constrained by the ejecta velocity, host star's co-latitude and longitude. They found that the effects of anisotropic mass loss are significant at larger separations of the order of hundreds of AU and that the orbital inclination of the planet keeps changing with respect to the rotation axis of the star.

The response of planetary orbits to mass loss from single star host has been studied extensively. For review of works on planetary dynamics during post-main sequence evolution, see Veras [2016] and Veras [2021]. In case of single star, maximum mass loss may occur on RGB, AGB or tip of AGB stages. For low mass stars of around $1\ \mathrm{M}_\odot$, mass loss rates have been found to be $10^{-6} - 10^{-8}\,\mathrm{M}_\odot\,\mathrm{yr}^{-1}$ over time periods of $10^4 - 10^7$ yr (Veras et al. [2013]).

Since the discovery of planets orbiting binary systems increased, a handful of studies have studied the planetary reaction to host binary star evolution. Evolution of close binary systems is different from that of single star evolution, where the mass loss scenarios experienced by planets occur over varying timescales (orbital timescales of binary to thermal) and rates. During the dynamical plunge-in phase of CE, dramatic mass loss occurs over a period of few months to years and the binary orbit drives strong asymmetry perpendicular to the equatorial plane. Ricker and Taam [2012] found 90% of ejecting material to be confined within 30° of the equatorial plane. Vetter et al. [2024] similarly found initially spherical symmetry to break into a thick toroidal structure. Currently, the CE simulations show varying mass loss rates and timescales (depending on the binary systems modeled and the physical processes included) by the end of the simulations, such as $\sim 0.3\,\mathrm{M}_\odot/\mathrm{yr}$ for Sandquist et al. [1998], $\sim 2\,\mathrm{M}_\odot/\mathrm{yr}$ from Ricker and Taam [2012] and $\sim 0.015\,\mathrm{M}_\odot/\mathrm{yr}$ for Ohlmann et al. [2016], among others. In addition, these studies do not include radiative transfer calculations which could limit the mass loss.

Veras and Tout [2012] modeled isotropic non-linear mass loss, defining it as a collection of consecutive phases of linear mass loss. They assume that the planet's orbit is always wider than the extent of the evolving CE of the host binary and that planets do not interact with it. They obtain the properties of host binary from rapid binary evolution code, BSE during CE phase and study the planetary response for CE timescales ranging from 10 to 10^4 yrs. They provide relations between initial and final semi-major axes and eccentricities for two extremes of adiabatic and runaway regime with non-linear mass loss, showing that these relations are not dependent on the intermediate stages of evolution and their mass-loss rates. The fate of the planet during entire post-MS evolution only depends on the phase with highest mass-loss rate given the retained mass of the system. They found that a planet within a few tens of AU distance may escape in case of a host binary star of mass $\geq 2\,\mathrm{M}_\odot$ owing to the

rapid mass loss during CEE, for all the timescales investigated in the study.

By using the observations for planets in the PCEB system NN Ser, Mustill et al. [2013] reconstructed the main sequence configuration (using BSE code) and investigated the dynamical stability of the entire planetary system through post-MS evolution under adiabatic and isotropic mass loss scenarios using N-body integrator code MERCURY. They used the product of common envelope efficiency and the binding energy parameter, $\alpha\lambda$, to generate various CE outcomes and concluded that planets orbiting the MS progenitor of NN Ser (first generation planets) are not likely to survive the post-MS evolution. They acknowledged that parameters used for modeling CE evolution could be a significant source of uncertainty along with the assumption of isotropic outflow and no inclusion of fallback material. Therefore, the question of survivability and origin of such planets remained unanswered.

Völschow et al. [2014] conducted a semi-analytical study for NN Ser system, deriving relations between initial and final orbital parameters of first generation planets during common envelope event, for slow and rapid mass loss scenarios in case of both initially circular and eccentric orbits assuming spherically symmetric ejecta. In event of isotropic mass loss for planets on initially circular orbits, they remain bound for adiabatic scenario but move to semi-major axis greater than approximately 10 AU, which is greater than the present day separations of the planets. For rapid mass loss, a planet is unbound for $\mathrm{M_f} \leq 0.5\,\mathrm{M_i}$. Assuming a mass loss factor of ~ 0.3 for NN Ser system with instantaneous ejection, they find that the pre-CE planets are ejected. They also considered the impact of asymmetric mass loss in the form of an expanding disc and found that the first generation planets are ejected. Unlike previous works, they estimated the geometric drag force on the planet and found it to be insignificant compared to the gravitational force of the central mass, suggesting that this force cannot keep the planets bound if the ejecta and planets were to interact. They concluded that these planets might be of second generation origin, in case they exist.

Kostov et al. [2016] investigated the orbital evolution of nine confirmed planetary systems during the CE stage of their host stars. To do this, BSE code is coupled with N-body evolution code REBOUND to obtain orbital properties. BSE models the rapid CE ejection using the energy formalism of CEE (Eq. 1.11) requiring α_{CE} efficiency parameter and pre-CE binary parameters as input. They assume exponential mass-loss from the CE instead of obtaining mass distribution from 3D hydrodynamical simulation. BSE provides stellar parameters as output such as stellar mass, radius, binary separation as a function of time but does not solve for the non-linear gas dynamics of the CE process. Authors assume the mass ejection to be isotropic with no interaction between CBPs and the ejected envelope gas. Some planetary systems used in this study fall into the intermediate mass-loss regime since their orbital periods are comparable to the mass-loss timescales explored. Some CBPs were found to survive for mass ejection rates of $1\,\mathrm{M_\odot\,yr^{-1}}$ and move to wider and eccentric orbits in all non-adiabatic scenarios. They acknowledge that not all CE material becomes unbound which may fall back and could significantly change the dynamics of the planets.

Recent work by Xing et al. [2025] modeled non-conservative stable mass transfer phase during binary star evolution using MESA (mass transfer rates of about $10^{-5}\,\mathrm{M_\odot/yr}$ to $10^{-8}\,\mathrm{M_\odot/yr}$) to study its impact on orbits of circumbinary planets along with the effects of tides due to star's quadrupolar distortion and tidal damping. In their study, planets move to wider orbits and the effect of tides are found to be negligible during the mass loss event in rapid mass transfer phase. This channel of binary evolution is in contrast to the common

envelope phase in terms of the longer timescales involved, of the order of a several million years. This study neglected the interaction of planets with the ejecta, additionally authors note that the ejecta during a CE event could be denser.

Previous works have studied the effects of mass loss during a common envelope event of the host binary on the planetary orbits under certain simplifying assumptions of parameterized isotropic mass loss and no interaction between the ejecta and the planet. But CEE is a non-linear process involving geometrically complex gas distributions with varying mass loss timescales. In this work, 3D global hydrodynamics simulations of mass ejection events are performed by exploring the parameter space of the energy components of the common envelope gas, to quantify its impact on the orbits of first generation planets. One of the goals of this work is to model mass loss scenarios covering intermediate cases along with the well-studied adiabatic and instantaneous events.

1.4 Circumbinary discs post CE

Existence of predicted planets in post common envelope binaries could be explained by a faster planet formation channel which initiates in the circumbinary discs formed after the common envelope event (Perets [2010]). This study focused on wind accreting binaries with separations of a few tens of AU. Only a handful of works exist on second generation circumbinary discs around close evolved binaries both theoretically and observationally.

Schleicher and Dreizler [2014], Schleicher et al. [2015] investigated analytically the potential of forming second generation planets via gravitational instability in post common envelope binaries. For NN Ser system using their fiducial model of surface density power-law index unity and disc mass of 0.146 $\mathrm{M}_{\odot}$, they found formation of planets of masses 6.6 M_{J} at 5.4 AU and 1.9 M_{J} at 3.4 AU for gas temperatures of 370 K and 231 K in the disc respectively, as predicted in observations. Their model showed favorable results for second generation planet formation but the constraints on clump masses reflected strong dependence on disk parameters such as amount of mass bound to the system, surface density and temperature profile of these discs along with the distribution of angular momentum. To quantify initial properties of the potential planet forming disc, detailed numerical study of the post-plunge in phase of CEE including relevant cooling and heating processes is required.

It is important to establish the properties governing gravitational instability in a self gravitating disc, before discussing recent theoretical works. The description and notation follows Lodato [2007]. Let's assume an accretion disc of radius 'R' around a central object of mass M which is infinitesimally thin, such that the disc thickness given by 'H' follows, $H \ll R$. Consider the surface density of disc to be $\Sigma(\mathrm{R},\mathrm{t})$ and that it is rotating with the angular velocity $\Omega = v_{\phi}/R$ where v_{ϕ} is the azimuthal velocity. In radial direction when centrifugal force balances gravity of the central object (assuming negligible pressure forces), the disc is found to be rotating with the Keplerian velocity, $\mathrm{v}_{\mathrm{kep}} = \sqrt{\mathrm{GM/R}}$ in the limit of negligible self gravity of the disc. Upon inclusion of pressure forces in radial direction, the azimuthal velocity is given by:

$$\frac{\mathrm{v}_{\phi}^2}{\mathrm{R}} = \frac{1}{\rho}\frac{\partial \mathrm{P}}{\partial \mathrm{R}} + \frac{\partial \phi}{\partial \mathrm{R}} \tag{1.16}$$

where P is the gas pressure, ρ is the gas density and $\partial\phi/\partial\mathrm{R}$ is the gravitational force due to the central object and the disc. In thin disc approximation, gravity approximately balances

pressure forces in the vertical direction establishing vertical hydrostatic equilibrium. For the strongly self gravitating disc ($\mathrm{M_{disk}} \gg \mathrm{M}$, where $\mathrm{M_{disk}}$ is the mass of the disc), flat rotation is obtained with the surface density profile scaling as $1/\mathrm{R}$.

In case of self-gravitating discs, local axisymmetric perturbations in a disc can become unstable for:

$$\mathrm{Q} = \frac{\mathrm{c_s}\,\kappa}{\pi\,\mathrm{G}\,\Sigma} \lesssim 1 \tag{1.17}$$

$$\kappa^2 = 4\Omega^2 + 2\mathrm{R}\Omega\frac{\mathrm{d}\Omega}{\mathrm{dR}} \tag{1.18}$$

where Q is the Toomre parameter, κ is the epicyclic frequency and $\mathrm{c_s}$ is the sound speed. In case of gravitational instability, self gravitating disc of substantial mass can fragment into dense clumps provided it can cool efficiently, that is, cool on a few rotation periods of the disc. This is a faster planet formation scenario as compared to the core accretion model since it can form massive clumps in a few orbital timescales.

Recently, Pourmand et al. [2025] investigate analytically whether second generation planets can form through gravitational instability in post-AGB CBDs assuming disc properties such as density, size, mass and thermal properties. Upon applying their model to the post-CE CBD proposed in NN Ser, assuming a disc mass of $\sim 0.146\,\mathrm{M_\odot}$, they find the disc to be gravitationally unstable at distances beyond $\sim 3\,\mathrm{AU}$, consistent with the proposed locations of the circumbinary planets in that system and confirming the analytical results obtained by Schleicher and Dreizler [2014]. Bear and Soker [2014] obtained from angular momentum considerations for the binary system, that first generation scenario is more plausible than the formation of second generation planets. Initial stages of giant planet formation via gravitational instabilities in self gravitating isothermal discs were modeled by Lichtenberg and Schleicher [2015], using 3D AMR hydrodynamic simulations in Enzo code. The authors found clump formation occurring over orbital timescales of the disc and defined the required grid resolution important for studying the spiral structures and clump formation through fragmentation.

Observations of circumbinary discs in evolved low-mass binaries:

CBDs around evolved binaries can form through distinct channels depending on the initial orbital separation and the mass transfer history. Relatively wide binaries evolve into post-AGB or post-RGB systems where the evolved star loses mass through stellar winds, with the high angular momentum material settling around the central binary into a stable circumbinary keplerian disc of gas and dust rather than being accreted directly (Van Winckel [2018]). These systems are proposed to have avoided the CE phase entirely, or expelled the CE rapidly with no fast inspiral stage. These post-AGB systems are found to have eccentric orbits of periods between 100 to 2000 days. In contrast, relatively tighter binaries (initial orbital separation less than approximately 2 AU) undergo unstable mass transfer leading to a full CE phase, which results in dramatic shortening of the orbital separation with periods, $\mathrm{P_{orb}} \leq 1\,\mathrm{day}$. Remaining bound material post the CE phase may form a post-CE CBD (Kashi and Soker [2011]).

A large number of CBDs have been observed around optically bright post-AGB or post-RGB binaries in the Milky way (Kluska et al. [2022]) with sizes of $\sim 100 - 500\,\mathrm{AU}$, optically thick mid-planes, inner dust rim temperatures of 1200 - 1300 K, and dust masses of $\sim 10^{-3}\,\mathrm{M_\odot}$

(Bujarrabal et al. [2017], Andrych et al. [2023], Corporaal et al. [2023b], Kluska et al. [2022], Van Winckel [2018]). These properties are strikingly similar to those of protoplanetary discs in hydrostatic equilibrium around Young Stellar Objects (Kluska et al. [2018], Corporaal et al. [2023a]). These discs are found to be dense and massive enough to provide a possible environment for second generation planet formation, though with a shorter lifetime of $10^4 - 10^5$ yr (Bujarrabal et al. [2017]). Pourmand et al. [2025] recently ruled out the possibility of planet formation via gravitational instability in these discs.

While circumbinary discs around post-AGB binaries have been observed in significant numbers and characterized in detail, direct observational evidence for post-CE CBDs remains scarce. The only detection to date is an excess emission detected with ALMA around the young PCEB NN Ser (WD-MS binary) with the age of WD $\sim 1.3\,\mathrm{Myr}$. It was interpreted as a circumbinary dust disc of mass $\sim 0.8\,\mathrm{M}_\oplus$ located within 1000 AU of the central binary and consistent with bound CE ejecta [Hardy et al., 2016]. The formation, lifetime and evolution of dynamical properties of CBDs such as total mass, spatial extent, and thermodynamic structure of post-CE CBDs therefore remain unconstrained by observations, and numerical simulations of the CE phase are the next step towards characterizing these properties. Current state of this numerical work is summarized below.

One of the main open questions to be resolved is the amount of CE material gravitationally bound to the binary cores after dynamical plunge in phase. Analytical study performed by Kashi and Soker [2011] in the case of rapid gravitational energy released deep into the envelope, showed that $\sim 10\%$ of the envelope mass possessing angular momentum may be bound to the system, which can eventually fall back and form a circumbinary disc due to angular momentum conservation. While hydrodynamic simulations of the inspiral phase with adiabatic equation of state show only a fraction of CE being unbound (Sandquist et al. [1998], Ricker and Taam [2012], Ohlmann et al. [2016], Chamandy et al. [2020]), recent simulations including the release of recombination energy show almost full ejection of envelope (Sand et al. [2020], Lau et al. [2022a], Vetter et al. [2024], Nandez et al. [2015]). In these runs, recombination energy is assumed to be thermalized fully and none of the simulations above include radiation transport or cooling processes which are expected to limit the amount of mass ejected (Lau et al. [2025]).

In addition to retained mass, post inspiral gas distributions needed to be investigated for sustained rotational properties with time and temperature profiles. For fragmentation due to gravitational instability the circumbinary gas should be cooled down to temperatures of a few hundred to a few thousand Kelvin. Kuruwita et al. [2016] induced fall back disk formation to study its effects on the orbital evolution of core and companion using hydrodynamical simulations in ENZO code but they do not follow the CE ejection and fall back phase. They perform simulations for ideal gas equation of state with $\gamma = 5/3$ for two initial temperature values of 350 K and 35000 K (uniform temperature profile). Upon evolution, all simulations result in similar volume-averaged virial value of temperature $\sim$ 50000 K independent of the different initial temperature values.

Numerical works on CE have also shown the presence of geometrically thick toroidal structure around the remnant binary which is pressure supported, slowly expanding and differentially rotating (Sandquist et al. [1998], Vetter et al. [2024], Reichardt et al. [2019]).

Using SPH code Phantom, Reichardt et al. [2019] studied post dynamical plunge in phase.

They identify fall back particles as those which lie outside a spherical volume around the binary and have negative radial velocity relative to the center of mass of system. However, they do not mention the radius of this spherical volume used in their calculation. For their high-resolution simulation of an RGB primary of mass $0.88\,\mathrm{M}_\odot$ ($0.392\,\mathrm{M}_\odot$ core and $0.488\,\mathrm{M}_\odot$ gas envelope) and radius $93\,\mathrm{R}_\odot$ with $0.6\,\mathrm{M}_\odot$ point mass companion orbiting each other with an initial orbital separation of around $218\,\mathrm{R}_\odot$, they find that only 11% of the gas mass unbinds. According to their fall back mass criteria, the total mass with negative radial velocity outside a certain spherical volume is found to be $\sim 0.15\,\mathrm{M}_\odot$ at approximately 19 yr of evolution time with specific angular momentum in z-direction to be $\sim 0.9 \times 10^{52}\,\mathrm{erg\,s}$ (inferred from their Fig. 12). This material exists within the region of 3.5 AU radius. They find that none of the hanging material falls back close to the binary but rather collides with the outflowing gas. By the end of their simulation, material is distributed in a toroidal structure.

Vetter et al. [2024] follow the CEE of a massive binary ($\mathrm{M_{primary}} = 9.4\,\mathrm{M}_\odot$, with two companions of mass $\mathrm{M}_2 = 5\,\mathrm{M}_\odot, 1.4\,\mathrm{M}_\odot$) beyond the dynamical inspiral phase, simulating to ∼37 yr for the companion mass $\mathrm{M}_2 = 5\,\mathrm{M}_\odot$, using 3D MHD simulations in AREPO with recombination energy included via the OPAL equation of state. They find that the thick toroidal structure forms by the end of dynamical inspiral itself with gravitationally bound gas in circularized motion. This circumbinary structure was found to satisfy the Rayleigh stability criterion with sub-keplerian rotation profile ($\Omega \propto \mathrm{r}^{-1.86}$) indicating substantial pressure support. While they find almost complete removal of the envelope, authors acknowledge that some internal energy will be lost through radiative cooling, therefore reducing the amount of internal energy available for mechanical work.

Given the status of 3D (magneto-) hydrodynamic simulations of post dynamical plunge in phase, adiabatic equation of state results in geometrically thick pressure supported structures. Simulations with adiabatic equation of state result in substantial amount of bound mass fraction. One of the aims of this work is to investigate if bound gas distributions after the ejection phase end up in disc-like structures, under different thermodynamic conditions. Furthermore, the goal is to determine whether these distributions become gravitationally unstable to fragment, hinting at the possibility of second generation planet formation in these discs. This is addressed in chapter 4.

Chapter 2

Methods

In order to numerically model the impact of common envelope evolution of the central binary on the orbital evolution of planets (at separations of a few AU in this work) self-consistently, large range of length scales need to be resolved over long timescales such that at least two orbits of the planets in the system are completed, to infer about their future evolution. Since this would require large computing resources and time, the central binary is treated as a single point particle. During the rapid inspiral phase when the binary separation has reduced down to a few solar radii and the inspiral rate has slowed down. This length scale is at least two orders of magnitude smaller than the size of the envelope or the initial planetary semi-major axes chosen for this work along with the size of the computational domain. This method helps to model the planetary orbital evolution along with following the bound and unbound common envelope ejecta out to the domain boundary. The numerical setup used for this work is described below.

2.1 Simulation Setup

To study the interaction between planets and CE gas, 3D AMR gravo-hydrodynamic simulations of the mass ejection stage of the binary star are performed using FLASH code. Consider the binary has developed a common envelope and the core and companion have reached a close separation with slow inspiral rate during the dynamical inspiral phase such that both can be treated as a single point particle. The model includes a self-gravitating gas sphere (representing the common envelope) with the binary and the two planets modeled as point particles, interacting only gravitationally with the gas and among themselves. To study the temporal evolution of the envelope structure, the following equations are solved for ideal and compressible HD:

$$\frac{\partial \rho}{\partial \mathrm{t}} + \nabla \cdot (\rho \mathbf{v}) = 0 \tag{2.1}$$

$$\frac{\partial (\rho \mathbf{v})}{\partial \mathrm{t}} + \nabla \cdot (\rho \mathbf{v}\mathbf{v}) + \nabla \mathrm{P} = -\rho \nabla \phi \tag{2.2}$$

$$\nabla^2 \phi = 4\pi \mathrm{G}\rho \tag{2.3}$$

$$\frac{\partial \rho \mathrm{E}}{\partial \mathrm{t}} + \nabla \cdot [(\rho \mathrm{E} + \mathrm{P})\mathbf{v}] = -\rho \mathbf{v} \cdot \nabla \phi \tag{2.4}$$

Here ρ, $\mathbf{v}$ and P are the density, velocity, and pressure of the gas. E denotes the sum of specific internal and specific kinetic energy given as $\mathrm{E} = \epsilon + |\mathbf{v}|^2/2$. The gravitational potential of the gas is represented by ϕ. The equation of state for an ideal gas is used to close the system of equations $\epsilon = \mathrm{P}/\rho\,(\gamma - 1)$ with the ratio of specific heats, $\gamma = 5/3$.

2.2 Initial Conditions

Common envelope has constant density in the central region which decreases in the outer expanding parts with a power law index two. The gaseous sphere is initialized with the following density profile:

$$\rho(\mathrm{r}) = \begin{cases} \rho_\mathrm{o}\,, & 0 \le \mathrm{r} \le \mathrm{r_o} \\ \rho_\mathrm{o}\mathrm{r_o^2}/\mathrm{r}^2\,, & \mathrm{r_o} < \mathrm{r} \le \mathrm{r_{env}} \end{cases}$$

where $\mathrm{r_o}$ and $\mathrm{r_{env}}$ are the radius of core region around the binary point particle and the radius of gas envelope. ρ_o is the density of the core which is decided by the mass of envelope $\mathrm{M_{env}} = 1.5\ \mathrm{M_\odot}$, $\mathrm{r_o} = 0.2\ \mathrm{AU} \sim 43\ \mathrm{R_\odot}$ and $\mathrm{r_{env}} = 1\ \mathrm{AU} \sim 215\ \mathrm{R_\odot}$. These parameters remain fixed for the set of simulations performed in this work. The pressure is a function of density only, $\mathrm{P(r)/P_o} = (\,\rho(\mathrm{r})/\rho_\mathrm{o}\,)^\gamma$. Here $\mathrm{P_o}$ is the pressure of the core region.

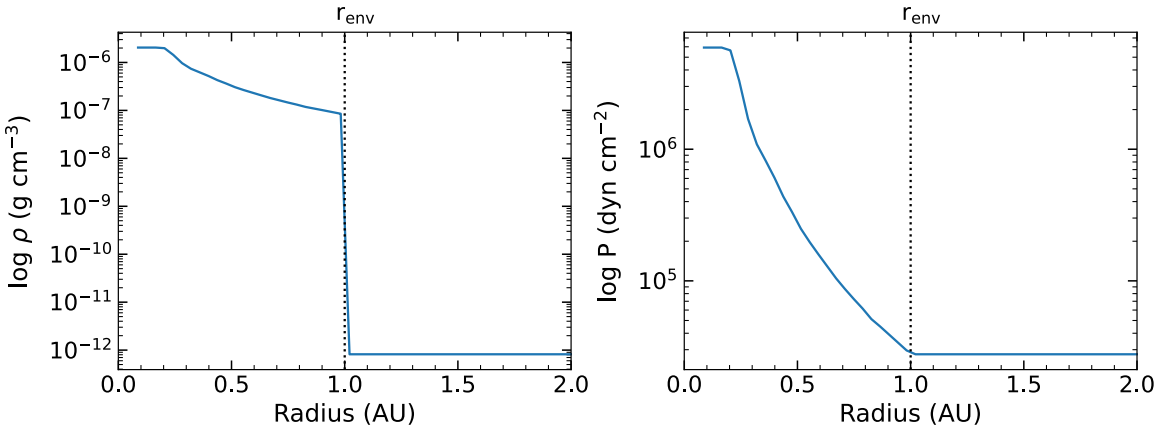


Figure 2.1: Radial profiles of density and pressure for the spherical gas envelope at the onset, for all the simulations. Vertical dotted line indicates the edge of the gas envelope at $\mathrm{r_{env}} = 1\ \mathrm{AU}$.

CE is found to have a rotation profile due to pre-CE phase and the transfer of angular momentum from the orbital shrinkage. The gas envelope is initialized with the solid body rotation profile $\mathrm{v_{rot}} = \sqrt{\mathrm{x}^2 + \mathrm{y}^2}\ \Omega$ and a radial velocity profile presented below to generate an expanding common envelope:

$$\mathrm{v_{rad}(r)} = \begin{cases} \mathrm{r_o}\ \mathrm{v_{edge}}/\mathrm{r_{env}}, & 0 \le \mathrm{r} \le \mathrm{r_o} \\ \mathrm{r}\ \mathrm{v_{edge}}/\mathrm{r_{env}}, & \mathrm{r_o} < \mathrm{r} \le \mathrm{r_{env}} \end{cases}$$

where $\mathrm{v_{edge}}$ is the radial velocity of gas at the envelope edge, $\mathrm{r_{env}}$. $\mathrm{P_o}$, $\mathrm{v_{edge}}$ and Ω vary for the set of simulations performed in this work. These are decided by the dimensionless energy parameters of the envelope, defined in Table 2.2. Radial profiles of pressure and density, and several velocity components of the gas envelope at the onset of the simulation are shown in Figs. 2.1 and 2.2 respectively. The planets are initialized on circular Keplerian orbits with respect to the system's center of mass and the initial properties of these point particles are listed in Table 2.1. The planets' starting positions are taken from Beuermann et al. [2013] as they are the best fit stable orbital configuration obtained for ~ 1 Myr.

The density of the ambient medium, ρ_amb, is such that it does not contribute significantly to the mass of common envelope gas. It is set to a constant density of 5 orders of magnitude less than the density at the gas envelope edge. The pressure of the envelope edge and the

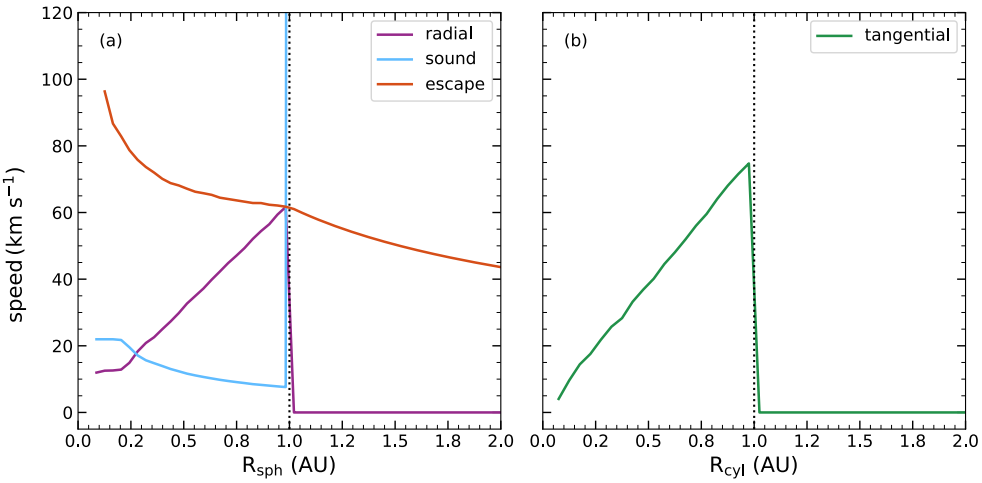


Figure 2.2: Radial velocity, escape velocity and sound speed profiles as a function of spherical radius and tangential velocity profile with respect to cylindrical radius since gas envelope is initialized with solid body rotation, at the start of the simulation I1. Black dotted line shows the edge of the gas envelope, $r_{env} = 1$ AU. Sound speed in ambient medium is 2374.84 km/s.

particle	mass	**r** (AU)	**v** (km/s)
Binary star	0.646 $M_\odot$	(0, 0, 0)	(0, 0, 0)
Planet 1	1.73 M_{jup}	(-3.374, 0, 0)	(0, -23.76, 0)
Planet 2	6.97 M_{jup}	(5.373, 0, 0)	(0, 18.86, 0)

Table 2.1: Initial parameters for point particles are fixed for all simulations performed. Used stable planetary configurations as proposed by Beuermann et al. [2013].

ambient medium is kept equal. The uniform ambient medium is initialized at rest with a constant temperature (which is almost five orders of magnitude higher than the temperature at envelope edge due to a jump in the density). In Fig. 2.3, the snapshot of gas density distribution in the orbital plane of the planets is presented along with the three point particles at the start of a typical simulation. Mass of gas on the computational volume at the beginning of the simulations is 1.586 $M_\odot$.

To perform 3D hydrodynamic simulations, FLASH code (Fryxell et al. [2000], Dubey et al. [2008]) is utilized which uses a finite-volume method to solve Euler equations of hydrodynamics (Eqs. 2.1, 2.2 and 2.4). The split piecewise-parabolic method (PPM) solver is utilized for the simulations performed for chapter 3. The multi-grid method is used to solve Poisson equation (Eq. 2.3) with isolated boundary conditions and the Gamma module is used to solve for the adiabatic equation of state. Cartesian geometry is used for the grid and the boundary conditions for the simulation domain are set to diode. The standard second derivative refinement criterion is applied on gas density to select blocks for refinement and the AMR code keeps region around point particles at highest resolution. Leapfrog time-step integrator is used for point particles with sink accretion and merging being switched-off. The simulation box is of 40 AU length on each side, with the smallest cell size of 0.078 AU for all the simulations of chapter 3.

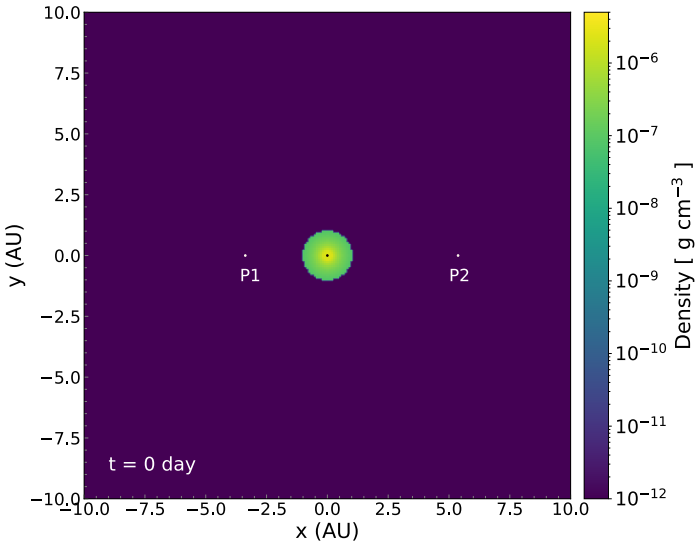


Figure 2.3: Initial gas density distribution in the x–y plane, showing a 20 AU zoomed-in region of the computational domain (actual box size 40 AU). The central black point particle denotes the binary star and the two white point particles, P1 and P2 represent circumbinary planetary companions.

parameter	energy components
$\eta = \dfrac{\mathrm{KE}}{\mathrm{PE}}$	$\mathrm{KE} = \mathrm{KE_{rad}} + \mathrm{KE_{rot}} \quad ; \quad \mathrm{PE} = -\displaystyle\int_0^{\mathrm{r_{env}}} \frac{\mathrm{G(M(r) + M_{BS})}}{\mathrm{r}}\,\rho(\mathrm{r})\,\mathrm{dV}$
$\beta = \dfrac{\mathrm{TE}}{\mathrm{PE}}$	$\mathrm{TE} = \displaystyle\int_0^{\mathrm{r_{env}}} \frac{\mathrm{P(r)}}{(\gamma - 1)}\,\mathrm{dV}$
$\zeta = \dfrac{\mathrm{KE_{rad}}}{\mathrm{KE_{rot}}}$	$\mathrm{KE_{rad}} = \displaystyle\int_0^{\mathrm{r_{env}}} \frac{\mathrm{v_{rad}^2}}{2}\,\rho(\mathrm{r})\,\mathrm{dV}\,; \quad \mathrm{KE_{rot}} = \int_0^{\mathrm{r_{env}}} \frac{\mathrm{r_\perp}^2\,\Omega^2}{2}\,\rho(\mathrm{r})\,\mathrm{dV}$

Table 2.2: Dimensionless parameters and their respective components. Here M(r) is the mass of gas enclosed within radius r and $\mathrm{M_{BS}}$ is the mass of the binary star point particle.

Upon evolution of the system, finger-like structures develop at the expanding interface due to initial conditions of the setup (details can be found in section 3.3). Since a spherical gas envelope has been implemented on the cartesian grid, the interface is not a smooth sphere due to cell boundaries. In order to reduce any grid dependency of these fingers, 10% of uniform white noise is added to the velocity field.

2.3 Simulation setup for Circumbinary disc

For the simulations presented in Chapter 4, modifications are made to the numerical setup mentioned above. The computational domain is extended from 40 AU to 100 AU, requiring a different refinement criterion to better resolve the central region. A nested-grid setup is adopted instead of adaptive mesh refinement (AMR). The refinement criterion is based on spherical radius where the blocks within 5 AU radius are refined to maximum refinement level throughout the entire run, with each block containing 8^3 cells. This results in the smallest grid cell size of 0.049 AU at the highest resolution, in the spherical region of radius 5 AU centered at (0, 0, 0). Further, blocks are de-refined to the lowest level of refinement in the

domain lying outside this distance. The central binary point particle is resolved at the highest resolution level. The grid distribution of a typical simulation at a later time in evolution, is presented in Fig. 2.4. The simulations in chapter 4 are conducted using two equations of state (EoS): adiabatic and isothermal. The Euler equations are solved using the Bouchut solver for both the cases. Isothermal EoS simulations employ the Polytrope module of the FLASH code and for the adiabatic, Gamma module is utilized.

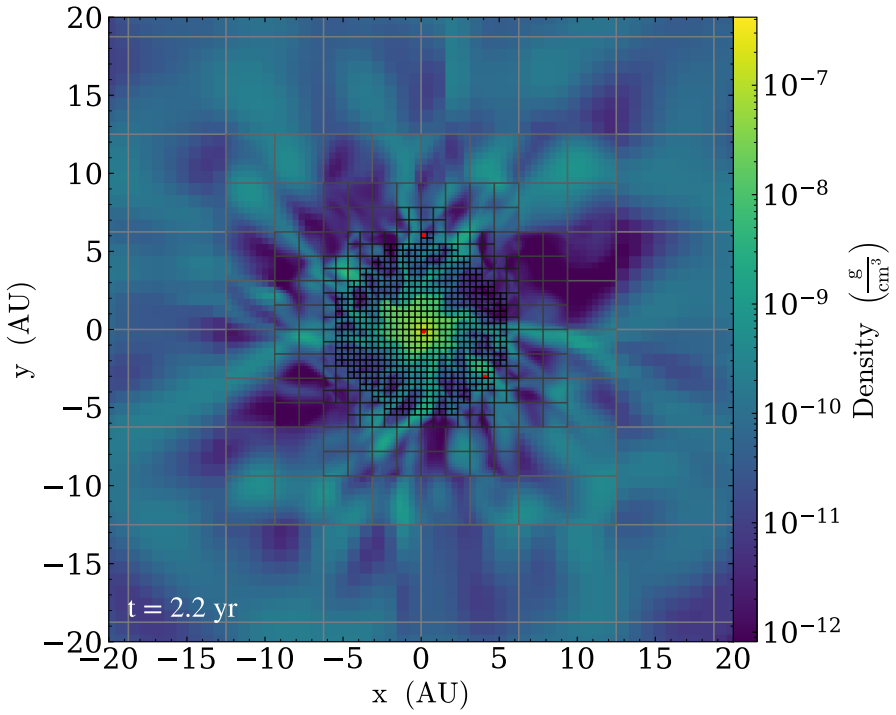


Figure 2.4: Grid distribution overlaid on gas density slice in x-y plane at t=2.2 yr for $\eta 0.64_\mathrm{adia}$ simulation. Zoomed-in on 40 AU region of the full domain.

The mass of gas sphere representing the common envelope is fixed at $1.5\,\mathrm{M}_\odot$ and the radius at 1 AU. Similar to previous setup, gaseous sphere is initialized with a solid body rotation profile and a radial velocity that increases linearly with radius outside the central high-density core region, a typical example shown in Fig. 2.2. The system is embedded in an ambient medium of density $8.18 \times 10^{-13}\mathrm{g\,cm^{-3}}$. Temperature of envelope edge is 4307.3 K and of the ambient medium is 4.069×10^{8}K for adiabatic simulations. Isothermal simulations are run with constant temperature of 4308.18 K in the computational volume. Sink accretion and merger are turned off in these simulations. The two point particles representing planets are also initialized in these simulations to follow their evolution.

As the domain length in each direction is increased from 40 AU to 100 AU, density for ambient medium could not be reduced further as the corresponding temperature would increase accordingly, thereby reducing the timestep for the simulations. Due to larger volume, ambient medium adds to the mass on the grid substantially. The radial profiles of gas density and radial velocity for the entire domain are presented in appendix B.1. Ambient medium is static initially and only moves outwards as the system evolves. It does not appear to dynamically affect the central 20 AU region.

Computing Resources:
I gratefully acknowledge the computing time made available on the high-performance computer "Lise" at the NHR center NHR@ZIB. This center is jointly supported by the Federal Ministry of Research, Technology, and Space and the state governments participating in the NHR. All the numerical simulations were performed using the *FLASH* code. The simulation software was developed by the DOE NNSA- and DOE Office of Science-supported Flash Center for Computational Science at the University of Chicago and the University of Rochester. The simulations presented in first generation planetary dynamics project were performed using approximately 1.5 Million CPU hours. One simulation utilized approximately 187,000 CPU hours on 384 cores. Those presented in circumbinary disc project used approximately 500,000 CPU hours in total. Publicly available python packages: *YT*, *Numpy*, *Matplotlib* and *Scipy* were utilized for all data analysis and visualization.

Chapter 3

Impact of CEE on first generation CBP orbits

3.1 Aim

Dynamical effect of mass loss on orbits of circumbinary planets and their eventual fate has been studied using both analytical/semi-analytical estimates (Völschow et al. [2014], Veras and Tout [2012]) and N-body simulations (Kostov et al. [2016], Xing et al. [2025]). The study by Veras and Tout [2012] was performed using the simplifying assumptions of negligible gas planet interaction and isotropic mass loss for the limiting mass loss scenarios: adiabatic (mass loss over longer timescales compared to orbital period of the planet) and instantaneous mass loss (mass loss over shorter timescales compared to orbital period). Völschow et al. [2014] investigated the effects of both spherically symmetric and disk-shaped ejection, along with estimating the geometric gas drag effects but only for the two limiting regimes of mass ejection. Kostov et al. [2016] treated the binary cores as point particles losing mass isotropically with a prescribed mass loss function and timescales, neglecting the gas-planet interaction, for the two limiting regimes as well as the intermediate regime (mass loss timescales comparable to orbital period). Xing et al. [2025] studied the impact of stable mass transfer between the binary components rather than a CE and the effect of tides, using mass evolution from a 1D code.

Current 1D stellar evolution codes cannot accurately model the transient and highly non-linear common envelope phase of the binary star host as the rate and amount of mass ejection varies non-linearly during a single common envelope event. In this work, mass loss over varying timescales during common envelope event are modeled using global 3D hydrodynamic simulations to study the impact on dynamics of circumbinary planets. This enables study of orbital properties and fate of the first generation planets consistently with the asymmetric evolution of the gas envelope, where mass loss is modeled by varying the energy budget components of the CE gas.

3.2 Parameter study

Common Envelope ejection events in this study are characterized by three dimensionless parameters mentioned in Table 2.2, where KE is the total kinetic energy consisting of radial ($\mathrm{KE_{rad}}$) and rotational ($\mathrm{KE_{rot}}$) components, PE is the total gravitational potential energy of gas including contributions from self gravity of the gas and from the point particle representing binary star and TE is the thermal energy. These are cumulative (or enclosed) energy components, calculated over the initial extent of the sphere (1 AU). The initial point particle properties and initial total PE of gas, which is 7.076×10^{46} erg, is fixed for all the simulations by not varying $\mathrm{M_{env}}$, $\mathrm{r_o}$ and $\mathrm{r_{env}}$, which keeps the density profile in the gas envelope fixed. The parameter values for different simulations are set by these energy components such that they produce varying rates and amounts of mass loss.

The simulations are divided into sets that model scenarios such as Adiabatic, Instantaneous, or Intermediate, as defined in 1.3. To achieve this, the dimensionless parameters η and

Run	η	η/β	$\eta+\beta$	T_{edge} (K)	v_{edge} (km/s)	Ω (rad/s)	$\mu_{dyn,min}$ P1, P2
I1	0.64	9.6	0.7067	4224.52	62.82	5.15×10^{-7}	0.76 , 0.83
A1	0.1	0.165		42400.68	24.83	2.04×10^{-7}	1. , 1.
M1	0.35	1		24690.7	46.68	3.83×10^{-7}	0.98 , 0.99
I2	1.6	24	1.6667	4224.52	99.34	8.15×10^{-7}	0.57 , 0.59
M2	0.83	1		58240	71.7	5.88×10^{-7}	0.74 , 0.82
I3	3.2	48	3.2667	4224.52	140.48	1.15×10^{-6}	0.47 , 0.47
M3	1.63	1		114,149.84	100.36	8.23×10^{-7}	0.53 , 0.66
I4	5	75	5.0667	4224.52	175.6	1.44×10^{-6}	0.42 , 0.42

Table 3.1: Summary of the initial properties of the simulated common envelope events. Last column presents the dynamic mass-ratio values for the maximum loss incurred during the entire simulation, $\mu_{dyn,min}$ (Eq 3.1) for the two planets respectively. Mass of gas envelope interior to each planet's orbit is 1.5 $M_\odot$ at the beginning of all the simulations.

β are varied by setting v_{edge}, Ω and P_{core} for the gas envelope and keeping the ζ parameter set to 1, which means equal split between KE_{rad} and KE_{rot}. The initial properties of the simulations performed are listed in the Table 3.1. For each value of $\eta+\beta$, two or three mass-loss scenarios are constructed which differ in their kinetic and thermal energy partitioning as defined below:

- Kinetic Energy dominated mass ejection events (KE > TE), [I] runs - keeping potential and thermal energy ($\beta = 1/15$) constant at 7.076×10^{46} erg and 4.717×10^{45} erg respectively, at onset of the simulation at t = 0. This results in the initial $T_{edge} = 4224.52$ K.
- Thermal Energy dominated mass loss model (KE < TE), [A] cases - with $\eta = 0.1$ at t = 0.
- Equal Kinetic and Thermal energy partitioning (KE = TE), [M] runs - for $\zeta = 1$ and PE kept constant at the onset.

Given that a common envelope event has not been directly observed to date, the parameter space for the simulations has been constrained using the properties from previous CEE works and observations of planetary nebulae, PNe (observed a few thousand years after a CE event). The range for η is chosen such that the v_{rad} and v_{rot} reflect the parameter space spanned by radial and tangential velocities. While in simulations radial and rotational velocities range from $\sim 30 - 230\,km\,s^{-1}$ for different systems in equatorial plane of the binary and perpendicular to it (Ohlmann et al. [2016], Ricker and Taam [2012], Vetter et al. [2024], Ondratschek et al. [2022], García-Segura et al. [2021]).

Kinematic properties of PNe (with close binary as the nuclei) from observations show varying expansion velocities such as, $2V_{exp} = 60 - 70\,km\,s^{-1}$ (NGC 6778), $2V_{exp} = 30 \pm 3\,km\,s^{-1}$ (NGC 6326), $2V_{exp} = 110\,km\,s^{-1}$ (ETHOS 1), $2V_{exp} = 80\,km\,s^{-1}$ (A 41) and $2V_{exp} = 56\,km\,s^{-1}$ (Necklace) among others (Miszalski et al. [2011] and references therein). It is important to note that substantial number of these PNe are found to be asymmetric with features expanding at varying velocities. One such feature is collimated bipolar outflows

which are found to be moving outwards at high speeds of $\gtrsim 200\,\mathrm{km\,s^{-1}}$ (NGC 6337) (García-Díaz et al. [2009]). The temperature of the envelope front T_{edge} at 1 AU varies from ~ 4200 K to 10^5 K in M3 case, at the onset of the simulations. Simulation with equal parts KE and TE for set 4 is not explored as it would result in even higher gas temperatures which are not found in CE simulations involving low-mass binaries.

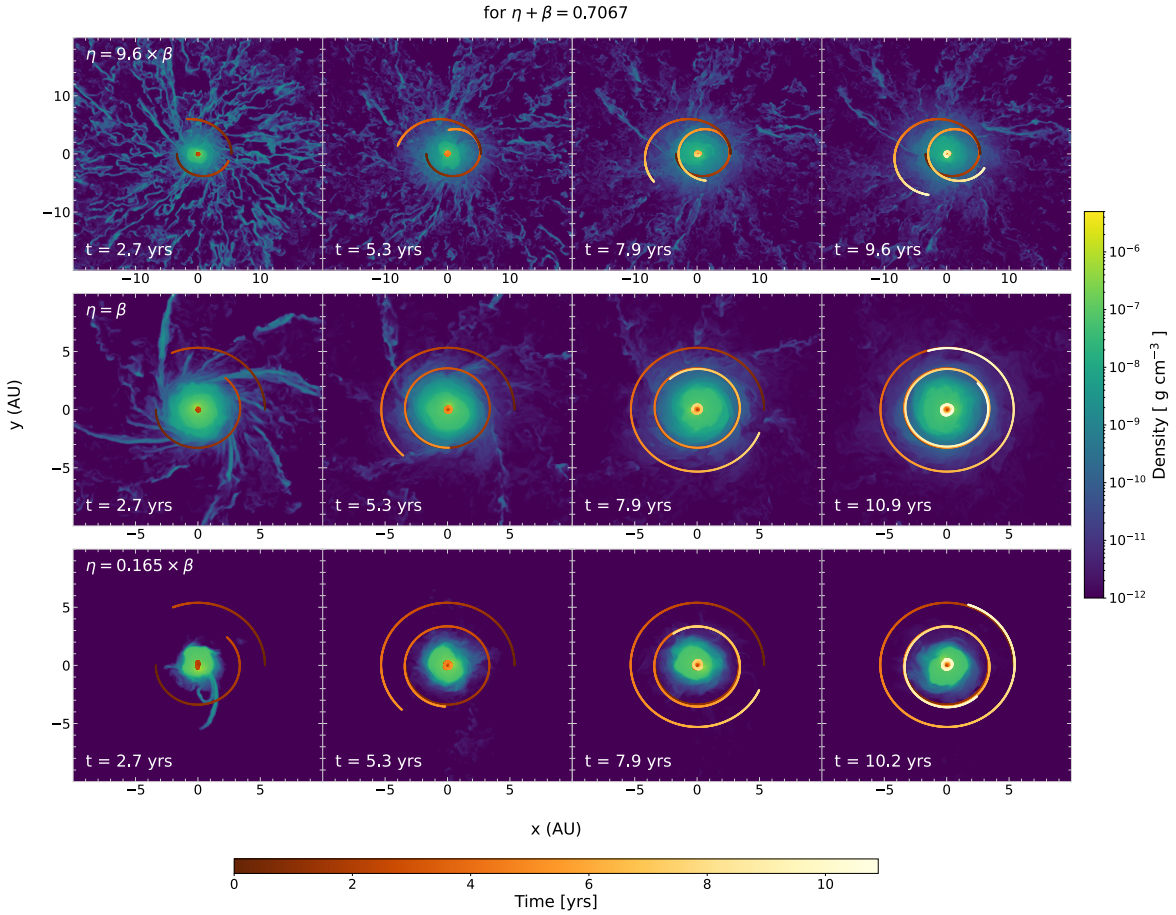


Figure 3.1: 2D slices of gas density distribution in x-y plane with maps in last column are for the latest snapshot available for each simulation. Top row shows the full computational domain of 40 AU, middle and bottom row are zoomed-in on the 20 AU region of the box, with logarithmic color map for density. Time evolution of particle trajectories are over plotted.

3.3 Results

A total of eight simulations are performed with varying energy components of the envelope gas. This energy budget governs the expansion and ejection. In Fig. 3.1, gas density maps are shown for set 1 $\eta + \beta = 0.7067$ along with the temporal evolution of orbital trajectories. For simulation A1 (last row of Fig. 3.1), thermal energy is higher than the kinetic energy of the envelope resulting in lower bulk velocity compared to I1 and M1 case. The over pressure region slowly relaxes as equilibrium is maintained quickly across the envelope. Therefore, the envelope expands slowly instead of strongly moving the envelope layers outwards. No finger-like expansion is observed. Mass within the planetary orbits remains the same for the simulated time of two complete orbits for the inner planet and one complete orbit for outer planet.

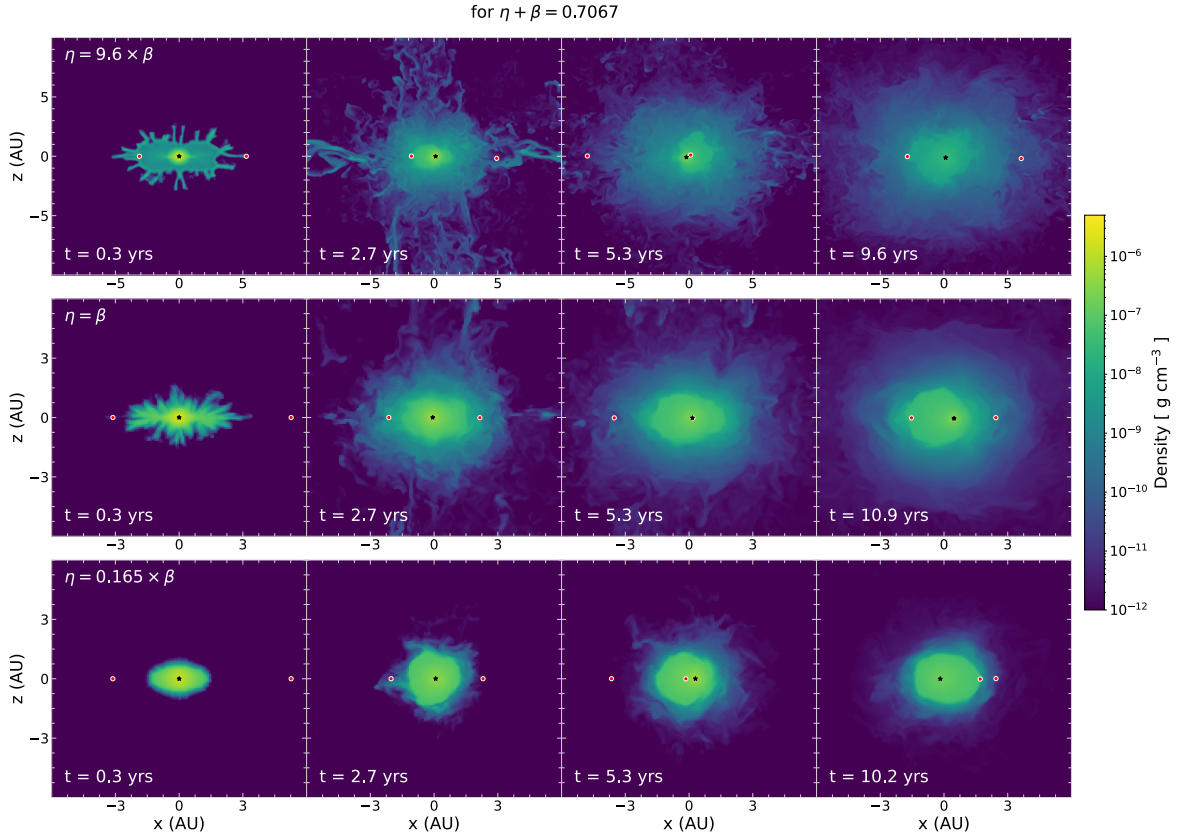


Figure 3.2: Density slices in x-z plane for set 1: I1, M1 and A1 in top, middle and bottom rows respectively. Box size for I1 is 20 AU whereas for M1 and A1 is 12 AU. Last column presents the maps for final snapshot of each run. Planets are presented by red dots and the binary star point particle at the center by black star. Since the planets are orbiting very close to x-y plane, their positions remain close to z=0.

In case of M1 (Fig. 3.1 middle row), orbits of the planets are negligibly perturbed as very small amount of mass is removed from the orbits due to lower bulk velocity compared to I1 case (Fig. 3.1 top row). For M1, mass is pulled back into the orbit by the massive central distribution. A1 and M1 cases turn out to be adiabatic scenarios since mass changes negligibly over around two orbits.

At the onset of I1 run, bulk velocity of gas in the outer layers of the envelope is larger than the sound speed leading to expansion of more mass into the domain. Mass is reduced from the orbit of the planets which results in the increase in their orbital separations. During the evolution, fluid parcels with velocity greater than escape velocity are ejected from the system leading to 0.26 $M_\odot$ removed from the grid. The lifted but bound material is pulled back by the central gas distribution and the binary point particle, resulting in clearing up of the computational domain. Total fallback mass in a spherical volume of radius 5 AU is 0.042 $M_\odot$ (with origin as the center of mass). Due to low density of the envelope material at the position of planets, gravitational drag force acting on the planets is insignificant compared to the gravitational force of the material interior to planet's orbit, for the given mass of the planets.

The direction of expansion and ejection of the CE material is governed by geometry of the

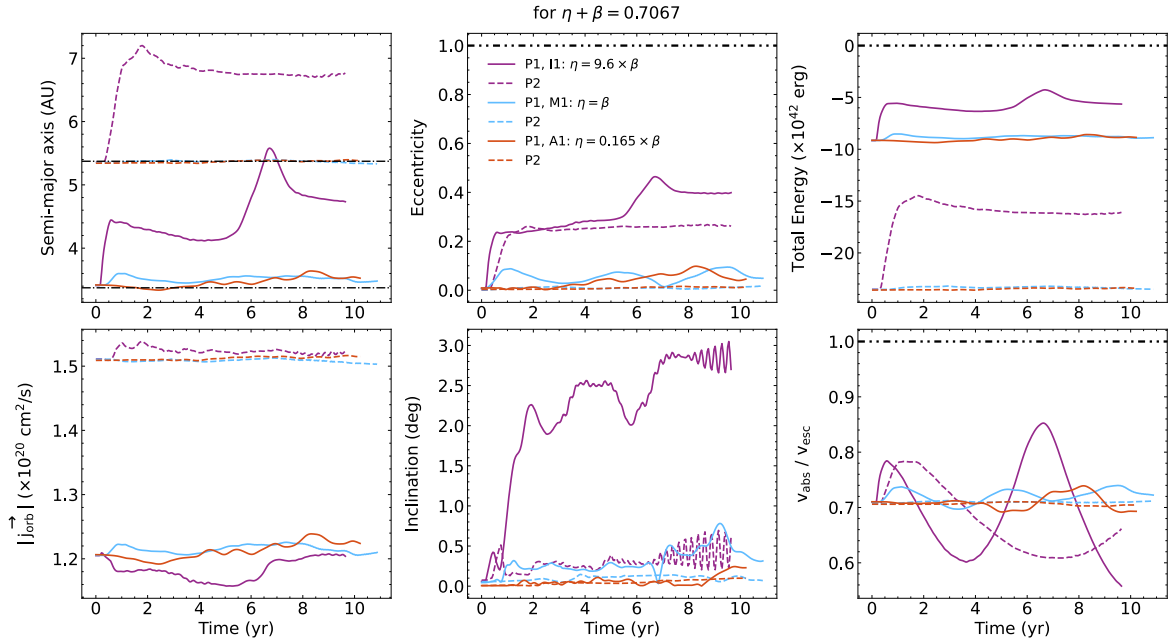


Figure 3.3: Osculating orbital properties of two planets for simulations of set 1: I1, M1 and A1, calculated using center of mass of the entire box as reference frame. Solid curves correspond to planet 1 (P1) and dashed curves to planet 2 (P2). Black dash-dot lines in semi-major axis panel show initial values of 3.374 AU and 5.373 AU. Black lines show the threshold where planets become unbound: eccentricity = 1, total energy = 0 and velocity ratio = 1 in their respective panels.

velocity field. Although the radial velocity is spherically symmetric which results in isotropic expansion of the spherical envelope, the tangential velocity imposes axisymmetry due to solid body rotation around the z-axis resulting in larger bulk velocity near the equators than the poles, thereby breaking the spherical symmetry. Higher ejection is observed around the equatorial region than the polar, shown in the density maps in x-z plane for simulations in set 1, Fig. 3.2.

Envelope develops finger-like structures at the edge moving outwards into the initially static, hotter and diffuse ambient medium. A low pressure region is created between the inner high pressure layers of the envelope close to the binary star point particle and the outward moving layer. The outward layer begins to decelerate and falls back onto the center, mixing with the inner layers and heating up the gas. The increase in heat cannot escape the system due to adiabatic equation of state leading to an over-pressured region that moves the layers outward. This material that accelerated outwards results in significant mass loss for I1 case even though the sum of kinetic and thermal energy was set lower than the potential energy at the onset of the simulation. By the end of the simulations, bound material remains extended in z-direction due to the high pressure support, Fig. 3.2.

Two types of instability which can generate finger-like structures at the interface are Rayleigh-Taylor (RTI) and Vishniac Instability. Vishniac Instability is supposed to occur in thin, cold and compressed shells which require either the presence of radiative losses or occurs in the case of $\gamma \lesssim 1.2$ (for adiabatic EoS, mimicing strong compression) (Ryu and Vishniac [1987]). In this work, adiabatic EoS is utilized with $\gamma = 5/3$ with no cooling, for which the interface is found to be stable. Therefore, the fingers are likely due to the Rayleigh-

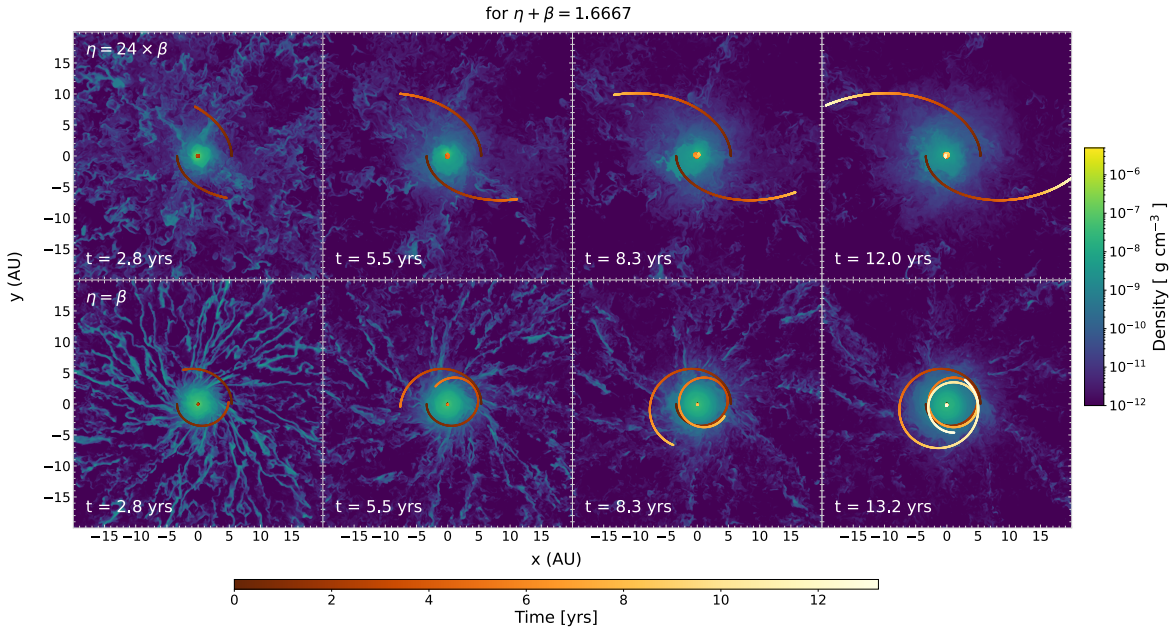


Figure 3.4: Similar to Fig. 3.1, density distributions in x-y plane presented for set 2: I2 in top row and M2 in bottom row. Both the planets remain bound in I2 and M2 case but move to wider and eccentric orbits.

Taylor instability which occurs at the effectively decelerating interface as it expands into the static lower density ambient medium. Chamandy et al. [2019, 2024] are other numerical works of expanding and ejecting CE where such structures have been found. Varying number of these fingers are seen in I1 and M1 case. The amplification factor of RTI is dependent on effective deceleration of the interface, density contrast at the interface and the excited wavelength modes (Taylor [1950]). Varying number and lengths of these fingers might be a combined effect of these factors between the runs of set 1, study of which is beyond the scope of this work.

The center of mass reference frame required to quantify the orbital properties is calculated using all the contents of the computational box: all gas on the grid (including low density ambient medium) and the 3 point particles (for further discussion on choice of frame of reference, see appendix A.1). Mass interior to the orbits of both the planets is identical at the beginning of the simulations when bound material is centrally concentrated and the two planets sit well outside it. During the extended envelope phase, two planets are responding to different enclosed masses. During the ejection phase, planets do not experience a purely Keplerian potential.

Osculating orbital elements for the planets are calculated using the cartesian state vectors at each instant. The expressions used to obtain orbital elements are mentioned in section 1.3. Central mass is defined as the mass enclosed inside the sphere, where its radius is defined by the planet's instantaneous separation from the center of mass of the system. Dynamic mass ratio $\mu_{\rm dyn}(\rm t)$ for each planet is defined as follows:

$$\mu_{\rm dyn}(\rm t) = \frac{M_{\rm enc}(\rm t)}{M_{\rm enc}(\rm t_0)} \tag{3.1}$$

where $M_{\rm enc}(\rm t)$ is the mass enclosed within the spherical volume. It reflects the effective

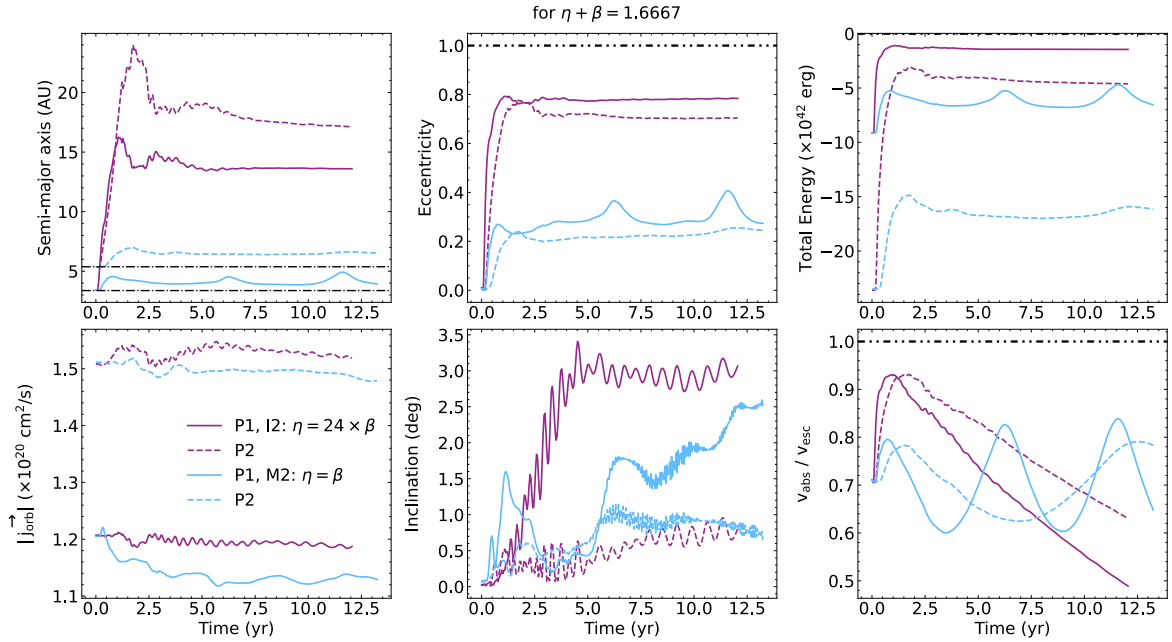


Figure 3.5: Osculating orbital elements of the two planets for set 2: I2 and M2.

change in the gravitational potential experienced by the planet over time. The value of $\mu_{\rm dyn}(\rm t)$ during maximum mass lost from a planet's orbit is reported for each simulation in the last column of the summary table 3.1.

Orbital properties of planets in set 1 $\eta + \beta = 0.7067$ are shown in Fig. 3.3. Semi-major axis and eccentricity of planets respond to the mass removed from the orbits and planets move to wider and eccentric orbits in case of I1. Oscillations found in quantities are partly due to the changes in $\rm M_{enc}(t)$ and the frame of reference chosen for their calculation. All the planets from set 1 are on bound orbits as expected for the adiabatic and instantaneous scenario with mass loss less than 50% (Völschow et al. [2014]). The inner planet undergoes strong interaction with the gas around t=6 yr which are reflected in its orbital properties.

In Fig. 3.4, gas density distributions in x-y plane for the two simulations I2 ($\eta = 24 \times \beta$) and M2 ($\eta = \beta$) from set 2 $\eta + \beta = 1.6667$ are presented. The density distributions are anisotropic for both the cases. Initially the gas structure is filamentary and dense across the domain but slowly the envelope settles into centrally dense distribution, same as set 1. Figure 3.5 shows the orbital properties for set 2. For I2 case, the planets leave the computational domain but remain bound to the system till the time they are tracked on grid. Similar to set 1 planets move to wider and eccentric orbits. Both the planetary orbits develop small inclinations but the inner planet ($\sim 3°$) is found to be more inclined than the outer planet for both I1 and I2 case.

Similarly the density distributions for set 3 are presented in Fig. 3.6. Maps of both I3 (top row) and M3 (bottom row) show anisotropic mass distribution in x-y plane (initial orbital plane of the system). A clear depiction of mass being pulled back is seen as the blob of gas turns into an elongated structure in I3 slices. I3 case corresponds to the instantaneous scenario as more than 50% mass is lost by t=0.5 yr of evolution resulting in unbinding of the planets, in accordance with the analytical benchmark (Völschow et al. [2014], Veras and Tout [2012]). From the eccentricity, total energy and velocity ratio panels in Fig. 3.7, planets are

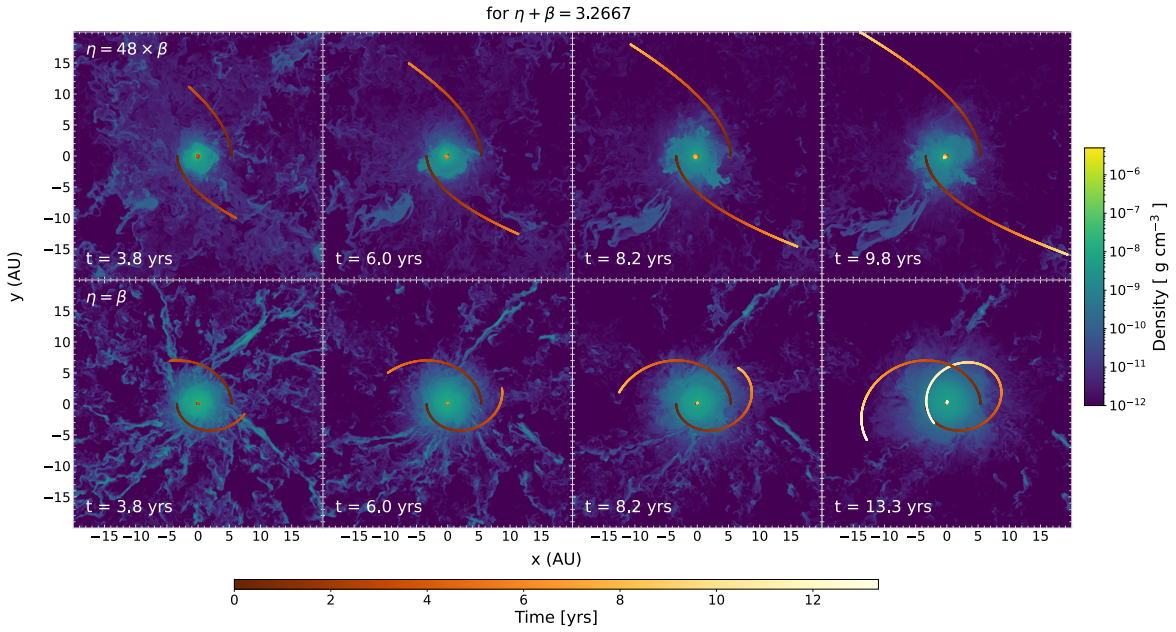


Figure 3.6: 2D density slices in x-y plane for group 3: I3 presented in the top and M3 in the bottom row with planet trajectories over-plotted. Both the planets are unbound and leave the computational domain in I3 case.

unbound around t=0.5 yr of evolution and are decoupled from the system before completing their first orbit. Whereas for the M3 model initiated with equal parts of kinetic and thermal energy, planets are on bound but wider and eccentric orbits by the end of $\sim$ 13 yrs. Similar to I3, model I4 (Fig. 3.8) also results in unbinding of planets (Fig. 3.9) in less than half a year of evolution due to sudden mass loss of 58%.

Variation of mass of gas on the computational domain with time is presented for all the runs in Fig. 3.10. The mass lost from the grid in I1 and M2 model is similar but the orbital properties of the planets show different evolution for the two models, in particular the inner planet (P1).

In Figs. 3.11 and 3.12, semi-major axes and eccentricities from kinetic energy dominated (I) runs are compared with the analytical relations (Eq: 1.14 and 1.15) for initially circular planetary orbits derived by Völschow et al. [2014]. All the curves begin with $\mu_{\rm dyn} = 1$, where the eccentricity of planets is zero given the initially circular orbits. The corresponding semi-major axis of planets are their initial separations. Grey curves for adiabatic and instantaneous analytical relations are obtained using the dynamic mass ratio per planet per simulation.

Initially the evolution of semi-major axes for both the planets follows the instantaneous curve but diverges soon from the theoretically expected values for I1 case, in column 1 of Fig. 3.11. As the semi-major axis increases, orbits of both the planets respond to larger mass enclosed due to the extended envelope structure and moves to smaller semi-major axis. Semi-major axes of planets in I2 run follows the instantaneous relation closely in the beginning. Semi-major axis of planet 1 is almost constant by the end of the simulation whereas it is decreasing for planet 2. This analysis is not performed for I3 and I4 runs as both the planets are ejected at the beginning of the simulation itself. Both planets in I1 and I2 runs move out to wider orbits than what is theoretically expected for the respective mass ratios before

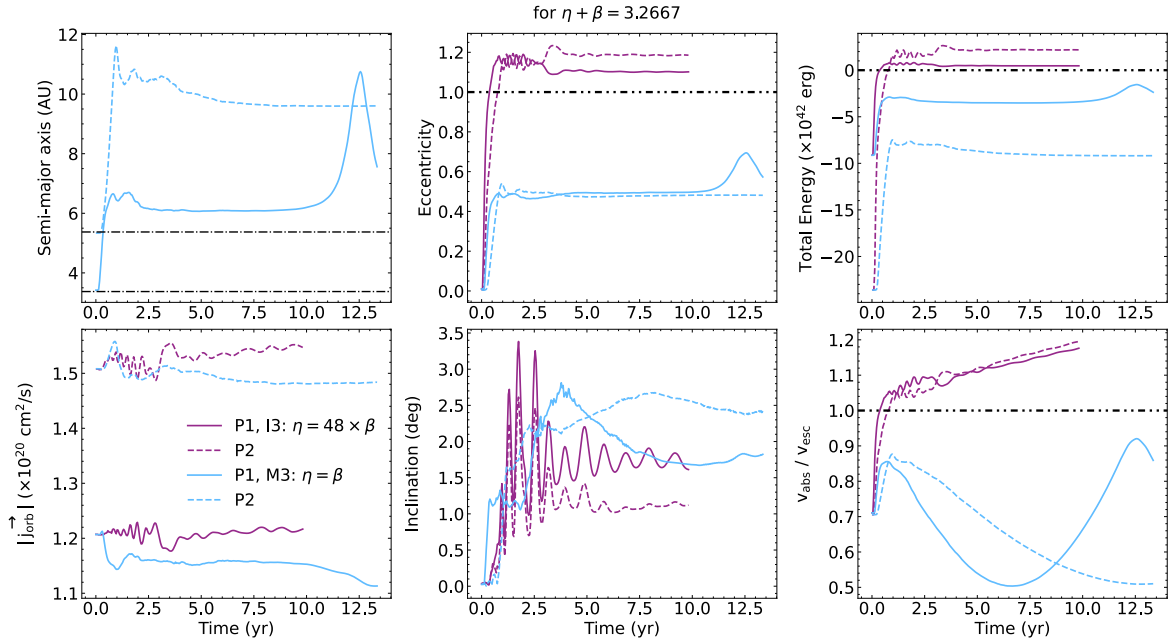


Figure 3.7: Orbital properties for the planetary systems in set 3: I3 and M3. Planets in I3 run are unbound at barely 144 days into the evolution.

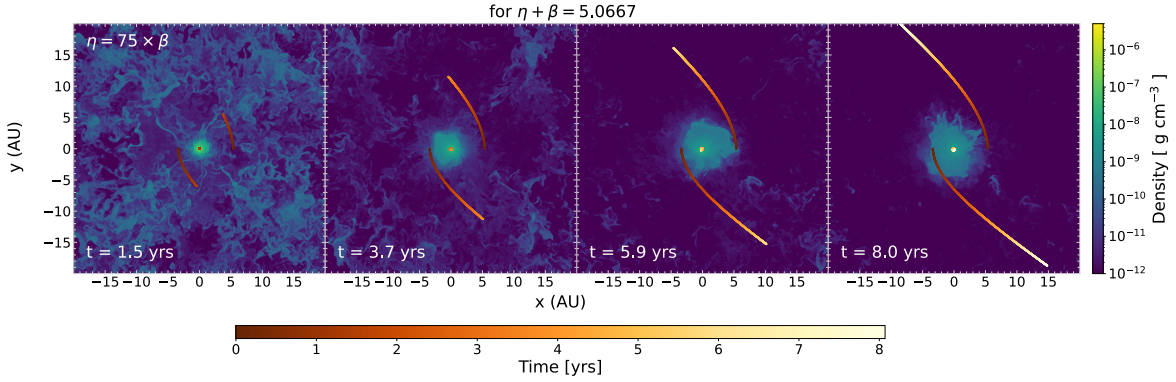


Figure 3.8: Density slices for simulation I4 with planet trajectories overlaid.

decreasing again.

Figure 3.12 shows that the eccentricity of both the planets from I3 and I4 simulations (column 3 and 4) follows the instantaneous analytic relation closely as the dynamic mass ratio decreases with time during ejection phase. These simulations can be treated as effectively instantaneous scenarios. The deviations from analytic curves for both planets are significant for the lower kinetic energy models I1 and I2 because the material has lower velocity and remains extended into the domain for longer times leading to gas-planet interaction. Whereas for I3 and I4 runs material ejects with high velocities, planets flung out to wider orbits and the computational domain clears up faster. Planets effectively experience keplerian potential in these simulations.

For I1 case, eccentricity of planet 1 is approximately constant with increasing mass ratio towards the end of the simulation (marked by square) corresponding to the decrease in semi major axis. Such varying behaviour cannot be captured in studies which assume a mass

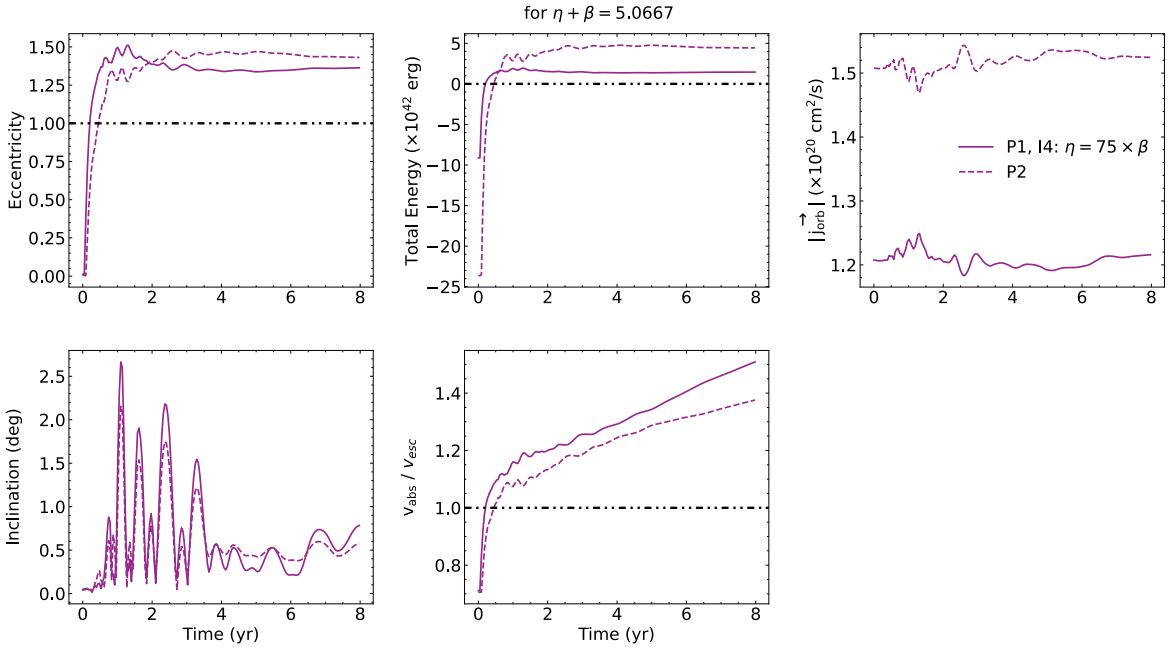


Figure 3.9: Same as Fig. 3.3, for the planetary system in model I4.

loss function throughout the evolution by assuming central gravitating body to be a point mass. A planet will not encounter an extended body where the mass enclosed changes with increase in the semi-major axis or eccentricity of the orbit. Moreover, such a model will only capture the mass loss scenario and not the increase during the fallback stages of an envelope.

Osculating orbital properties of two planets in the same simulation are different because they experience varying mass enclosed from the beginning of the mass loss event, given their initial orbital separations. Orbital separation of the planet just prior to the amount and rate of change in central mass, decides the type of mass-loss scenario observed by that planet. In a multi-planet system, planets view the same common envelope event as different mass-loss events depending on their orbital separation. As can be seen in Fig. 3.11, analytical curves for planet 2 (outer planet) in I1 run are steeper than those for planet 1.

In Fig. 3.13, a similar analysis for semi-major axis is presented for KE =TE models (M2 and M3). While planet 2 in M2 model follows the instantaneous curve closely with slight deviations, planet 1 (inner planet) does not follow any analytical curve throughout the evolution and follows a complex dynamics. For M3 run, both the planets follow the instantaneous curve initially but then deviate from both the analytical curves. Interestingly, semi-major axis of planet 1 remains in the range of 6-11 AU while the instantaneous curve predicts higher semi major axis values. Each planet in M2 and M3 simulations experiences different mass loss scenarios. Figure 3.14 shows the variation of eccentricity with dynamic mass-ratio for KE =TE models (M2 and M3). Eccentricity and semi-major axis remains almost constant after t=6 yr for planet 2.

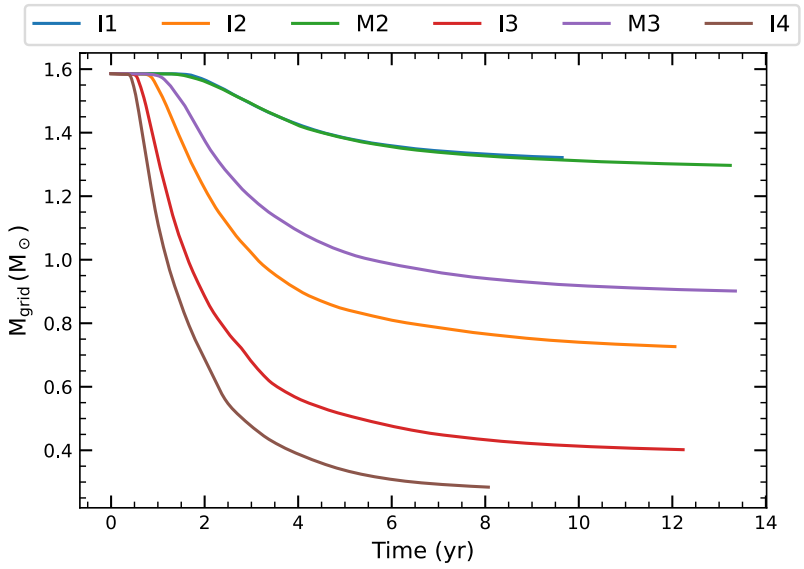


Figure 3.10: Time evolution of total gas mass on the computational domain (M_{grid}) for all the I and M models in which mass loss is observed.

Run	ζ	v_{edge} (km/s)	Ω (1/s)	v_ϕ (km/s)	μ_{dyn} P1, P2
ζ_0.1	0.1	59.91	1.55×10^{-6}	232.4	0.491, 0.494
ζ_0.5	0.5	114.72	1.33×10^{-6}	198.96	0.471, 0.472
ζ_1	1	140.5	1.15×10^{-6}	172.34	0.467, 0.473
ζ_2	2	162.24	9.41×10^{-7}	140.77	0.503, 0.516

Table 3.2: Initial Properties of mass-ejection models with varying radial-to-rotational kinetic energy ratio, ζ keeping $\eta = 3.2$ and $\beta = 1/15$ constant which ensures that total KE, TE and PE are constant for this set of runs. Similar to table 3.1, μ_{dyn} column presents the dynamic mass ratio corresponding to the maximum loss of gas from the planetary orbits.

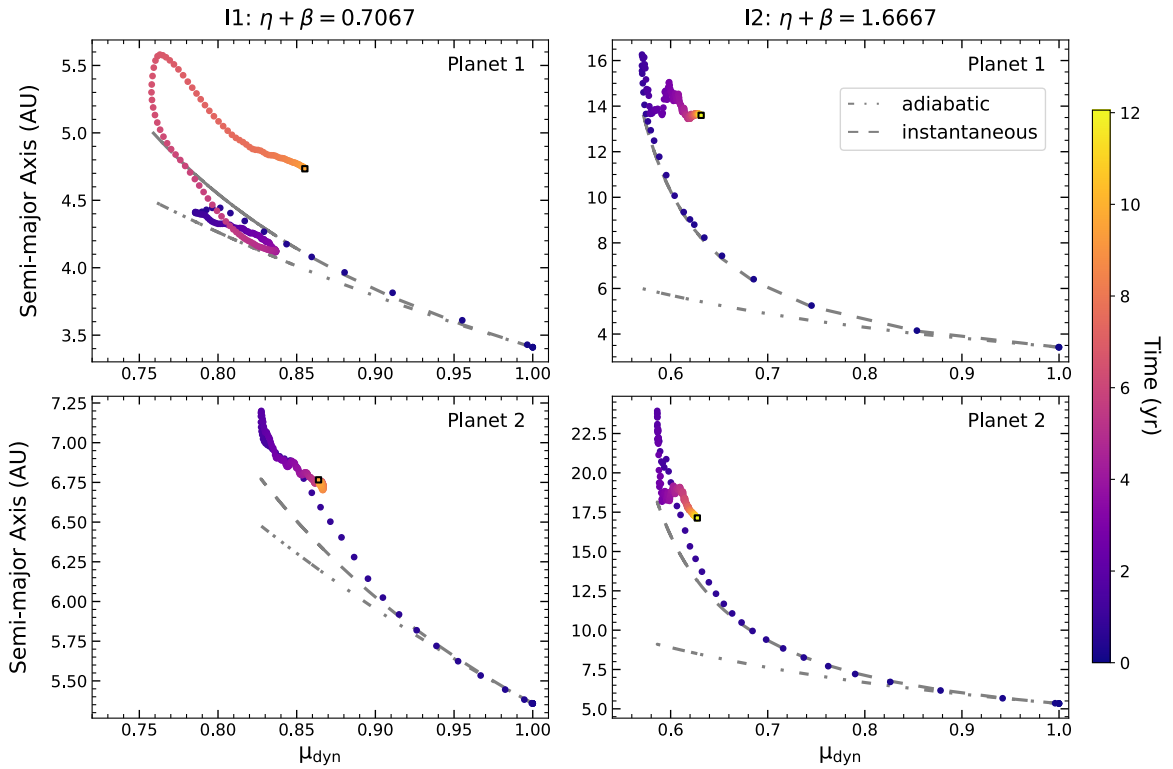


Figure 3.11: Variation of semi-major axes of planets with dynamic mass-ratio $\mu_{dyn}(t)$, color mapped for simulations I1 in column 1 and I2 run in column 2. Rows 1 and 2 correspond to planet 1 and 2 respectively. Grey curves depict the semi-analytical results from Table 2 of Völschow et al. [2014] for the 2 asymptotic cases, namely adiabatic (dash-dotted) and instantaneous (dashed).

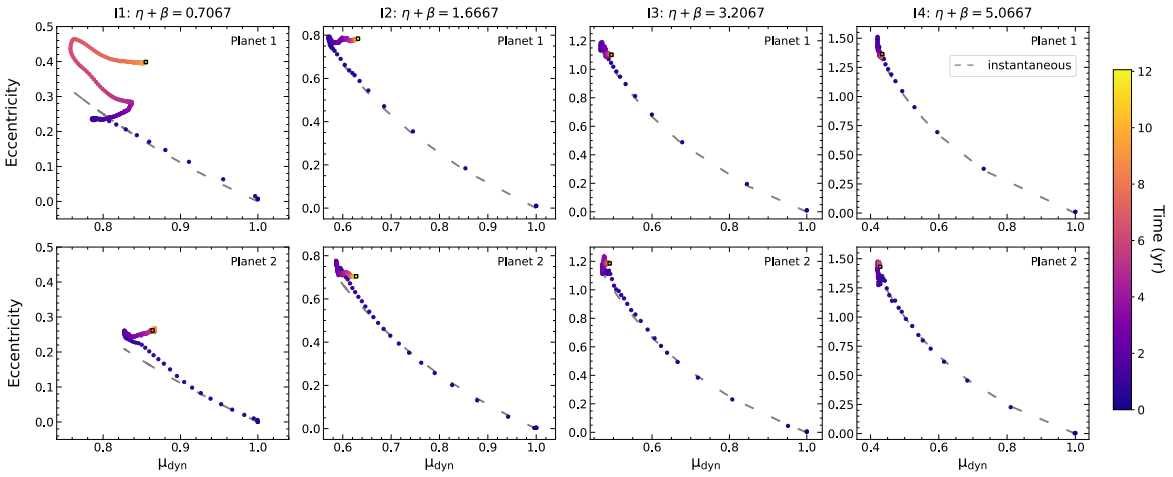


Figure 3.12: Eccentricity of planets plotted with dynamic mass-ratio for runs I1 to I4 from left to right columns respectively. Rows 1 and 2 correspond to planet 1 and 2 respectively. For planets initialized on circular orbits (as in this work), eccentricity remains zero through the mass evolution for adiabatic mass loss. Grey curve depicts the semi-analytical result for instantaneous scenario (dashed curve) (from Table 2 of Völschow et al. [2014]). I2, I3 and I4 can be treated as instantaneous cases but I1 deviates, therefore falls in intermediate regime.

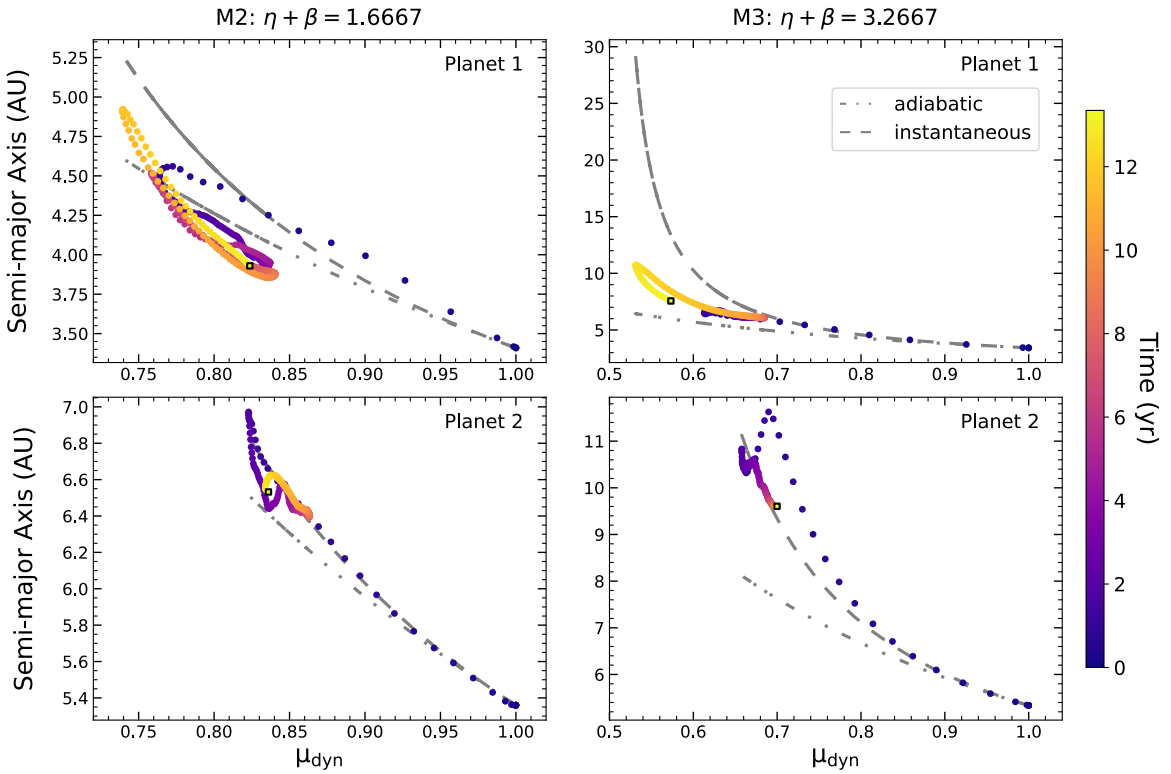


Figure 3.13: Similar to Fig. 3.11, for M2 and M3 runs. Semi-major axes evolution with dynamic mass ratio for both the planets does not follow either of the analytical curves. M2 and M3 cases fall in intermediate regime.

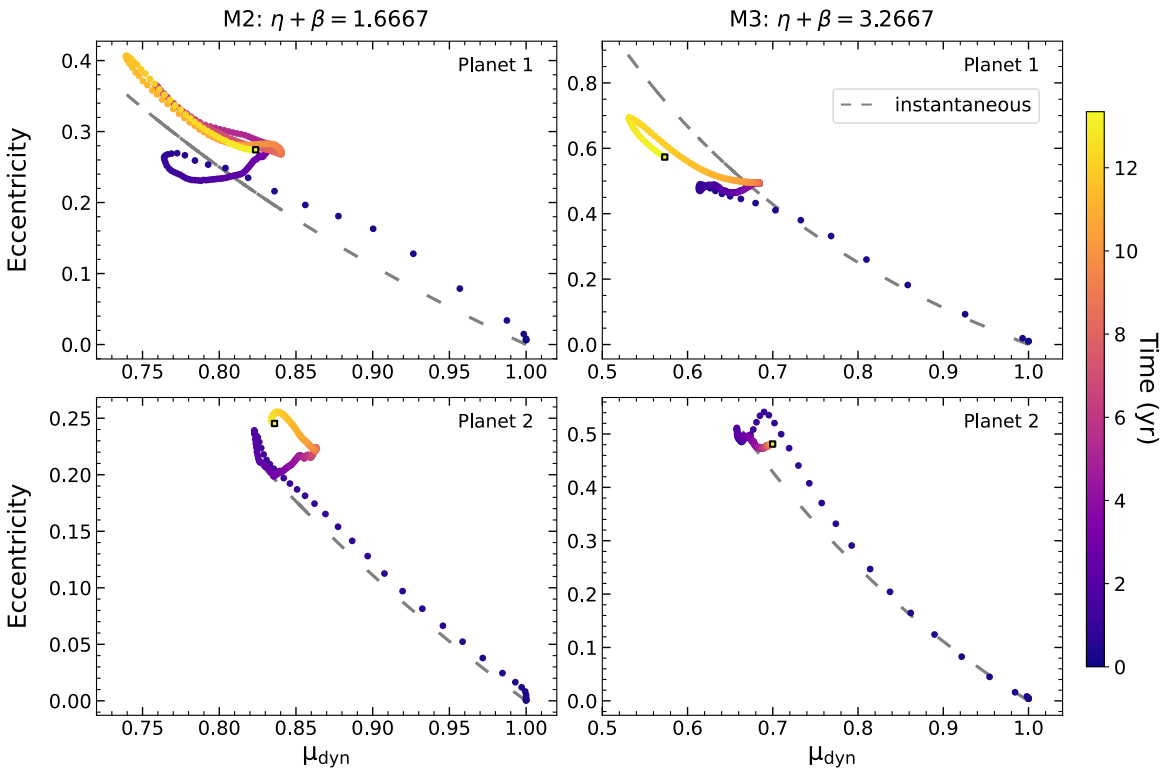


Figure 3.14: Similar to Fig. 3.12, eccentricities with dynamic mass-ratio are presented for intermediate cases M2 and M3.

3.3.1 Varying initial radial and rotational support to CE

As a sub-group of instantaneous mass ejection events, initial radial and rotational kinetic energy of CE is varied to study its effect on the planetary orbits and the amount of unbound mass. To achieve this, $\zeta = \mathrm{KE_{rad}}/\mathrm{KE_{rot}}$ parameter is varied. Total kinetic energy parameter, $\eta = 3.2$ and thermal energy parameter, $\beta = 1/15$ is kept fixed. These correspond to I3 run which produces $\sim 50\%$ mass loss. As the common envelope is found to be more rotationally supported than radial (Ricker and Taam [2012], Vetter et al. [2024]) two models are explored in $\zeta < 1$ range, one in $\zeta > 1$. These 3 models are compared to the $\zeta = 1$ I3 case, details of which are present in previous section. In table 3.2, initial parameters for the simulation suite are mentioned.

Figure 3.15 displays the density distribution in x-y plane for simulations with different ζ values. The gas morphology is significantly different for the high rotation energy $\zeta = 0.1$ case, which is filamentary than the clumpy distribution in $\zeta = 2$ high radial energy run. Towards the end of the simulations, high rotation run shows compact gas distribution as compared to the more diffused structure in high radial energy scenario. Both planets leave the computational domain by the end of the runs. In Fig. 3.16, amount of gas mass lost from the computational grid over time is shown for all the four simulations. Models with high rotational energy ($\zeta = 0.1, 0.5$) show steeper decrease in mass as compared to the high radial energy ($\zeta = 2$). By the end of the simulations, similar amount of mass is removed from the grid in all the four cases. Unbound mass exhibits a non-monotonic response with respect to decreasing ζ parameter.

Figure 3.17 shows eccentricity, total energy, specific orbital angular momentum and ratio of absolute to escape velocity for the two planets, for the group of simulations in table 3.2. Both planets in cases of higher $\mathrm{KE_{rot}}$ than $\mathrm{KE_{rad}}$ are unbound with eccentricities and velocity ratio greater than unity. Planets in the higher radial energy case $\zeta = 2$ appear marginally bound by the end of the simulations as the total energy of the planets is only slightly less than zero, similar feature can be seen in the eccentricity and velocity ratio curves as well. In all the four simulations, planets leave the domain by the end of the simulations and it is difficult to conclude whether the higher radial energy ($\zeta = 2$) scenario could harbor bound planets in the event of $\sim 50\%$ mass loss.

Limitations: During the evolution, ejecta spreads into the entire computational domain and eventually leaves the boundaries. Second derivative of gas density is employed as resolution criterion for adaptive mesh refinement. This criterion along with the self gravity module makes the runtime for simulations longer. Therefore, a better resolution criterion is needed to run higher resolution simulations. Osculating elements for orbital properties are reported for all the simulations in this work which depend on the instantaneous mass enclosed within the orbits. These elements are subject to the changing instantaneous mass within a single orbit resulting in oscillations in the orbital properties with time Adams et al. [2013]. Orbital averaging is a way to obtain properties for single orbit but in this work planets barely complete one to two orbits. Additionally, the planets are not subject to purely keplerian potential, during the extended envelope phases. Therefore, the osculating elements reported are indicative during those stages and more robust quantitatively when the envelope settles to a centrally concentrated distribution in the early stages and by the end of the simulations.

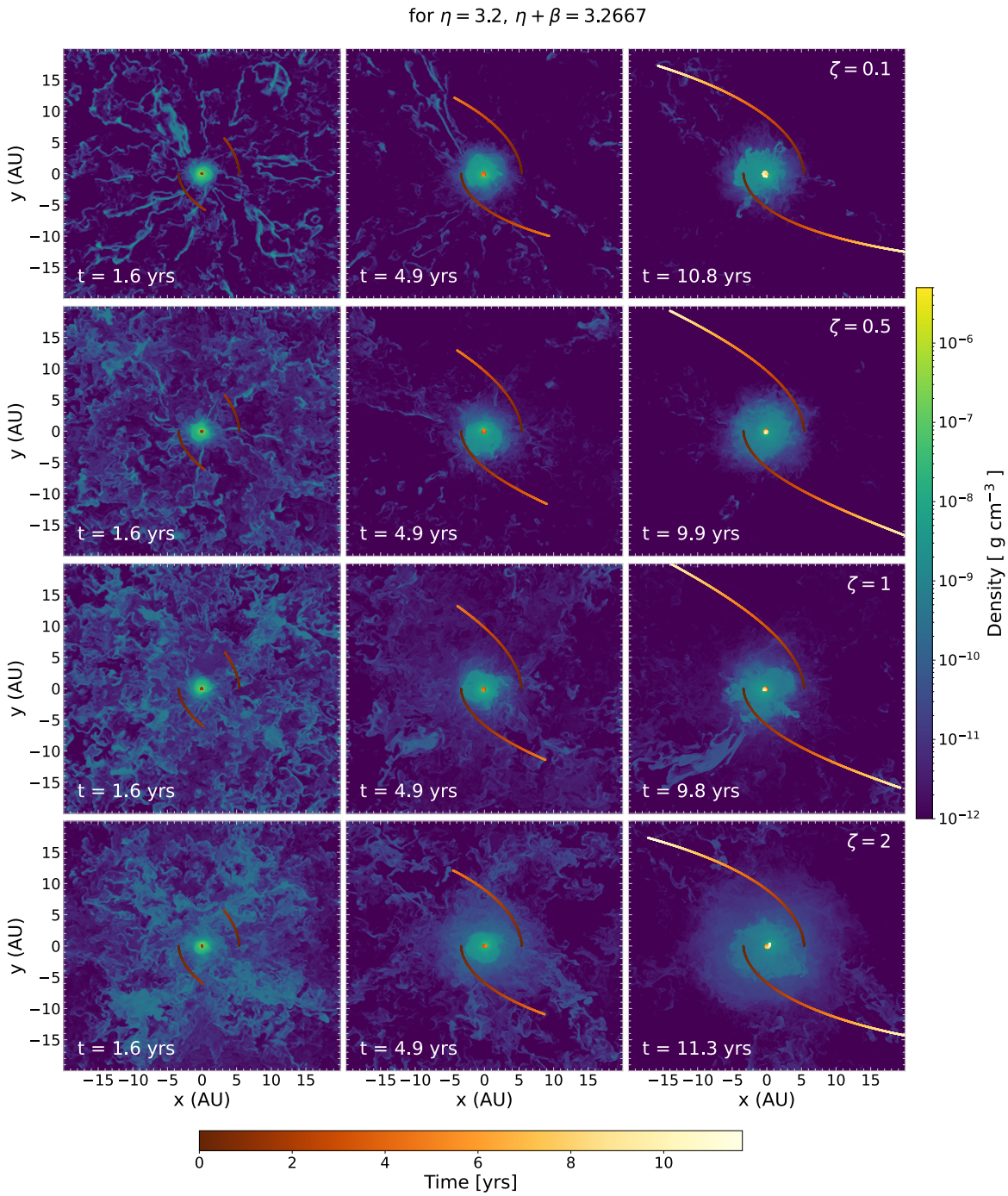


Figure 3.15: Density slices in x-y plane are presented for the four runs with increasing $\zeta = \mathrm{KE_{rad}}/\mathrm{KE_{rot}}$ parameter from row 1 to 4. Maps for different timestamps are shown from left to right columns with planet trajectories overplotted and logarithmic color map for density.

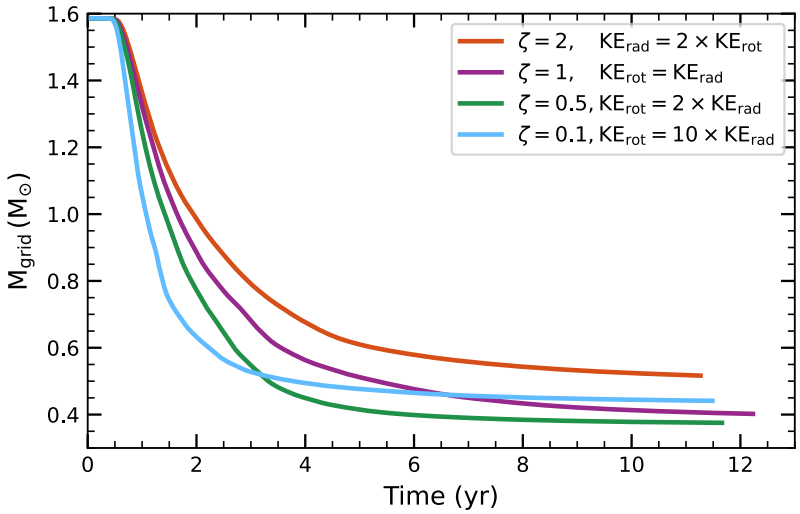


Figure 3.16: Time evolution of mass on the computational grid ($\mathrm{M_{grid}}$) for simulations with varying radial to rotational kinetic energy of the gas (ζ). Decrease in mass becomes steeper from $\zeta = 2$ to $\zeta = 0.1$ initially but by the end of the simulations non-monotonic dependence is found between $\mathrm{M_{grid}}$ and ζ.

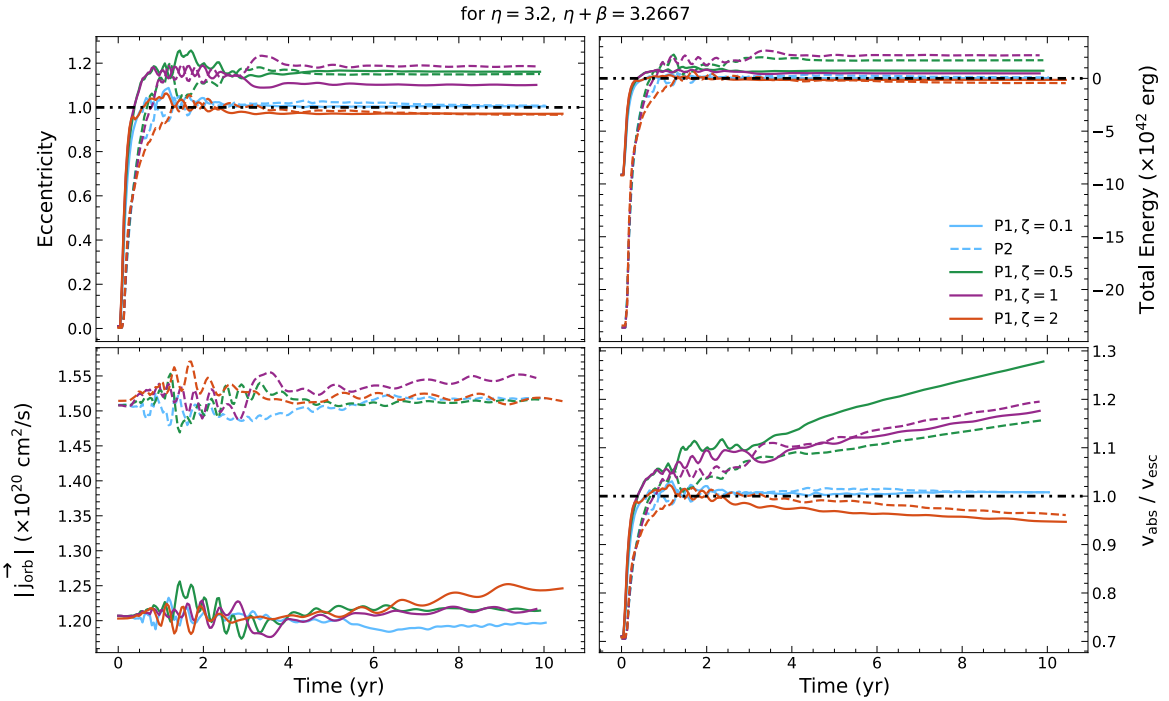


Figure 3.17: Time evolution of kinematic properties of planets for ζ runs. While both the planets from $\zeta = 2$ ($\mathrm{KE_{rad}} = 2 \times \mathrm{KE_{rot}}$) simulation appear marginally bound, planets in the other three runs are unbound from the system.

3.4 Summary and Conclusions

To model the impact of common envelope mass ejection events on the circumbinary planetary orbits, 3D global hydrodynamic simulations are performed to identify whether first generation planets sustain the common envelope event and remain bound. Mass loss of varying timescales is generated by exploiting the energy budget of the gas envelope. Two planets are initialized on circular coplanar orbits which interact with the asymmetric extended gas structures. The main results from this work are summarized below:

- For A1 and M1 case, planetary orbits are negligibly affected due to zero mass loss during almost two orbits modeled for the inner planet and one orbit for the outer planet. These cases depict adiabatic (slow) mass loss scenarios.
- In case of instantaneous mass loss rate, negligible interaction of planets with the envelope is a good approximation to derive the final orbital parameters. Planets are unbound for mass fraction $\leq 50\%$ (I3, I4 runs) in the case of rapid mass loss event, in agreement to the results found by analytical studies Völschow et al. [2014], Veras and Tout [2012].
- Planets move to wider and eccentric orbits for instantaneous and intermediate mass loss scenarios (I and M models).
- For envelope ejection models I1, I2, M2 and M3: orbital parameters significantly deviate from the analytical curves for the two extreme cases of slow and rapid mass loss, and planets interact with the extended gas structures. These simulations depict intermediate mass loss scenarios. No clear analytical relation between the initial and final orbital elements with the dynamic mass ratio for intermediate scenarios could be obtained as their fate is subject to non-linear interactions.
- Each planet in the system experiences the same CE event as different mass loss scenario depending on its orbital separation. Simulations show that once mass is ejected, bound and low kinetic energy ejecta is pulled back by the central mass leading to decrease in semi-major axis of planets. Therefore, fate of a planet is decided by the rate and amount of change of mass from the orbit spanned by instantaneous position of the planet, which is non-linear in the case of CEE.
- Varying radial and rotational support of gas, $\zeta = \mathrm{KE_{rad}}/\mathrm{KE_{rot}} < 1$ for instantaneous mass ejection event I3 (50% mass loss) results in similar orbital configurations of the planet. In case of higher radial kinetic energy ($\zeta = 2$), planets appear marginally bound but it cannot be concluded if they are saved upon further evolution since they leave the domain boundary.
- Non-monotonic relation is found between the lost common envelope material and the initial ratio of radial to rotational energy. Mass is lost faster initially in the case of high initial rotational energy but by the end of the simulations, a non-monotonic dependence is found.

First generation planets on circular coplanar orbits may survive the envelope ejection in case of intermediate mass loss scenario. Mass loss event experienced by a planet depends upon the orbital separation immediately before the ejection event. These planets will move out to wider and eccentric orbits in case of instantaneous and intermediate scenarios. In case of instantaneous mass loss event where more than 50% of the gas envelope is removed from the orbits, planets are unbound from the system.

Chapter 4

Properties of Post-CE Circumbinary Discs

4.1 Aim

One of the possible scenarios for existence of planets in circumbinary orbits around PCEBs is planet formation from the remnant bound material, after the common envelope ejection phase (Perets [2010]). A handful of studies have addressed this problem both analytically (Schleicher and Dreizler [2014], Pourmand et al. [2025]) and by performing hydrodynamic simulations of compact self-gravitating disks using ENZO code (Lichtenberg and Schleicher [2015]). Their results supported the possibility of forming massive clumps through Gravitational Instability planet formation channel, on orbital timescales of the disc at close separations within 10 AU.

To model these instabilities, constraints on thermodynamic and kinematic properties of post-CE structures are required. While some numerical works on CE have resulted in ejection of most of the envelope using recombination energy (Vetter et al. [2024], Sand et al. [2020], Reichardt et al. [2020]), these works did not include full radiative transfer calculations and assumed the recombination energy to have thermalized locally. Lau et al. [2025] showed that expanding outer layers of the envelope are optically thin where the radiation can escape and less mass is lost in simulations with radiation transport although they have not included recombination energy.

Focus of this project is to study the kinematic properties of post-ejection gas distributions to identify if they sustain coherent rotation. To address this problem, 3D hydrodynamic simulations of common envelope ejection are performed for thermodynamic extremes of instant cooling and no cooling. The aim is to quantify mass distribution of the leftover material along with its rotation budget, in order to investigate if post-CE structures could be gravitationally unstable to form clumps which could evolve into jupiter-mass planets at later times.

4.2 Parameter study

To my knowledge, simulations on CE are performed using adiabatic EoS or tabulated/OPAL EoS to account for recombination energy released. Recent numerical experiments with OPAL EoS have shown puffed toroidal circumbinary accretion disc rather than thin discs due to high thermal pressure support (Vetter et al. [2024]). The common envelope material is found to be optically thick in the deeper layers of the envelope (Lau et al. [2025]). As the envelope expands adiabatically, it cools in the outer regions and becomes optically thin from where the radiation can escape. This would allow the gas to lose thermal energy and cool, resulting in reduced thermal pressure and the gas could potentially settle into a thin disc-like structure. For the formation of a rotation-supported flattened disc, significant cooling is needed during CE evolution. This requires full radiative transport calculations to accurately model the cooling, which is beyond the scope of this work.

Run	η	ζ	KE (erg)	v_r (km/s)	v_ϕ (km/s)	EoS
η0.64_adia	0.64	0.1	4.53×10^{46}	26.79	103.92	adiabatic
η0.64_iso						isothermal
η1.6_adia	1.6	0.1	1.13×10^{47}	42.36	164.32	adiabatic
η1.6_iso						isothermal
η10_adia	10.0	0.1	7.076×10^{47}	105.89	410.80	adiabatic
η10_iso						isothermal

Table 4.1: Initial properties of the exploratory runs to identify scenarios with disc-like structures. PE is fixed at 7.076×10^{46} erg and TE at PE/15 = 4.7175×10^{45} for all the runs. Temperature at envelope front for adiabatic simulations is 4308.18 K and the same temperature is used for globally isothermal runs.

For this study, simulation setup detailed in section 2.3 is adopted. Two ideal thermodynamic scenarios of no cooling (Adiabatic) and instantaneous cooling (Isothermal) are modeled. Using the same non-dimensional parameters based on energy components of the gas envelope, mentioned in table 2.2, a set of numerical experiments are performed to identify disc-like structures after partial to high mass-ejection. Details of these simulations are presented in table 4.1 where ζ parameter is set to 0.1 for all the simulations ($\mathrm{KE_{rot}} = 10\,\mathrm{KE_{rad}}$) implying that rotational kinetic energy is significant contributor to mass loss. This choice of ζ parameter is made to ensure that the bound remnant is rotationally supported post the expansion and ejection phase.

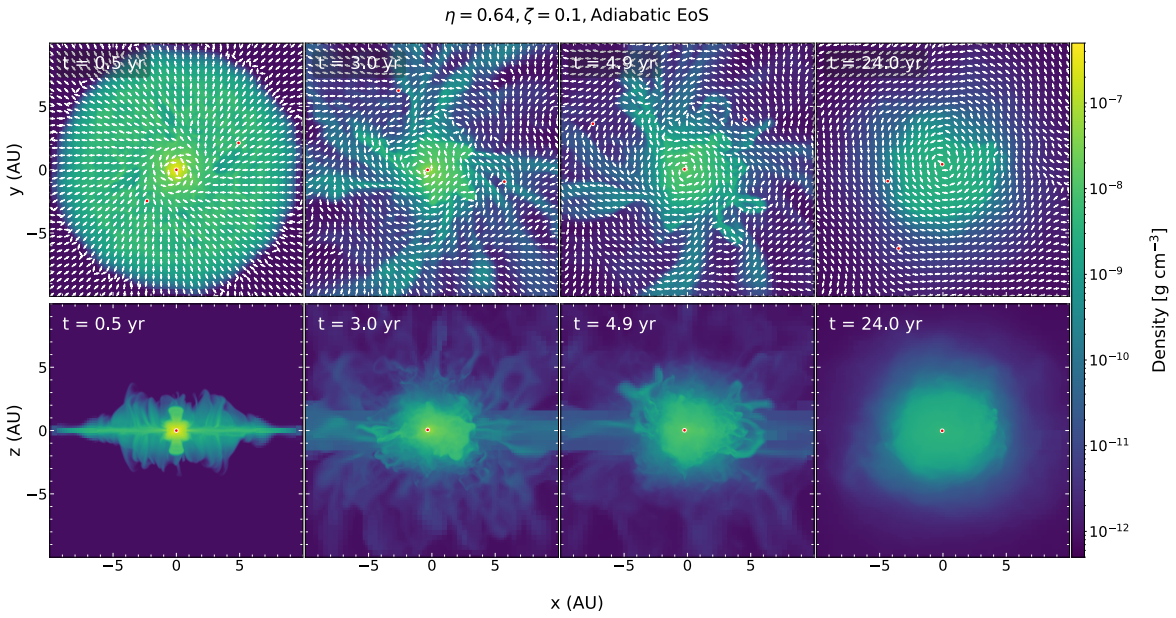


Figure 4.1: Density-weighted projection maps of density in x-y and x-z plane (with center of mass as origin) shown in row 1 and row 2 respectively (logarithmic scale), with velocity vectors over-plotted for the x-y plane at different times from left- to right-hand columns for run η0.64_adia. Final gas distribution is a geometrically thick structure. Maps are zoomed-in on 20 AU^3 region of the computational volume.

4.3 Results

In order to identify gas structures which satisfy disc-like properties different conditions are evaluated, such as clear rotation in velocity vectors, alignment of average specific angular momentum vector along a single component, if tangential velocity v_ϕ is at least twice the radial velocity v_r, and whether the mean tangential velocity is at least 0.5 times the Keplerian velocity. All kinematic properties are calculated in center of mass frame, obtained using all gas cells with $\rho \geq 6 \times 10^{-12}\,\mathrm{g\,cm^{-3}}$ inside 10 AU sphere, with the sphere centered on binary star point particle (for more details see appendix A.2).

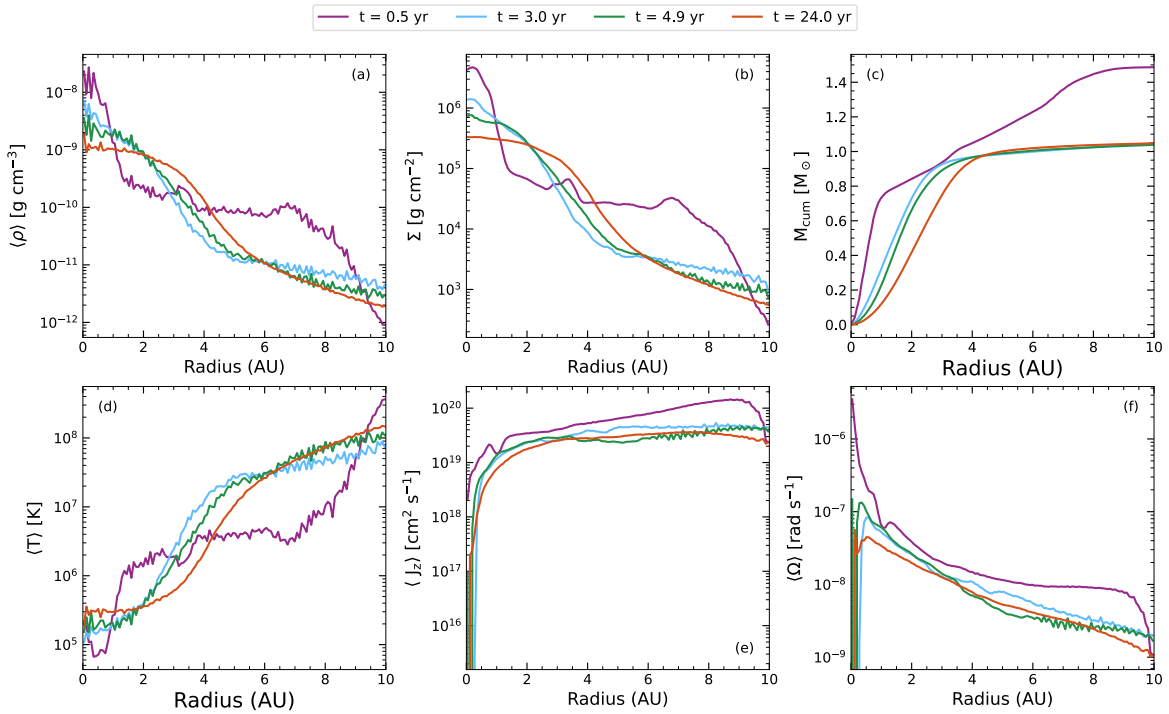


Figure 4.2: Mass-weighted cylindrically averaged radial profiles of volume density (ρ), surface density (Σ), cumulative mass ($\mathrm{M_{cum}}$), temperature (T), z-component of specific angular momentum ($\mathrm{J_z}$) and angular velocity (Ω) at same timestamps as in Fig. 4.1 for run $\eta 0.64_\mathrm{adia}$.

Three HD simulations are performed with adiabatic EoS with increasing $\eta = \mathrm{KE/PE}$ parameter leading to reduced remnant cumulative mass. In first row of Fig. 4.1, density-weighted projection plots of density of the CE material in the x-y plane (with center of mass as origin and averaged over 20 AU cubical region) are presented for the low kinetic energy simulation $\eta 0.64_\mathrm{adia}$ at four evolutionary stages: t = 0.5, 3.0, 4.9, and 24 yr (the final available snapshot). In the beginning, expanding common envelope keeps its initial rotation profile, gradually develops asymmetric rotation pattern as part of the lifted material falls back and collides with the bound inner layers (t=4.9 yr). This exists until all the fallback material has been redistributed and the computational domain has been cleared of ejecta. The bound remnant develops mostly ordered rotation around the z-axis. Gas settles into a non-spherical distribution and not a geometrically thin disc. This is due to the adiabatic EoS, therefore thermal energy cannot be removed from the gas. As a result, gas remains hot with thermal pressure supporting against gravity and maintaining a vertically extended structure.

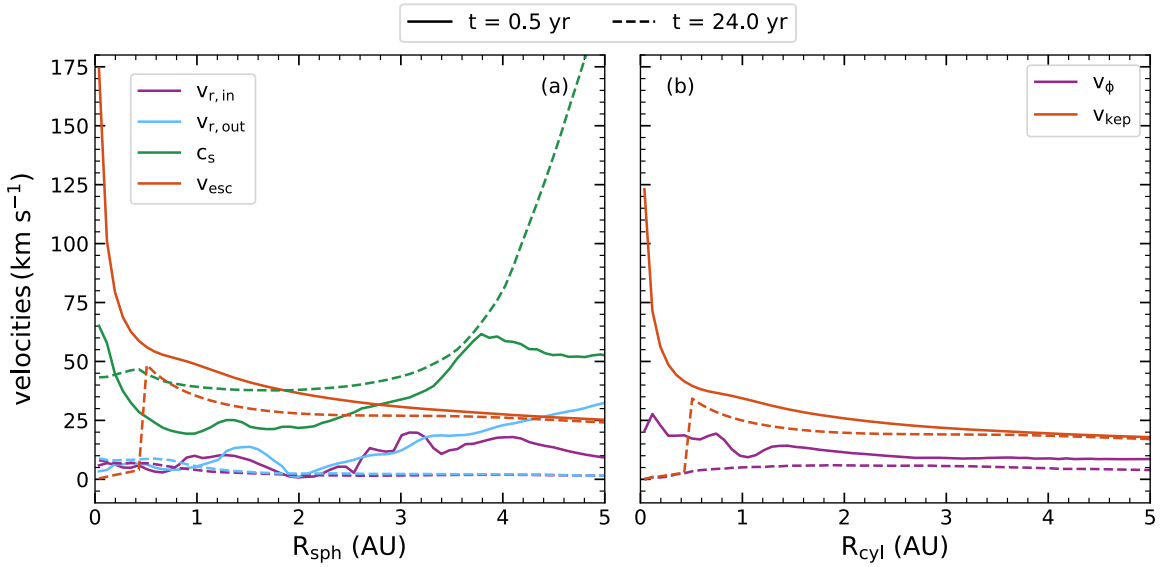


Figure 4.3: Radial profiles of velocities of inflowing ($v_{r,\,in}$) and outgoing ($v_{r,\,out}$) gas, sound speed (c_s) and escape speed (v_{esc}) in panel (a) plotted with spherical radius. Keplerian (v_{kep}) and tangential velocity (v_ϕ) profiles with cylindrical averaging in panel (b) for $\eta 0.64_adia$ simulation at time t=0.5 yr (solid lines) and t=24 yr (dashed).

Figure 4.2 shows the temporal evolution of several dynamical quantities of gas in center of mass frame with z-axis chosen as rotation axis. The properties are mass-weighted averages over cylindrical bins for the same snapshots presented in Fig. 4.1. Panel 4.2a illustrates radial profile of volume mass density from 0.5 yr to 24 yr. The outbound layers of the CE can be seen as a slight peak in density at around 3.5 AU and 7 AU at time t=0.5 yr. Decrease in gas density by an order of magnitude (from t=0.5 to t=24 yr) is found in the central region while an increase is seen in the outer regions beyond $\sim$ 3 AU at t=24 yr, depicting spread of the gas envelope with time. Gas is removed out slowly from the central region as opposed to a typical accretion disc. Similar feature is seen in the surface density profiles (volume density integrated along the z-axis) presented in panel (b). The cumulative gas mass is displayed in panel 4.2c. The mass enclosed within a cylinder of radius 5 AU and height 10 AU converges to nearly the same amount of $\sim 1.05\,M_\odot$ by the end of the simulation.

Temperature profiles in panel (d) show cooling of gas in the outer regions of 2-3 AU due to expansion at t$=24$ yr. In panel 4.2e, radial distribution of the z-component of specific angular momentum is shown. At t=0.5 yr as outer layers of the envelope are moving out (Fig. 4.1), a small peak in the curve is found at around 9 AU. Once these layers are removed, average J_z values converge to similar values with time. From t=0.5 yr to 24 yr, value of this component reduces in the inner regions as mass depletes out but in the outer regions it is similar to the values found for t=3 and 4.9 yr. Average angular velocity profiles are presented in 4.2f. Negative values for both J_z component and Ω are found in the innermost bins. Although the envelope gas is initialized with a constant angular velocity, it develops a decreasing angular velocity profile with radius. By t=24 yr, angular velocity is reduced in the inner regions by significant amount of $\sim 4.0 \times 10^{-6}\,\mathrm{rad\,s^{-1}}$ to $\sim 4.0 \times 10^{-8}\,\mathrm{rad\,s^{-1}}$. This is partly due to the expending of rotational kinetic energy in driving the ejection of gas and the depletion and spread of material to the outer regions. Although the circumbinary structure in Vetter et al. [2024] shows reduction in density and angular momentum as the material is being removed both by radial winds and bipolar outflows, they find inward flowing gas

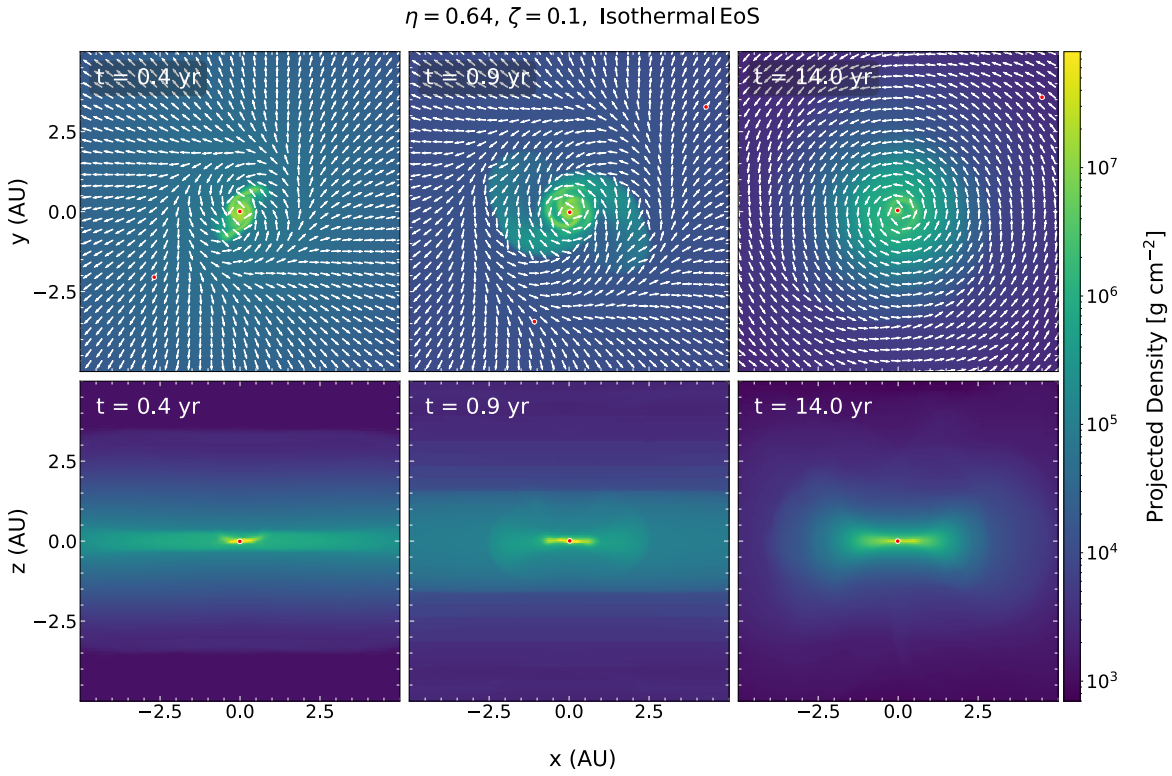


Figure 4.4: Column density maps in x-y and x-z plane in center of mass frame, at different times for $\eta 0.64_\mathrm{iso}$ simulation (showing $10\,\mathrm{AU}^3$ volume of the box) with logarithmic color map.

fueling the outflows in the inner regions similar to an accretion disc. Similar to our results, they find circularized motion of gas which is sub-keplerian and supported pressure.

Figure 4.3 displays radial profiles of various velocities at early and final stages of the $\eta 0.64_\mathrm{adia}$ simulation, corresponding to first and last snapshot of each row presented in Fig. 4.1. Inflowing and outgoing gas have approximately the same speeds which reduce with time. All the dense material is in subsonic motion and is bound by the end of the simulation since its radial velocity is less than the escape speed required. For t=0.5 yr, the solid blue curve depicting radial outflow speed is found to be greater than the escape speed for region outside 4.4 AU showing that those layers may be ejected. The Keplerian velocity at each radius is calculated using all the mass enclosed within spherical volume of that radius (gas and the binary point particle). The escape speed and keplerian velocity profile (calculated in center of mass frame) show a sudden jump at 0.4 AU because the binary star point particle is offset from the center of mass and is included into the enclosed mass from those radial bins onward. The tangential velocity (in panel (b)) is one-third of the keplerian velocity over majority of the dense gas at t=24 yr, whereas the sound speed is ~ 25 km/s. This shows that the gas distribution is pressure-supported.

For the simulation $\eta 0.64_\mathrm{iso}$ with isothermal EoS, the formation of spiral arms is seen in the projected density maps (taken over 20 AU cubical region) at time t=0.4 yr and t=0.9 yr, in Fig. 4.4. Density projections in x-z plane show that the envelope gas settles into a thin disc structure by t=14 yr, although it remains diffused in the outer regions and does not truncate sharply. Dense gas distribution and point particle orbit about their center of mass and move from the initial position at domain center (0, 0, 0) (see appendix A.2).

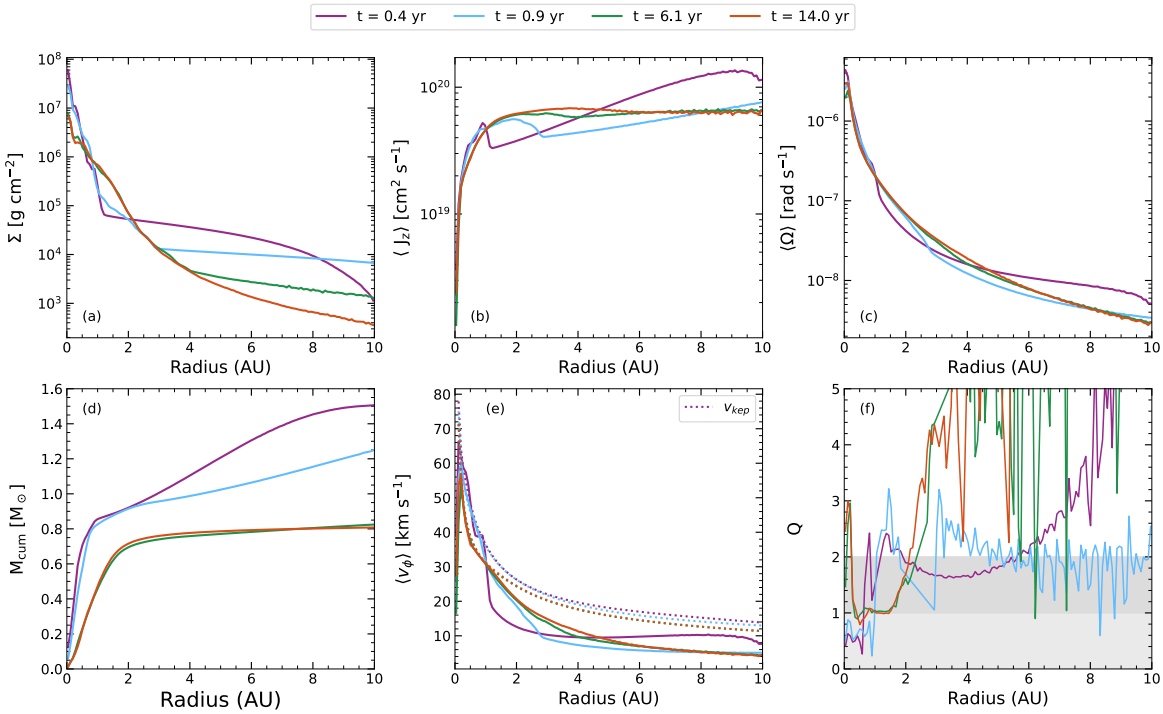


Figure 4.5: Time evolution of radial profiles of several physical quantities for $\eta 0.64$_iso simulation. From top left to bottom right: surface density (Σ), z-component of specific angular momentum (J_z), angular velocity (Ω), cumulative mass (M_{cum}), tangential (v_ϕ) and keplerian (v_{kep}) velocity and toomre parameter (Q).

Gas morphology changes from initially spherical to thin disc-like structure for the isothermal EoS and for the initial solid body rotation profile. Centrifugal force supports the gas parcels against gravity around the equatorial plane. Depending on the angular momentum distribution, gas parcels reorganize to orbit around the center of mass at their respective circularization radius and radial motion is slowed down. Due to isothermal EoS, material that piles up is able to release thermal energy and remain at a fixed global temperature. In addition, an ordered circularized motion is seen in the velocity vectors around the z-axis. In Fig. 4.6, cylindrically averaged radial profiles of tangential, radial and sound speed along with keplerian velocity are presented for $\eta 0.64$_iso run for snapshot t=14 yr. All the isothermal simulations are performed with constant sound speed of 5.985 km/s. It is found that there is negligible radial motion of gas. Within radius $\sim$ 1.2 AU the tangential velocity is similar to the keplerian velocity and for the outer regions tangential velocity drops by around 50% (sub-keplerian motion) by 5 AU.

Radial profiles for several kinematic properties for simulation $\eta 0.64$_iso are shown in Fig. 4.5. Temporal evolution of surface density profiles shows spreading of the dense material and the disc becomes diffused in the outer regions gradually, by t=14 yr. Surface density in central region is decreased from $\sim 6 \times 10^7\,\mathrm{g\,cm^{-2}}$ at t=0.4 yr to $\sim 8 \times 10^6\,\mathrm{g\,cm^{-2}}$ by t=14 yr. The cumulative mass converges to approximately 0.76 $M_\odot$ within the cylinder of radius 3 AU. Gas is found to be rotation supported, with tangential velocity being comparable to the keplerian velocity in the inner 1.2 AU region with the outer parts of the disc being sub-keplerian, with at least 50% rotation support. Panel (f) of Fig. 4.5 shows the Toomre parameter profiles ($Q = c_s\,\kappa/\pi\,G\,\Sigma$) at various times. Temporal persistence of Toomre parameter values in the

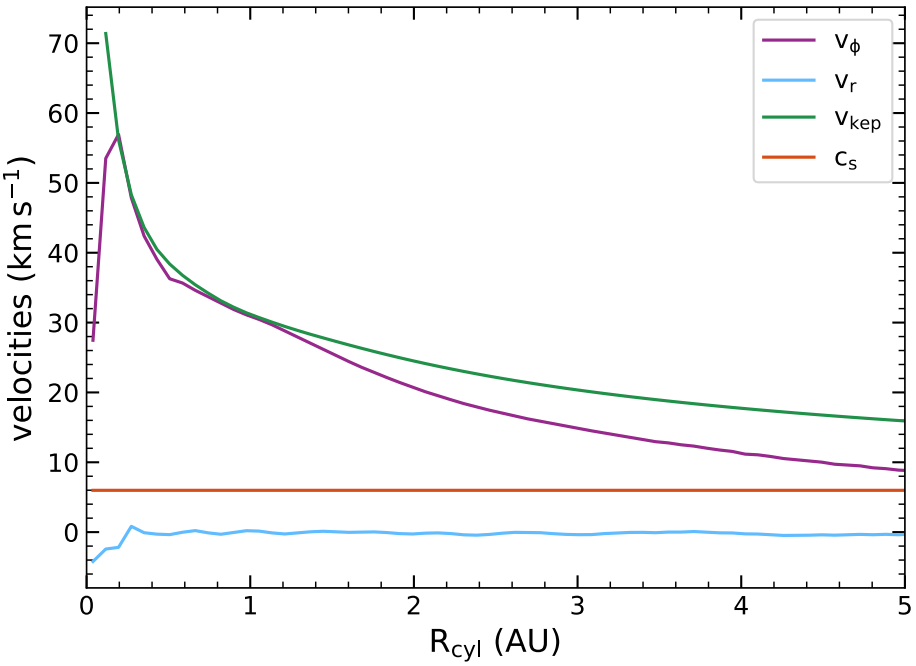


Figure 4.6: Radial profiles of tangential velocity (v_ϕ), radial velocity (v_r), keplerian (v_{kep}) and sound speed (c_s) with cylindrical radius for $\eta 0.64$_iso simulation at time t=14 yr.

range of $1 < Q < 2$ is found within radius of 2 AU from t=6 yr to t=14 yr.

Density-weighted projections of density for higher kinetic energy cases $\eta 1.6$_adia and $\eta 10$_adia are presented in Fig. 4.7 and 4.11 respectively. Gas morphology found in these simulations is similar to the lower kinetic energy case. A pressure-supported non-spherical gas remnant remains by the end of the simulations. Radial profiles for the post-ejection gas structures for these runs are shown in Fig. 4.8 and Fig. 4.12.

From radial profiles of simulation $\eta 1.6$_adia and $\eta 10$_adia, similar feature of spreading of the envelope gas with decrease in the density in inner regions is seen. Specific angular momentum in outer layers decreases as the material flows outwards for both the runs. Surface density profile shows a shallow decrease with radius in $\eta 10$_adia case (similar trend found for $\eta 1.6$_adia). For $\eta 10$_adia scenario, the angular velocity is reduced significantly by almost two orders of magnitude and develops an almost solid body rotation profile in the 3 AU region by t= 21 yr, with an average value of $\sim 1.92 \times 10^{-8}\,\mathrm{rad\,s^{-1}}$.

Figures 4.9 and 4.13 show the column density maps (in center of mass frame) for the higher kinetic energy cases with isothermal EoS. Structure of gas envelope changes from spherical in the beginning of simulation to thin-disc in both the cases as expected for Isothermal EoS. Spiral arm feature is seen in $\eta 1.6$_iso case at t=0.9 yr with ordered rotation in x-y plane. Similar to the $\eta 0.64$_iso case, system comprising of dense disc and the binary star point particle drifts in positive z-direction (see appendix A.2). Evenly distributed gas is found within 2.5 AU of radial extent in the case of $\eta 10$_iso (Fig. 4.13) by t=14 yr.

The radial profiles for $\eta 1.6$_iso and $\eta 10$_iso are illustrated in 4.10 and 4.14 respectively. The profiles correspond to same snapshots in figs. 4.9 and 4.13 respectively. Similar temporal behaviour of quantities is observed for these simulations as in the case of $\eta 0.64$_iso, but

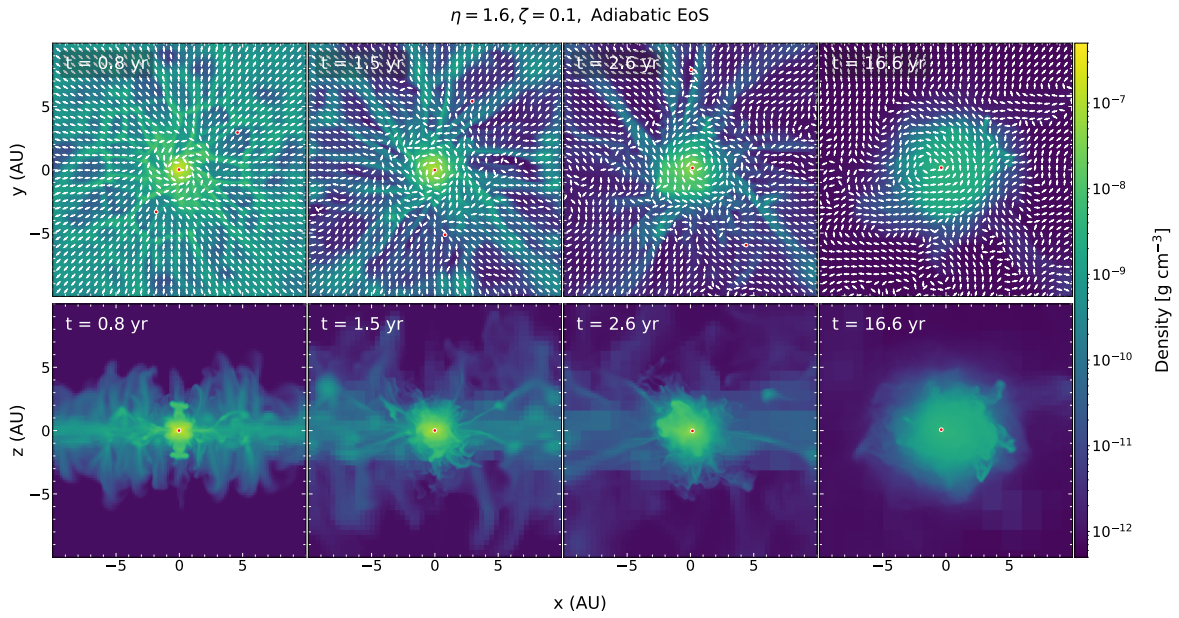


Figure 4.7: 2D maps of density-weighted density projections in x-y and x-z plane at different times for $\eta 1.6_\mathrm{adia}$, zoomed in on 20 AU of box in each direction)

with reduced cumulative mass and radial extent of the dense structure in the higher kinetic energy cases. A very small region of the disc (radius < 1 AU) shows $1 < Q < 2$ for $\eta 10_\mathrm{iso}$ case. Although the outer layers with high kinetic energy are ejected, the specific angular momentum and angular velocity in the gas structures do not show a decrease from the initial values. Results from all isothermal EoS simulations are presented till the time of 14 yr for comparison. Due to larger drift of the center of mass of the dense gas distribution and the binary point particle in case of $\eta 0.64_\mathrm{iso}$ and $\eta 1.6_\mathrm{iso}$ runs, the disc is resolved at the highest refinement level by that time since it is still confined in the highest resolved 5 AU region.

To estimate the power law indices for surface density and angular velocity profiles for all the isothermal runs in this work, following criteria is used for selecting the gas disk. Gas cells with density $\geq 6 \times 10^{-12}\,\mathrm{g\,cm^{-3}}$ are selected within a radius of 10 AU from the center of mass. The cylindrically averaged radial profiles are calculated for radial, vertical and tangential velocity, angular velocity and surface density. The radial range for power-law index is selected such that the tangential velocity is greater than both the radial and vertical velocity by a factor of two (Joos et al. [2012]). Along with this, the inner radius is fixed to 0.5 and an outer radius for each simulation. The outer radius is defined as the point where the surface density reduces by more than a factor of 4 over one bin. Visually it is the radius where the surface density drops to lower order of magnitude values (see appendix B.2). The same radial range is used for the angular velocity profile as well. Table 4.2 summarizes the cumulative mass and power law scalings for angular velocity and the surface density profiles, for the last snapshot of the isothermal runs.

Comparison with previous works:
From the simulations performed in this work, post-ejection density distribution is confined to around 10 AU in radius (upper bound) for adiabatic EoS (for $\sim 15 - 20$ yrs of evolution depending on the simulation) and within 7 AU (depending on simulation) for isothermal EoS (in ~ 14 yrs). As these are the early phases, gas distribution might spread further upon evolution. In all isothermal simulations, certain radial bins of disc are found to have $Q < 2$

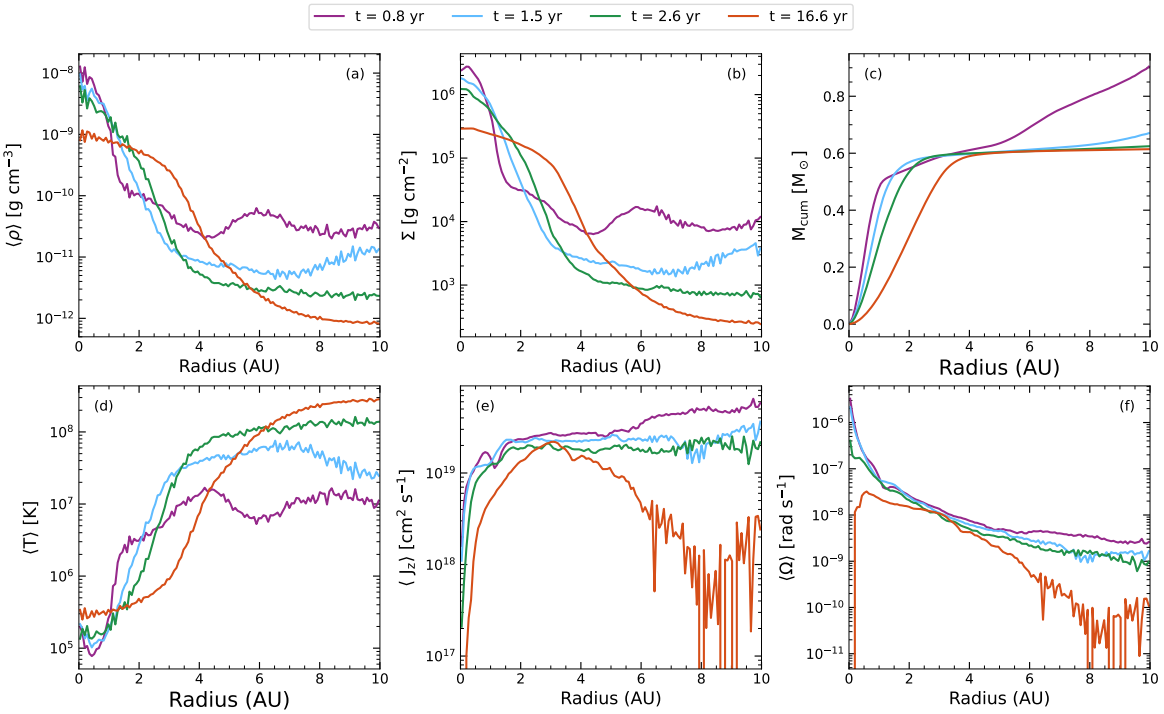


Figure 4.8: For η1.6_adia, time evolution of radial profiles of dynamical quantities for same snapshots as those displayed in the density weighted projections in Fig. 4.7.

Run	η KE/PE	M_{cum} $M_\odot$	n_Ω	n_Σ
η0.64_iso	0.64	0.80	-1.75 ± 0.014	-3.90 ± 0.11
η1.6_iso	1.6	0.64	-1.81 ± 0.014	-4.02 ± 0.08
η10_iso	10	0.18	-1.98 ± 0.02	-6.24 ± 0.21

Table 4.2: Cumulative mass (M_{cum}) and power-law indices for surface density (n_Σ) and angular velocity (n_Ω) profiles of post-ejection gas structures, presented for isothermal simulations at t=14 yr. Mass of the binary star point particle is $M_{BS} = 0.646\,M_\odot$.

for region within 2 AU. At these distances, photo-heating from the central binary star may significantly heat inner parts of the disc and stabilize it against the fragmentation. Schleicher and Dreizler [2014] find that radiative feedback is significant out to the scales of 4 AU when atmospheric temperature of star is $\sim 10^5$ K and around 1 AU for temperature of $\sim 10^4$ K.

Schleicher and Dreizler [2014] provided the estimates for planetary masses for NN Ser system. For their fiducial model of surface density power law index n=1, initial clump masses resulting in NN Ser like planets are found at gas temperatures of 370 K and 231 K at distance of 5.4 AU and 3.4 AU respectively. They found that steeper slope in surface density supports formation of more massive clumps in the inner parts of the disc, even at higher temperatures. Power law indices for surface density profiles of the three isothermal simulations in this work are higher than the range (n $\in$ [0, 1.5]) studied in Schleicher and Dreizler [2014]. η10_iso simulation has final cumulative mass comparable to the bound mass assumed in Schleicher and Dreizler [2014]. From the column density plots (Fig. 4.13), even gas distribution is found and only the inner region (radius $<$ 1 AU) of the disc shows Q $<$ 2. To conclude

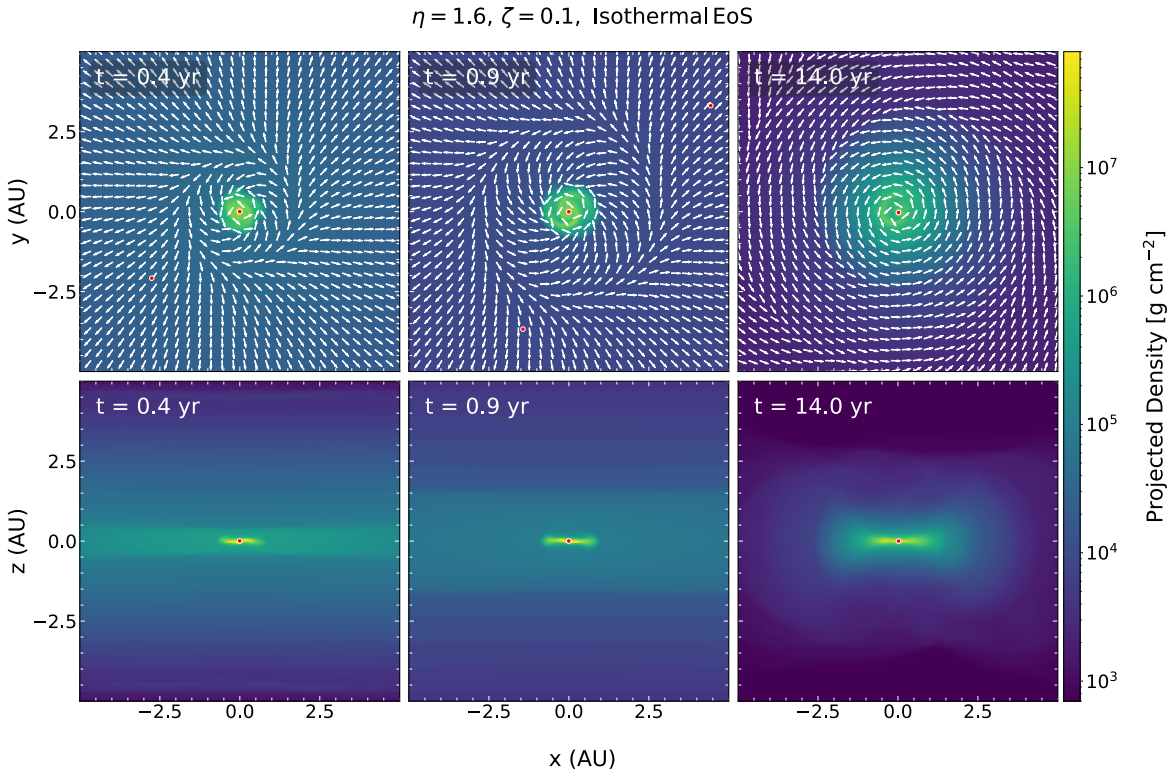


Figure 4.9: Projected density maps in both x-y and x-z plane for $\eta 1.6$_iso run (in center of mass frame), showing $10\,\mathrm{AU}^3$ region. Spiral arm feature is present close to the point particle at time t=0.9 yr.

whether clumps can form upon fragmentation in this work, higher resolution in simulations is required (Lichtenberg and Schleicher [2015]) with realistic cooling and heating processes.

Limitations of present work:
Simulations in this study have been performed for two extreme cases of no cooling and instantaneous cooling using ideal gas EoS whereas a realistic investigation of disk formation and evolution in post common envelope event would require inclusion of cooling processes such as dust cooling, radiative cooling or full radiative transport.

Upon increasing the size of computational domain to follow the ejecta, ambient medium of the box effectively increases gas mass on the grid due to the large volume it encompasses. Although it is shown in the appendix B.1 through dynamical quantities that the ambient medium is moving outwards, adding passive tracer particles to common envelope gas will help to clearly distinguish the envelope gas from the ambient medium. In simulations with adiabatic EoS, the ambient medium (fluff) is hotter than the envelope gas so that the gas sphere does not expand and is in initially stable configuration on the grid. This ambient material could effect the ejecta thermodynamically.

Temperature profiles of the bound remnant and the fall back material are crucial for the type of disc that can form. In adiabatic runs, temperatures are of the order of 10^5 K for the gas distribution but for planet formation to occur, gas should cool down to the temperatures of the order of a few hundred Kelvin. Therefore, from purely adiabatic runs with no cooling processes and surrounding hot ambient medium, one cannot obtain accurate temperature measurements. Globally isothermal simulations performed in this work are idealistic de-

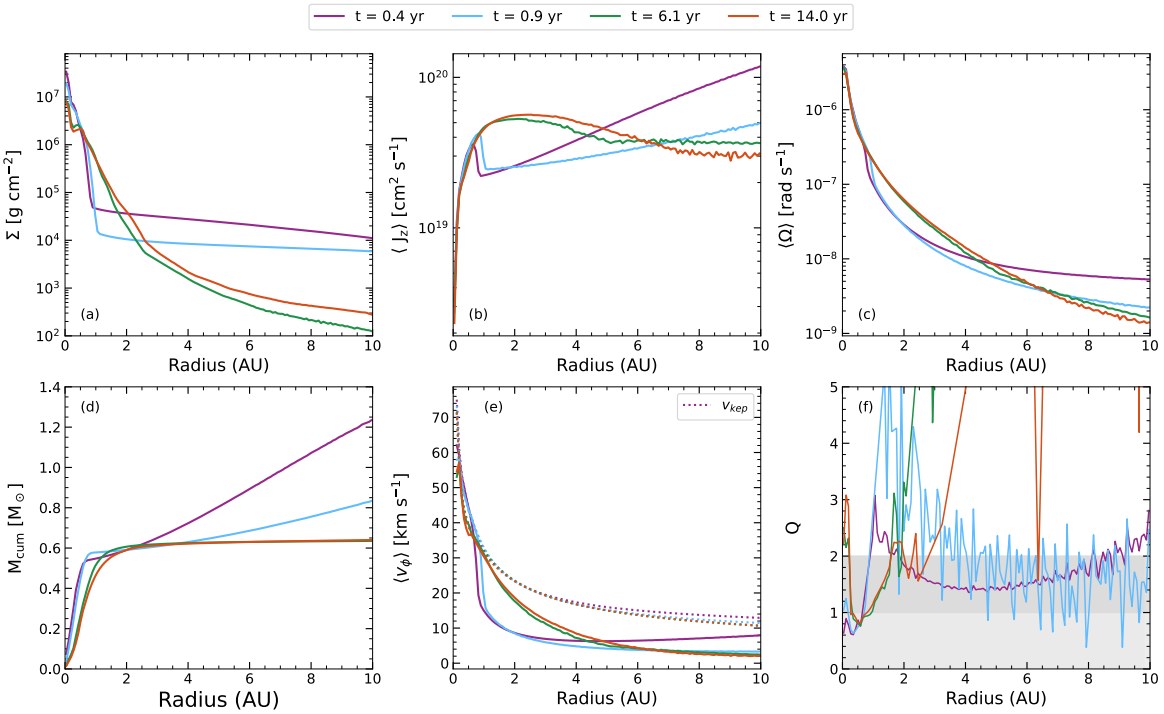


Figure 4.10: Similar to Fig. 4.5), radial profiles for surface density, cumulative mass, z-component of specific angular momentum, keplerian and tangential velocities, angular velocity and toomre parameter are presented for $\eta 1.6$_iso case.

scription for cooling layers of the partially ionized stellar material in common envelope gas. With globally isothermal conditions, one cannot obtain the accurate variation of temperature with radius. Additionally, the circumbinary material might be actively removed through recombination driven winds over time as the material cools (Vetter et al. [2024]). Therefore, addition of recombination effects is an important process to include.

This work does not include dust formation and its evolution which has been found to initiate during the inspiral phase itself (Bermúdez-Bustamante et al. [2024], Iaconi et al. [2020]). Since the binary star has been assumed to be a single point particle in this work, lifting this assumption to include the actual two cores and the effects of their orbital motion is left for future study. Investigation with higher resolution is required to model post-CE disc evolution and the gravitational instabilities along with investigating hydrostatic equilibrium in the vertical direction.

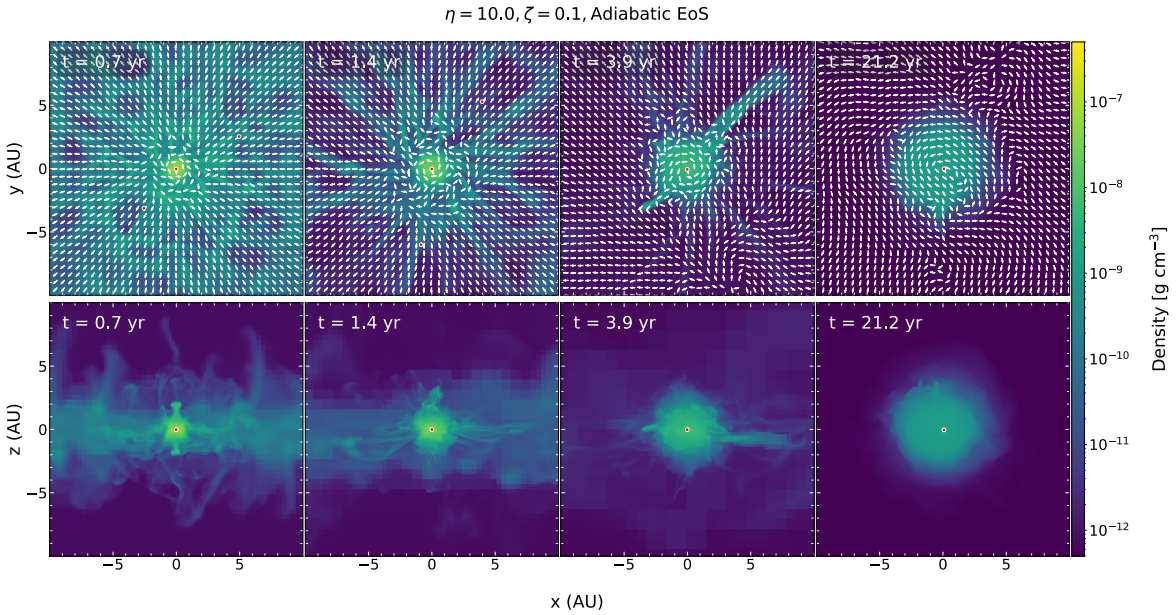


Figure 4.11: Density-weighted density projection plots in x-y and x-z plane for different timestamps for simulation η10_adia, zoomed-in on 20 AU^3 region.

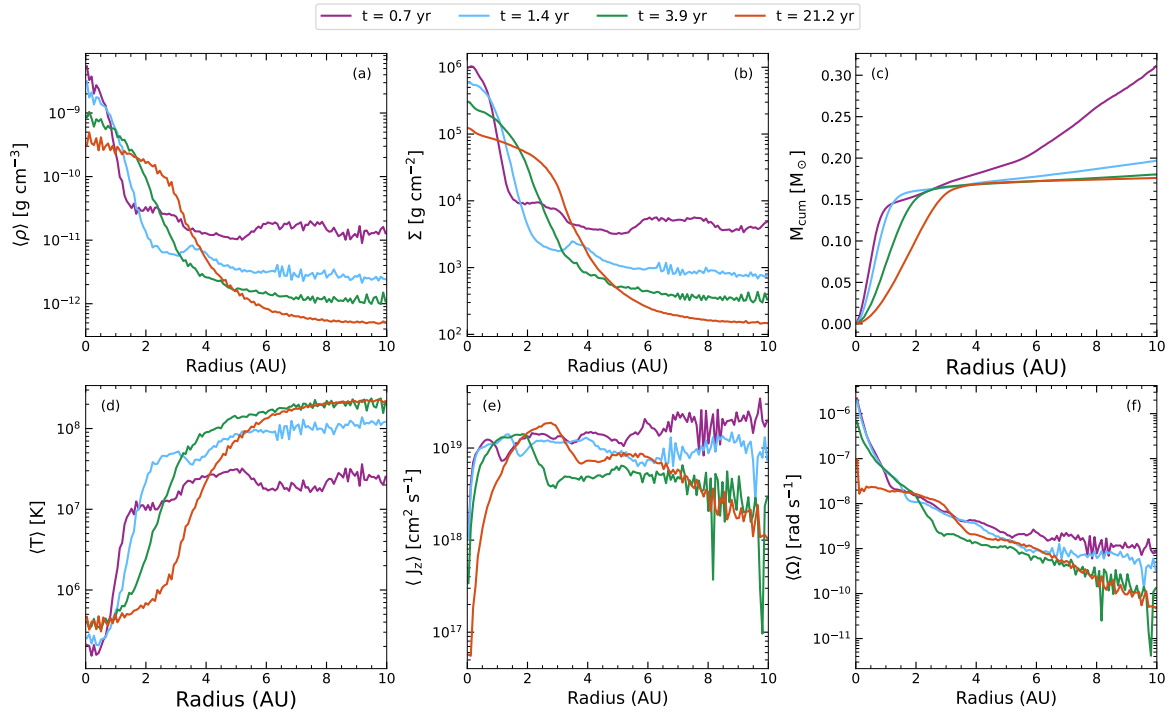


Figure 4.12: Similar to Fig. 4.2, cylindrically averaged radial profiles of volume density, surface density, cumulative mass, temperature, z-component of specific angular momentum and angular velocity is presented for several snapshots, for η10_adia run.

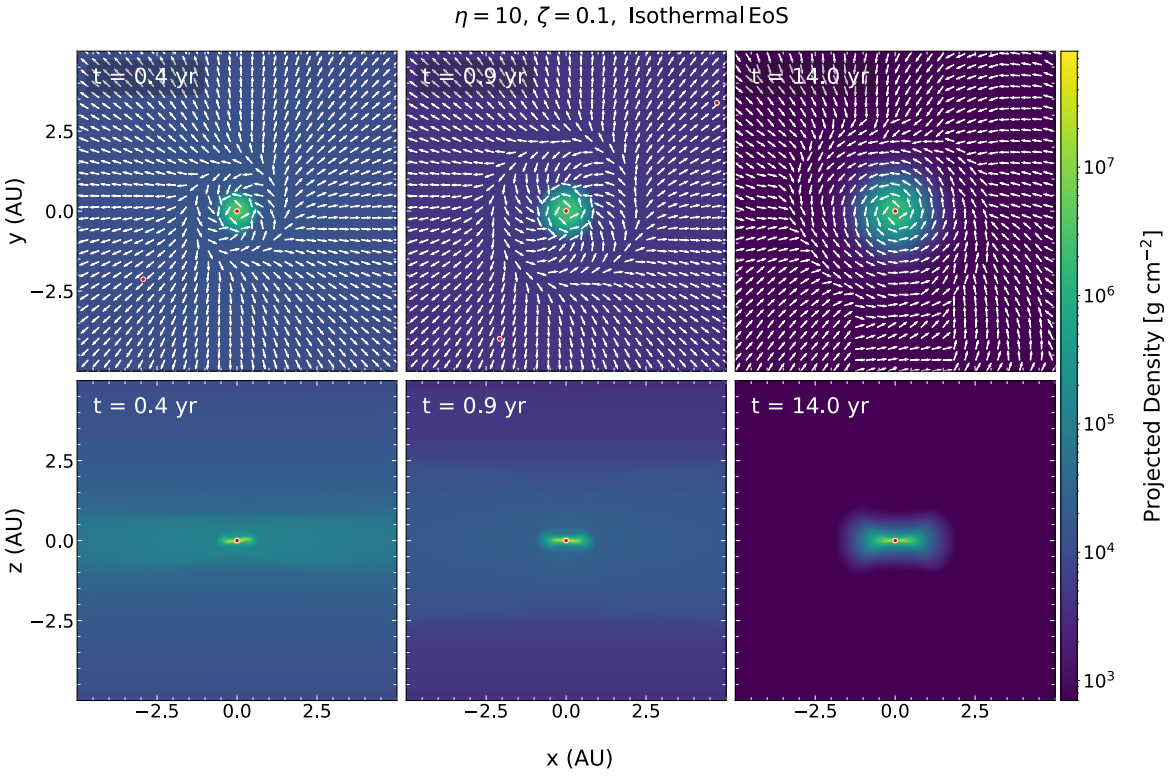


Figure 4.13: Similar to Fig. 4.4 for η10_iso run with isothermal EoS.

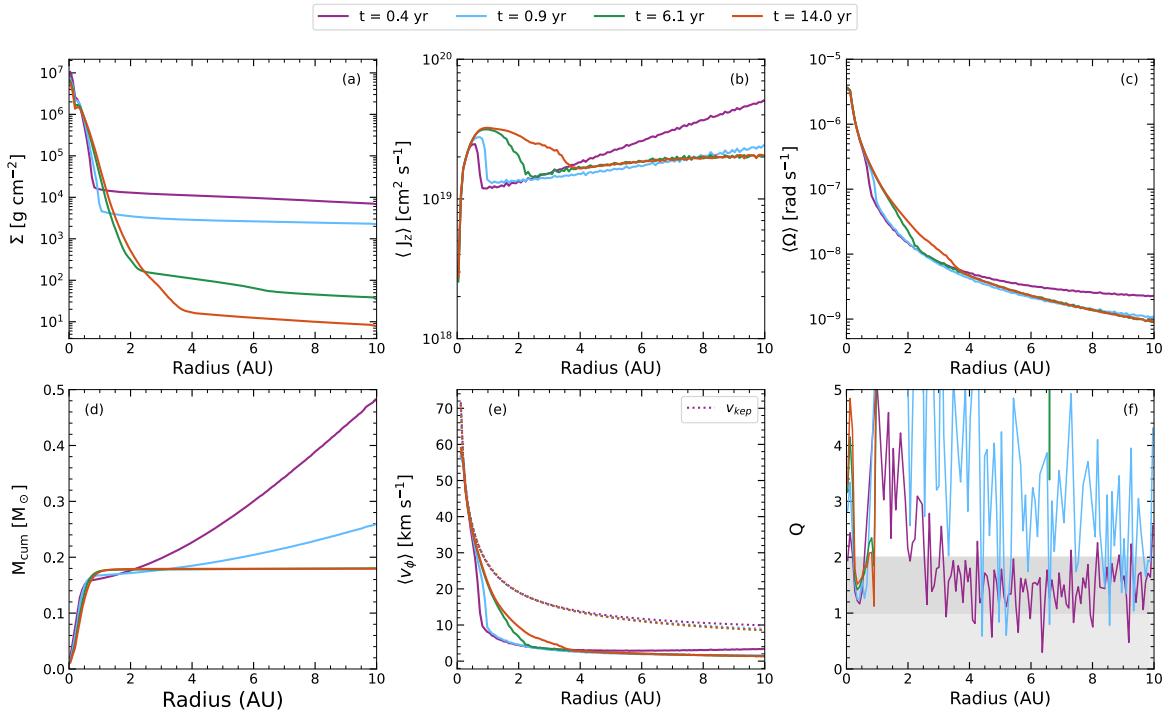


Figure 4.14: Radial profiles of surface density, z-component of specific angular momentum, angular velocity, cumulative mass, tangential velocity along with keplerian velocity and Toomre parameter for several timestamps. Similar to Fig. 4.5 for η10_iso simulation.

4.4 Summary and Conclusions

3D hydrodynamic simulations of CE ejection are performed to investigate kinematic properties of gas structures, for varying kinetic energy of gas ($\eta = \mathrm{KE/PE}$) leading to different amounts of remnant mass. For each dimensionless parameter value (η), two thermodynamic extremes are studied using adiabatic (no cooling) and isothermal (instantaneous cooling) EoS.

Independent of the $\eta = \mathrm{KE/PE}$ parameter, vertically extended non-spherical gas distribution is obtained in all the adiabatic simulations. The radial profiles of rotation curves show that the leftover structure is pressure supported and sub keplerian. The density distribution is constrained to 10 AU in radius for the time simulated in this work ($\sim 15 - 20$ yrs).

In case of isothermal EoS, once again independent of the $\eta = \mathrm{KE/PE}$ parameter, thin-disk structure is found with diffused distribution and not a sharp drop in density. Gas distribution is rotation supported with tangential velocity following keplerian profile in the inner regions and at least 50% in the outer regions of dense gas distribution. Discs in all the isothermal simulations are compact and lie within 7 AU for the simulated time of ~ 14 yrs. For $\eta 0.64_\mathrm{iso}$ and $\eta 1.6_\mathrm{iso}$ case, disc is found to have with $\mathrm{Q} \sim 1$ in the inner regions due to the steep surface density profile for high temperatures of 4300 K. For $\eta 10_\mathrm{iso}$ run with remnant mass of 0.18 $\mathrm{M}_\odot$, a small radial extent of 1 AU has $1 < \mathrm{Q} < 2$. Gas distributions in both adiabatic and isothermal cases may spread upon further evolution and extend to further distances.

Feasibility of second generation planet formation through gravitational instability depends on the surface density profile, rotation budget and the temperature profile of the post-CE structures. While the isothermal simulations show that the inner regions of the disc could be gravitationally unstable, it is important to note that inner regions of disc (a few AU) may be subject to heating from the stellar cores (Schleicher and Dreizler [2014]) making it stable against fragmentation. In addition, simulations with higher resolution are needed to produce pronounced spiral features and clump formation.

Chapter 5

Conclusions and Outlook

Multiple confirmed detections of circumbinary planets have been made around main-sequence binaries (Thebault and Bonanni [2025]), whereas their existence in tight and evolved binary systems still remains debatable. Through indirect observations of Eclipse timing variations, planets have been proposed to exist around close white dwarf - main sequence binaries. Such planetary configurations raise questions about their existence and survival during the violent mass transfer phase of common envelope evolution.

Two possible scenarios have been studied in detail over the past few years. First, the circumbinary planets formed along with the main sequence binary and survived the common envelope stage of the binary star evolution. Orbital evolution of such planets as the host binary evolves and ejects envelope gas, has been studied using analytical estimates and N-body simulations. Some works assumed isotropic mass loss along with negligible interactions between gas and the planets (Veras and Tout [2012], Kostov et al. [2016]) during adiabatic and non-adiabatic mass loss scenarios. Völschow et al. [2014] obtained semi-analytical estimates on final (post-CE) orbital parameters for isotropic case along with investigating the effects of disk-shaped ejection. They estimated the geometric gas drag force on the planets but found it to be insignificant compared to the gravitational force of the central mass. While these studies found that the planets move to wider and eccentric orbits as the central binary ejects mass during the CE phase, they did not include the effects of extended asymmetric envelope with the intermediate mass loss scenarios.

After the dynamical plunge-in stage of the CE event, leftover material bound to the binary cores with substantial angular momentum, may settle into a disk-like configuration (Kashi and Soker [2011]). These circumbinary disks could serve as an environment to form second generation planets (Perets [2010]), provided the disk has cooled down substantially and has sufficient mass and angular momentum to support formation of gas giant planets. Schleicher and Dreizler [2014] showed through analytical estimates that such planets can form out of the post-CE material through gravitational instability at separations of a few AU, assuming certain properties of the post-CE material.

Numerical works on CE evolution have not yet settled on the properties of the bound remnant material (Röpke and De Marco [2023], Ivanova et al. [2013]), in terms of the retained mass and angular momentum budget. While some simulations have shown to eject almost the entire envelope in the span of a few tens of years using the release of recombination energy (Vetter et al. [2024]), these studies have not included radiation transport or cooling processes which can retain more mass.

This thesis focuses on the orbital dynamics of first generation planets during the common envelope event and on studying the properties of post ejection circumbinary gas distribution which could be the nurseries for second generation planet formation. Both these goals are addressed using 3D hydrodynamic simulations performed with FLASH code. First, the effects

of mass loss during common envelope event on the orbital evolution of pre-existing planets are studied. In agreement to the semi-analytical results (Veras and Tout [2012], Völschow et al. [2014]), first generation planets initialized on coplanar circular orbits are unbound for enclosed mass fraction $\leq 50\%$, in case of instantaneous mass loss models. This shows that even in the case of planets interacting with the extended asymmetric envelope, orbital parameters obtained are similar to those from analytical approximation for instantaneous cases. Planets are found to move to wider and eccentric orbits in case of instantaneous and intermediate mass ejection scenarios. No clear analytical function could be obtained to relate initial and final orbital properties with the dynamic mass ratio for intermediate scenarios. First generation planets may survive in these cases.

Second, the properties of leftover material post CE event are studied, to determine whether they could serve as the environment for second generation planet formation. 3D hydrodynamic simulations with two thermodynamic extremes of no cooling (adiabatic equation of state) and efficient cooling (isothermal) are performed. While adiabatic simulations result in vertically extended sub keplerian pressure-supported structures, the runs with isothermal equation of state lead to flattened disk morphology which is rotation supported. This gas distribution is confined to around 7 AU of radial extent for the time simulated in this work. Gas distribution obtained from both the thermodynamic scenarios may spread upon further evolution. Circumbinary material in adiabatic simulation can cool down as it expands. Disks in isothermal simulations show steep surface density profiles with more mass concentrated in the inner regions of the disc. Isothermal simulations have fixed global temperature of 4300 K. For these discs, spiral arm features are observed and toomre parameter ranges around unity for the inner regions indicating that these discs could be gravitationally unstable. In order to study further disc evolution, high resolution simulations are required to show pronounced features. While the ideal scenario of efficient cooling indicates that second generation planet formation via gravitational instability might be a possible channel, additional physical processes such as photo heating from the central binary and relevant cooling processes need to be modeled.

Outlook:
While the first step of globally isothermal simulations show spiral arm structures, this work can be expanded by adding different cooling and heating processes such as dust cooling, photo heating and radiative cooling from the optically thin regions. Initializing these mass ejection simulations from the final output of a common envelope evolution simulation would result in a more consistent evolution along with the binary cores orbiting in the center. Addition of tracer particles to the envelope gas could be the next step to clearly indicate the remnant envelope gas distribution.

For the first generation planet dynamics, it could be useful to study the intermediate mass loss scenario with more than 75% mass loss from the system in order to identify if the planets remain bound in the case of high mass loss. To achieve this, planets could be initialized on reduced orbital separations than used in this work. In order to run these simulations longer with high resolution, better refinement criterion can be implemented.

Appendix A

Choice of frame of reference

A.1 For orbital properties of planets

To decide the origin for obtaining orbital properties of planets, different frames are considered. These are center of mass of contents of entire box: ambient medium, envelope gas and the point particles; another possible reference frame is that of the binary star point particle and the third is the domain center (0, 0, 0). Domain center is the only inertial frame but it is not a physical point of reference. While center of mass of full simulation box drifts, the binary star particle orbits around this center of mass making both these frames as non-inertial (Fig. A.1).

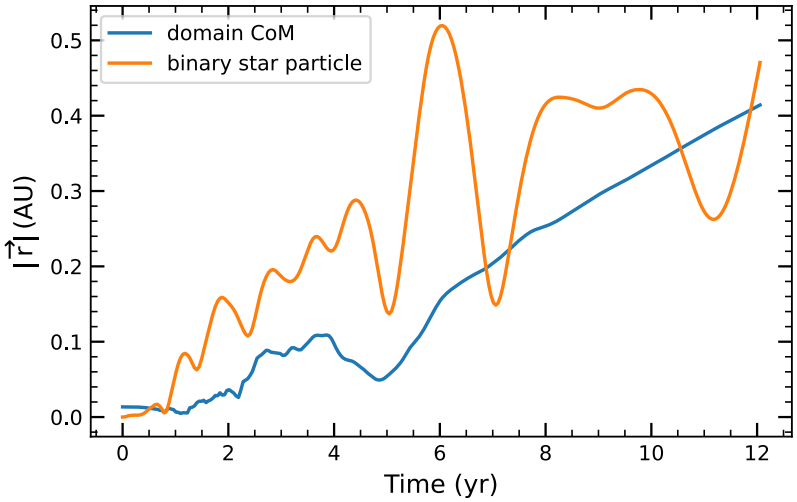


Figure A.1: Time evolution of orbital separation of binary star particle and center of mass of full box from the domain center (0, 0, 0) for simulation I2.

Ideally, the center of mass of the full computational domain should not have acceleration. Due to diode boundary conditions, ejecta spread asymmetrically in the box is allowed to leave the boundary. Linear momentum conservation of material on the grid is affected due to mass leaving the boundary asymmetrically, resulting in drift of center of mass. In Fig. A.2, radial distance of center of mass with time is shown for all the eight simulations. The movement of center of mass is larger for high kinetic energy cases where more mass is ejected from the system. In order to see how the choice of origin affects eccentricity, results using all the three reference frames are illustrated in Fig. A.3.

To conserve linear momentum for contents on the grid, binary star point particle can be imparted velocities accordingly. For calculation of all the orbital properties shown in this work, center of mass of entire box is utilized as the frame of reference for each simulation.

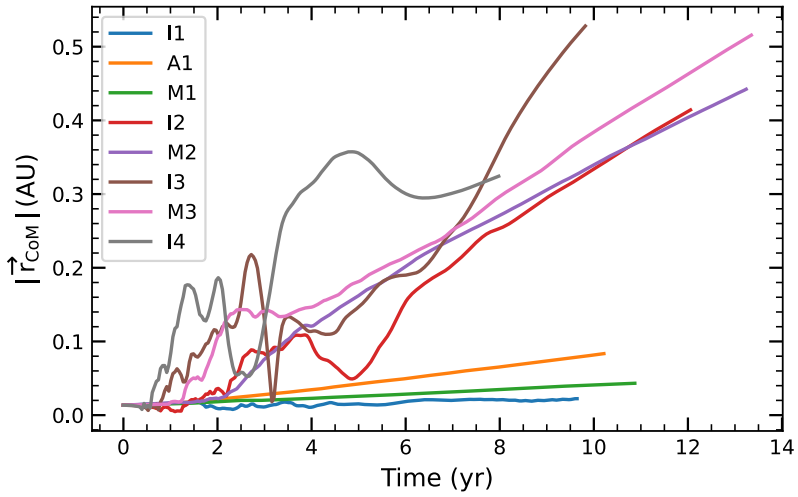


Figure A.2: Drift in center of mass (from domain center (0, 0, 0)) obtained from the contents of entire simulation domain with time, presented for I, M and A models.

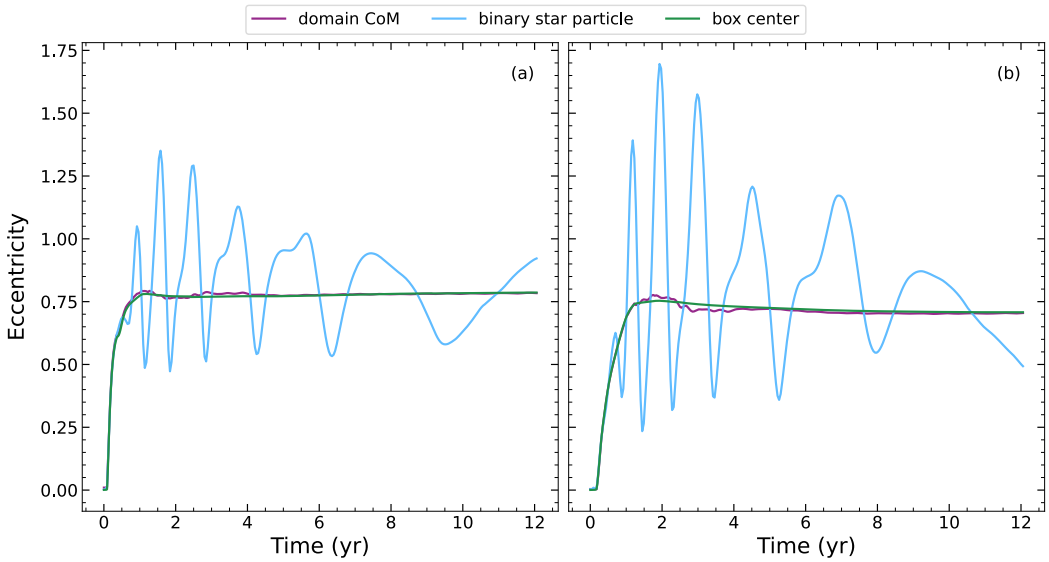


Figure A.3: Evolution of eccentricity of the two planets with time using three points of reference, presented for model I2. Panel (a) shows results for inner planet (P1) and panel (b) for outer planet (P2).

A.2 For properties of post-CE structures

Due to the presence of ambient medium (with substantial mass) in the computational domain of increased size and de-refined blocks in outer parts of the box, center of mass is calculated using all the gas cells with $\rho \geq 6 \times 10^{-12}\,\mathrm{g\,cm^{-3}}$ inside a 10 AU sphere, with the sphere centered on binary star point particle. Figs. A.4 and A.5 show the movement of center of mass of selected mass distribution for respective simulations.

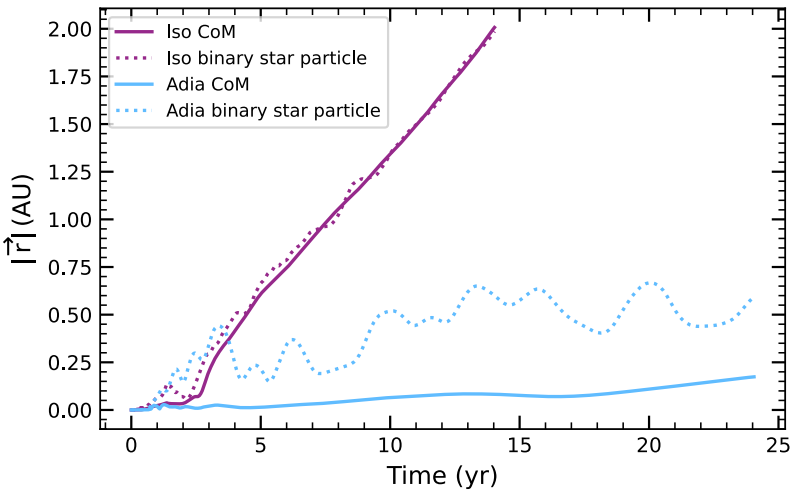


Figure A.4: Comparison of drift in center of mass and binary star point particle from the domain center (0, 0, 0), presented for simulations $\eta 0.64_\mathrm{adia}$ and $\eta 0.64_\mathrm{iso}$.

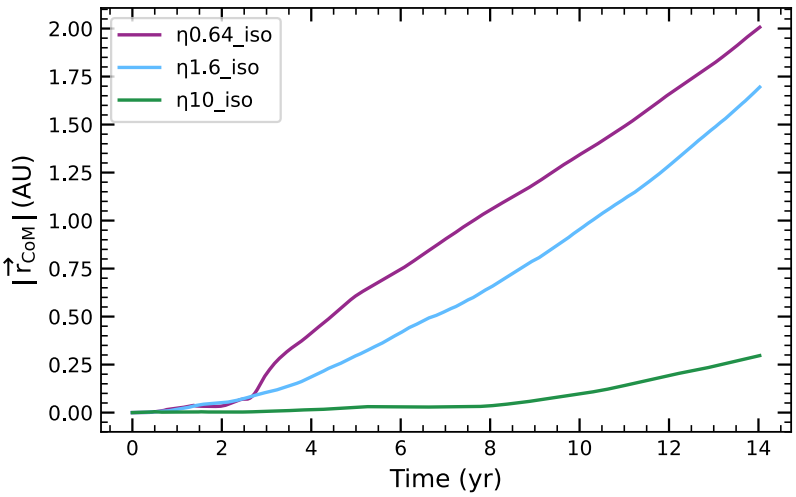


Figure A.5: Evolution of position of center of mass with respect to the domain center (0, 0, 0) is shown for the three isothermal simulations.

Figure A.6 shows the rotation curves for gas distribution with respect to three points of reference. Profiles with respect to point particle and the center of mass are similar and are significantly different from those with respect to the box center in the inner 5 AU radial range. All the curves for respective quantities converge for outer radii.

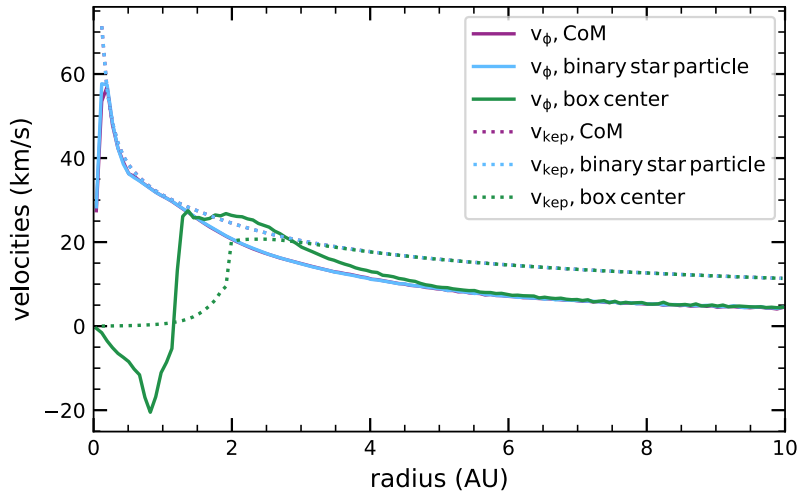


Figure A.6: Mass-weighted average of tangential velocity over cylindrical shells and keplerian velocity with respect to three different reference frames presented for simulation $\eta 0.64_\mathrm{iso}$ at time t=14 yr.

Appendix B

Circumbinary discs

B.1 Hot ambient medium

Figure B.1 shows the radial profiles for density and radial velocity with time for the entire simulation box for run $\eta 1.6_\mathrm{adia}$. In the density profiles, it is seen that the material spreads outwards with high density peaks moving to larger radii with time. At the onset of simulations, ambient medium is initialized with zero velocity. As the dense common envelope material expands and moves outwards, the hot vacuum is pushed out and leaves the domain. The hot low-density ambient medium does not seem to affect the dynamics of the central dense gas.

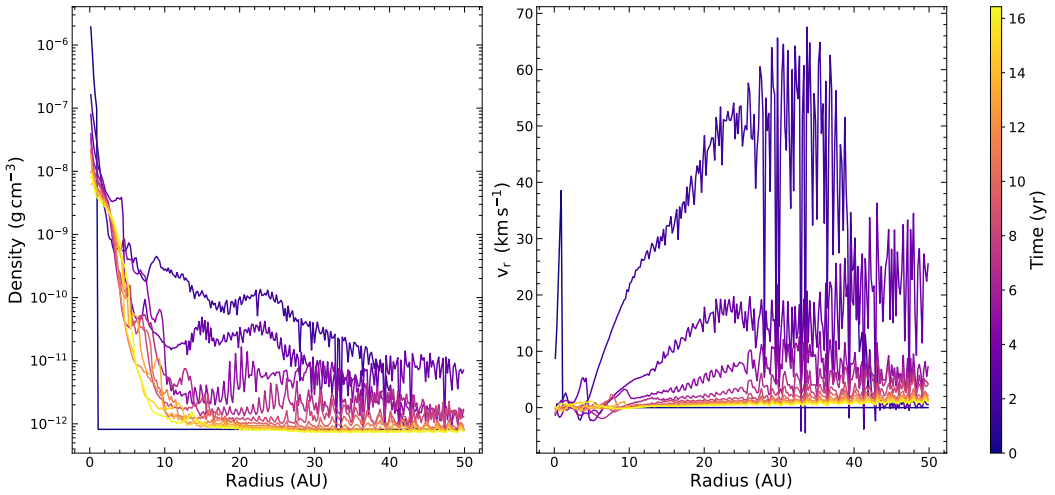


Figure B.1: Time evolution of spherically averaged radial profiles of gas density and radial velocity for the entire computational domain, for run $\eta 1.6_\mathrm{adia}$.

B.2 Power law indices

Figure B.2 shows the cylindrically averaged radial profiles of angular velocity and surface density for the three isothermal simulations, produced using the gas cells with density $\rho \geq 6 \times 10^{-12}\,\mathrm{g\,cm^{-3}}$ within a radius of 10 AU from the center of mass, for time time t=14 yr. Power-law indices presented in the table 4.2 are calculated for a particular radial range. This radial range is decided by both the ratios of tangential velocity to radial velocity and to vertical velocity, to be greater than two (Joos et al. [2012]). In addition to this, radial range is set from 0.5 to an outer radius, where outer radius is defined by the point where the surface density drops by a factor of four, for each simulation. This visually corresponds to the radius where the surface density shows clear drop to lower order of magnitudes for each simulation.

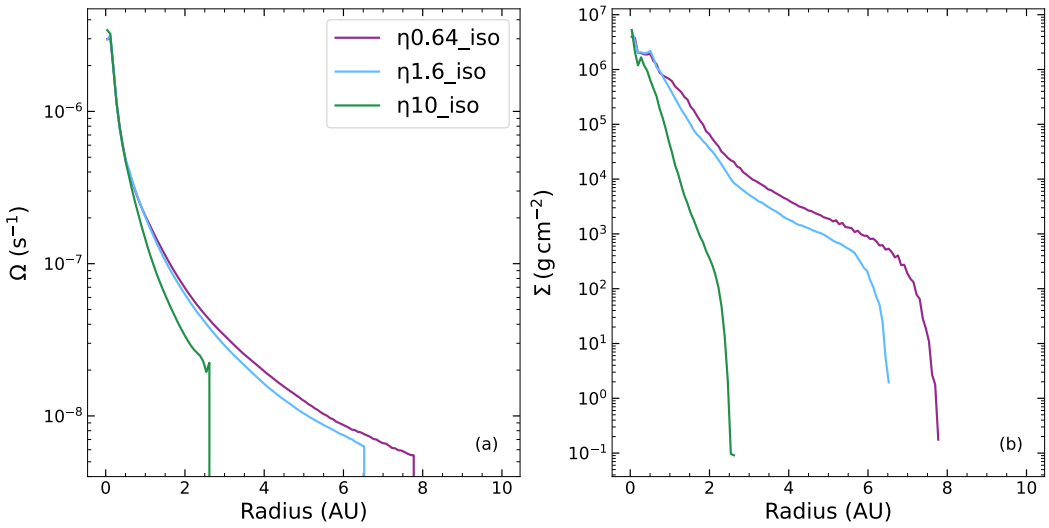


Figure B.2: Radial profiles for angular velocity (Ω) and surface density (Σ) used for obtaining the power law indices (see table 4.2), for the three isothermal simulations at time t=14 yr.

Bibliography

Fred C. Adams, Kassandra R. Anderson, and Anthony M. Bloch. Evolution of planetary systems with time-dependent stellar mass-loss. *Monthly Notices of the Royal Astronomical Society*, 432(1):438–454, June 2013. doi: 10.1093/mnras/stt479.

Kateryna Andrych, Devika Kamath, Jacques Kluska, Hans Van Winckel, Steve Ertel, and Akke Corporaal. Second-generation protoplanetary discs around evolved binaries: a high-resolution polarimetric view with SPHERE/IRDIS. *Monthly Notices of the Royal Astronomical Society*, 524(3):4168–4195, September 2023. doi: 10.1093/mnras/stad1968.

James H. Applegate. A Mechanism for Orbital Period Modulation in Close Binaries. *Astrophysical Journal*, 385:621, February 1992. doi: 10.1086/170967.

Thomas A. Baycroft, Amaury H. M. J. Triaud, and Pierre Kervella. New evidence about HW Vir's circumbinary planets from Hipparcos-Gaia astrometry and a reanalysis of the eclipse timing variations using nested sampling. *Monthly Notices of the Royal Astronomical Society*, 526(2):2241–2250, December 2023. doi: 10.1093/mnras/stad2794.

Ealeal Bear and Noam Soker. First- versus second-generation planet formation in post-common envelope binary (PCEB) planetary systems. *Monthly Notices of the Royal Astronomical Society*, 444(2):1698–1704, October 2014. doi: 10.1093/mnras/stu1529.

Luis C. Bermúdez-Bustamante, Orsola De Marco, Lionel Siess, Daniel J. Price, Miguel González-Bolívar, Mike Y. M. Lau, Chunliang Mu, Ryosuke Hirai, Taïssa Danilovich, and Mansi M. Kasliwal. Dust formation in common envelope binary interactions - II: 3D simulations with self-consistent dust formation. *Monthly Notices of the Royal Astronomical Society*, 533(1):464–481, September 2024. doi: 10.1093/mnras/stae1841.

K. Beuermann, F. V. Hessman, S. Dreizler, T. R. Marsh, S. G. Parsons, D. E. Winget, G. F. Miller, M. R. Schreiber, W. Kley, V. S. Dhillon, S. P. Littlefair, C. M. Copperwheat, and J. J. Hermes. Two planets orbiting the recently formed post-common envelope binary NN Serpentis. *Astronomy & Astrophysics*, 521:L60, October 2010. doi: 10.1051/0004-6361/201015472.

K. Beuermann, S. Dreizler, and F. V. Hessman. The quest for companions to post-common envelope binaries. IV. The 2:1 mean-motion resonance of the planets orbiting NN Serpentis. *Astronomy & Astrophysics*, 555:A133, July 2013. doi: 10.1051/0004-6361/201220510.

P. Bodenheimer and R. E. Taam. Double-core evolution. II - Two-dimensional hydrodynamic effects. *Astrophysical Journal*, 280:771–779, May 1984. doi: 10.1086/162049.

C. S. Brinkworth, T. R. Marsh, V. S. Dhillon, and C. Knigge. Detection of a period decrease in NN Ser with ULTRACAM: evidence for strong magnetic braking or an unseen companion. *Monthly Notices of the Royal Astronomical Society*, 365(1):287–295, January 2006. doi: 10.1111/j.1365-2966.2005.09718.x.

V. Bujarrabal, A. Castro-Carrizo, J. Alcolea, H. Van Winckel, C. Sánchez Contreras, and M. Santander-García. A second post-AGB nebula that contains gas in rotation and in expansion: ALMA maps of IW Carinae. *Astronomy & Astrophysics*, 597:L5, January 2017. doi: 10.1051/0004-6361/201629317.

Luke Chamandy, Yisheng Tu, Eric G. Blackman, Jonathan Carroll-Nellenback, Adam Frank, Baowei Liu, and Jason Nordhaus. Energy budget and core-envelope motion in common envelope evolution. *Monthly Notices of the Royal Astronomical Society*, 486(1):1070–1085, June 2019. doi: 10.1093/mnras/stz887.

Luke Chamandy, Eric G. Blackman, Adam Frank, Jonathan Carroll-Nellenback, and Yisheng Tu. Common envelope evolution on the asymptotic giant branch: unbinding within a decade? *Monthly Notices of the Royal Astronomical Society*, 495(4):4028–4039, July 2020. doi: 10.1093/mnras/staa1273.

Luke Chamandy, Jonathan Carroll-Nellenback, Eric G. Blackman, Adam Frank, Yisheng Tu, Baowei Liu, Yangyuxin Zou, and Jason Nordhaus. How negative feedback and the ambient environment limit the influence of recombination in common envelope evolution. *Monthly Notices of the Royal Astronomical Society*, 528(1):234–254, February 2024. doi: 10.1093/mnras/stae036.

A. Corporaal, J. Kluska, H. Van Winckel, K. Andrych, N. Cuello, D. Kamath, and A. Mérand. Transition disc nature of post-AGB binary systems confirmed by mid-infrared interferometry. *Astronomy & Astrophysics*, 674:A151, June 2023a. doi: 10.1051/0004-6361/202346408.

A. Corporaal, J. Kluska, H. Van Winckel, D. Kamath, and M. Min. What does a typical full disc around a post-AGB binary look like?. Radiative transfer models reproducing PIONIER, GRAVITY, and MATISSE data. *Astronomy & Astrophysics*, 671:A15, March 2023b. doi: 10.1051/0004-6361/202245689.

M. de Kool. Common Envelope Evolution and Double Cores of Planetary Nebulae. *Astrophysical Journal*, 358:189, July 1990. doi: 10.1086/168974.

J. D. M. Dewi and T. M. Tauris. On the energy equation and efficiency parameter of the common envelope evolution. *Astronomy & Astrophysics*, 360:1043–1051, August 2000. doi: 10.48550/arXiv.astro-ph/0007034.

A. Dubey, L. B. Reid, and R. Fisher. Introduction to FLASH 3.0, with application to supersonic turbulence. *Physica Scripta Volume T*, 132:014046, December 2008. doi: 10.1088/0031-8949/2008/T132/014046.

Peter Eggleton. *Evolutionary Processes in Binary and Multiple Stars*. 2011.

B. Fryxell, K. Olson, P. Ricker, F. X. Timmes, M. Zingale, D. Q. Lamb, P. MacNeice, R. Rosner, J. W. Truran, and H. Tufo. FLASH: An Adaptive Mesh Hydrodynamics Code for Modeling Astrophysical Thermonuclear Flashes. *Astrophysical Journal Supplement Series*, 131(1):273–334, November 2000. doi: 10.1086/317361.

Ma. T. García-Díaz, D. M. Clark, J. A. López, W. Steffen, and M. G. Richer. The Outflows and Three-Dimensional Structure of NGC 6337: A Planetary Nebula with a Close Binary Nucleus. *Astrophysical Journal*, 699(2):1633–1638, July 2009. doi: 10.1088/0004-637X/699/2/1633.

Guillermo García-Segura, Ronald E. Taam, and Paul M. Ricker. Common Envelope Shaping of Planetary Nebulae. III. The Launching of Jets in Proto-Planetary Nebulae. *Astrophysical Journal*, 914(2):111, June 2021. doi: 10.3847/1538-4357/abfc4e.

Hila Glanz and Hagai B. Perets. Efficient common-envelope ejection through dust-driven winds. *Monthly Notices of the Royal Astronomical Society*, 478(1):L12–L17, July 2018. doi: 10.1093/mnrasl/sly065.

Aldana Grichener, Efrat Sabach, and Noam Soker. The limited role of recombination energy in common envelope removal. *Monthly Notices of the Royal Astronomical Society*, 478(2): 1818–1824, August 2018. doi: 10.1093/mnras/sty1178.

J. D. Hadjidemetriou. Binary Systems with Decreasing Mass. *Zeitschrift für Astrophysik*, 63: 116, January 1966a.

John D. Hadjidemetriou. Two-body problem with variable mass: A new approach. *Icarus*, 2: 440–451, January 1963. doi: 10.1016/0019-1035(63)90072-1.

John D. Hadjidemetriou. Analytic Solutions of the Two-Body Problem with Variable Mass. *Icarus*, 5(1):34–46, January 1966b. doi: 10.1016/0019-1035(66)90006-6.

Zhanwen Han, Philipp Podsiadlowski, and Peter P. Eggleton. The formation of bipolar planetary nebulae and close white dwarf binaries. *Monthly Notices of the Royal Astronomical Society*, 272(4):800–820, February 1995. doi: 10.1093/mnras/272.4.800.

A. Hardy, M. R. Schreiber, S. G. Parsons, C. Caceres, G. Retamales, Z. Wahhaj, D. Mawet, H. Canovas, L. Cieza, T. R. Marsh, M. C. P. Bours, V. S. Dhillon, and A. Bayo. The First Science Results from Sphere: Disproving the Predicted Brown Dwarf Around V471 Tau. *Astrophysical Journal Letters*, 800(2):L24, February 2015. doi: 10.1088/2041-8205/800/2/L24.

Adam Hardy, Matthias R. Schreiber, Steven G. Parsons, Claudio Caceres, Carolyn Brinkworth, Dimitri Veras, Boris T. Gänsicke, Thomas R. Marsh, and Lucas Cieza. The detection of dust around NN Ser. *Monthly Notices of the Royal Astronomical Society*, 459(4):4518–4526, July 2016. doi: 10.1093/mnras/stw976.

Ronald W. Hilditch. *An Introduction to Close Binary Stars*. 2001.

Roberto Iaconi, Keiichi Maeda, Takaya Nozawa, Orsola De Marco, and Thomas Reichardt. Properties of the post in-spiral common envelope ejecta II: dust formation. *Monthly Notices of the Royal Astronomical Society*, 497(3):3166–3179, September 2020. doi: 10.1093/mnras/staa2169.

Icko Iben, Jr. and Mario Livio. Common Envelopes in Binary Star Evolution. *Publications of the Astronomical Society of the Pacific*, 105:1373, December 1993. doi: 10.1086/133321.

N. Ivanova, S. Justham, X. Chen, O. De Marco, C. L. Fryer, E. Gaburov, H. Ge, E. Glebbeek, Z. Han, X. D. Li, G. Lu, T. Marsh, P. Podsiadlowski, A. Potter, N. Soker, R. Taam, T. M. Tauris, E. P. J. van den Heuvel, and R. F. Webbink. Common envelope evolution: where we stand and how we can move forward. *Astronomy and Astrophysics Review*, 21:59, February 2013. doi: 10.1007/s00159-013-0059-2.

Natalia Ivanova. On the Use of Hydrogen Recombination Energy during Common Envelope Events. *Astrophysical Journal Letters*, 858(2):L24, May 2018. doi: 10.3847/2041-8213/aac101.

Natalia Ivanova, Stephen Justham, and Paul Ricker. *Common Envelope Evolution*. IOP Publishing, 2020. doi: 10.1088/2514-3433/abb6f0.

J. H. Jeans. Cosmogonic problems associated with a secular decrease of mass. *Monthly Notices of the Royal Astronomical Society*, 85:2, November 1924. doi: 10.1093/mnras/85.1.2.

M. Joos, P. Hennebelle, and A. Ciardi. Protostellar disk formation and transport of angular momentum during magnetized core collapse. *Astronomy & Astrophysics*, 543:A128, July 2012. doi: 10.1051/0004-6361/201118730.

Amit Kashi and Noam Soker. A circumbinary disc in the final stages of common envelope and the core-degenerate scenario for Type Ia supernovae. *Monthly Notices of the Royal Astronomical Society*, 417(2):1466–1479, October 2011. doi: 10.1111/j.1365-2966.2011.19361.x.

Rudolf Kippenhahn, Alfred Weigert, and Achim Weiss. *Stellar Structure and Evolution*. 2013. doi: 10.1007/978-3-642-30304-3.

J. Kluska, M. Hillen, H. Van Winckel, R. Manick, M. Min, S. Regibo, and P. Royer. The perturbed sublimation rim of the dust disk around the post-AGB binary IRAS08544-4431. *Astronomy & Astrophysics*, 616:A153, August 2018. doi: 10.1051/0004-6361/201832983.

J. Kluska, H. Van Winckel, Q. Coppée, G.-M. Oomen, K. Dsilva, D. Kamath, V. Bujarrabal, and M. Min. A population of transition disks around evolved stars: Fingerprints of planets. Catalog of disks surrounding Galactic post-AGB binaries. *Astronomy & Astrophysics*, 658: A36, February 2022. doi: 10.1051/0004-6361/202141690.

Veselin B. Kostov, Keavin Moore, Daniel Tamayo, Ray Jayawardhana, and Stephen A. Rinehart. Tatooine's Future: The Eccentric Response of Kepler's Circumbinary Planets to Common-envelope Evolution of Their Host Stars. *Astrophysical Journal*, 832(2):183, December 2016. doi: 10.3847/0004-637X/832/2/183.

Yoshihide Kozai. Secular perturbations of asteroids with high inclination and eccentricity. *Astronomical Journal*, 67:591–598, November 1962. doi: 10.1086/108790.

Rajika L. Kuruwita, Jan Staff, and Orsola De Marco. Considerations on the role of fall-back discs in the final stages of the common envelope binary interaction. *Monthly Notices of the Royal Astronomical Society*, 461(1):486–496, September 2016. doi: 10.1093/mnras/stw1414.

A. F. Lanza. Internal magnetic fields, spin-orbit coupling, and orbital period modulation in close binary systems. *Monthly Notices of the Royal Astronomical Society*, 491(2):1820–1831, January 2020. doi: 10.1093/mnras/stz3135.

Mike Y. M. Lau, Ryosuke Hirai, Miguel González-Bolívar, Daniel J. Price, Orsola De Marco, and Ilya Mandel. Common envelopes in massive stars: towards the role of radiation pressure and recombination energy in ejecting red supergiant envelopes. *Monthly Notices of the Royal Astronomical Society*, 512(4):5462–5480, June 2022a. doi: 10.1093/mnras/stac049.

Mike Y. M. Lau, Ryosuke Hirai, Daniel J. Price, and Ilya Mandel. Common envelopes in massive stars II: The distinct roles of hydrogen and helium recombination. *Monthly Notices of the Royal Astronomical Society*, 516(4):4669–4678, November 2022b. doi: 10.1093/mnras/stac2490.

Mike Y. M. Lau, Ryosuke Hirai, Daniel J. Price, Ilya Mandel, and Matthew R. Bate. Common envelopes in massive stars: III. The obstructive role of radiation transport in envelope ejection. *Astronomy & Astrophysics*, 699:A274, July 2025. doi: 10.1051/0004-6361/202554782.

Tim Lichtenberg and Dominik R. G. Schleicher. Modeling gravitational instabilities in self-gravitating protoplanetary disks with adaptive mesh refinement techniques. *Astronomy & Astrophysics*, 579:A32, July 2015. doi: 10.1051/0004-6361/201424528.

M. L. Lidov. The evolution of orbits of artificial satellites of planets under the action of gravitational perturbations of external bodies. *Planetary and Space Science*, 9(10):719–759, October 1962. doi: 10.1016/0032-0633(62)90129-0.

Mario Livio and Noam Soker. The Common Envelope Phase in the Evolution of Binary Stars. *Astrophysical Journal*, 329:764, June 1988. doi: 10.1086/166419.

Mario Livio, Anurag Shankar, Andreas Burkert, and James W. Truran. The Common Envelope Phase in the Outbursts of Classical Novae. *Astrophysical Journal*, 356:250, June 1990. doi: 10.1086/168836.

G. Lodato. Self-gravitating accretion discs. *Nuovo Cimento Rivista Serie*, 30:293, January 2007. doi: 10.1393/ncr/i2007-10022-x.

M. E. Lohr, A. J. Norton, D. R. Anderson, A. Collier Cameron, F. Faedi, C. A. Haswell, C. Hellier, S. T. Hodgkin, K. Horne, U. C. Kolb, P. F. L. Maxted, D. Pollacco, I. Skillen, B. Smalley, R. G. West, and P. J. Wheatley. Period and amplitude variations in post-common-envelope eclipsing binaries observed with SuperWASP. *Astronomy & Astrophysics*, 566:A128, June 2014. doi: 10.1051/0004-6361/201424027.

Michel Mayor and Didier Queloz. A Jupiter-mass companion to a solar-type star. *Nature*, 378 (6555):355–359, November 1995. doi: 10.1038/378355a0.

B. Miszalski, D. Jones, P. Rodríguez-Gil, H. M. J. Boffin, R. L. M. Corradi, and M. Santander-García. Discovery of close binary central stars in the planetary nebulae NGC 6326 and NGC 6778. *Astronomy & Astrophysics*, 531:A158, July 2011. doi: 10.1051/0004-6361/201117084.

Alexander J. Mustill, Jonathan P. Marshall, Eva Villaver, Dimitri Veras, Philip J. Davis, Jonathan Horner, and Robert A. Wittenmyer. Main-sequence progenitor configurations of the NN Ser candidate circumbinary planetary system are dynamically unstable. *Monthly Notices of the Royal Astronomical Society*, 436(3):2515–2521, December 2013. doi: 10.1093/mnras/stt1754.

J. L. A. Nandez and N. Ivanova. Common envelope events with low-mass giants: understanding the energy budget. *Monthly Notices of the Royal Astronomical Society*, 460(4):3992–4002, August 2016. doi: 10.1093/mnras/stw1266.

J. L. A. Nandez, N. Ivanova, and J. C. Jr Lombardi. Recombination energy in double white dwarf formation. *Monthly Notices of the Royal Astronomical Society*, 450:L39–L43, June 2015. doi: 10.1093/mnrasl/slv043.

Felipe H. Navarrete, Petri J. Käpylä, Dominik R. G. Schleicher, Carolina A. Ortiz, and Robi Banerjee. Origin of eclipsing time variations: Contributions of different modes of the dynamo-generated magnetic field. *Astronomy & Astrophysics*, 663:A90, July 2022. doi: 10.1051/0004-6361/202243252.

Felipe H. Navarrete, Dominik R. G. Schleicher, Petri J. Käpylä, and Marcel Völschow. Eclipsing time variations in close binaries produced by azimuthal dynamo waves. *arXiv e-prints*, art. arXiv:2604.27609, April 2026. doi: 10.48550/arXiv.2604.27609.

G. Nelemans, F. Verbunt, L. R. Yungelson, and Simon F. Portegies Zwart. Reconstructing the evolution of double helium white dwarfs: envelope loss without spiral-in. *Astronomy & Astrophysics*, 360:1011–1018, August 2000. doi: 10.48550/arXiv.astro-ph/0006216.

Sebastian T. Ohlmann, Friedrich K. Röpke, Rüdiger Pakmor, and Volker Springel. Hydrodynamic Moving-mesh Simulations of the Common Envelope Phase in Binary Stellar Systems. *Astrophysical Journal Letters*, 816(1):L9, January 2016. doi: 10.3847/2041-8205/816/1/L9.

Patrick A. Ondratschek, Friedrich K. Röpke, Fabian R. N. Schneider, Christian Fendt, Christian Sand, Sebastian T. Ohlmann, Rüdiger Pakmor, and Volker Springel. Bipolar planetary nebulae from common-envelope evolution of binary stars. *Astronomy & Astrophysics*, 660: L8, April 2022. doi: 10.1051/0004-6361/202142478.

Aykut Özdönmez, Huseyin Er, and Ilham Nasiroglu. Investigation on the orbital period variations of NN Ser: implications for the hypothetical planets, the Applegate mechanism, and the orbital stability. *Monthly Notices of the Royal Astronomical Society*, 526(3):4725–4734, December 2023. doi: 10.1093/mnras/stad3086.

B. Paczynski. Common Envelope Binaries. In Peter Eggleton, Simon Mitton, and John Whelan, editors, *Structure and Evolution of Close Binary Systems*, volume 73 of *IAU Symposium*, page 75, January 1976.

Joel Parriott and Charles Alcock. On the Number of Comets Around White Dwarf Stars: Orbit Survival During the Late Stages of Stellar Evolution. *Astrophysical Journal*, 501(1): 357–366, July 1998. doi: 10.1086/305802.

Jean-Claude Passy, Orsola De Marco, Chris L. Fryer, Falk Herwig, Steven Diehl, Jeffrey S. Oishi, Mordecai-Mark Mac Low, Greg L. Bryan, and Gabriel Rockefeller. Simulating the Common Envelope Phase of a Red Giant Using Smoothed-particle Hydrodynamics and Uniform-grid Codes. *Astrophysical Journal*, 744(1):52, January 2012. doi: 10.1088/0004-637X/744/1/52.

Hagai B. Perets. Second generation planets. *arXiv e-prints*, art. arXiv:1001.0581, January 2010. doi: 10.48550/arXiv.1001.0581.

Ali Pourmand, Devika Kamath, Orsola De Marco, and Mark Wardle. Second-generation planet formation in post-AGB discs: Testing the role of gravitational instability. *Publications of the Astronomical Society of Australia*, 42:e159, November 2025. doi: 10.1017/pasa.2025.10125.

D. Pulley, I. D. Sharp, J. Mallett, and S. von Harrach. Eclipse timing variations in post-common envelope binaries: Are they a reliable indicator of circumbinary companions? *Monthly Notices of the Royal Astronomical Society*, 514(4):5725–5738, August 2022. doi: 10.1093/mnras/stac1676.

D. Pulley, I. D. Sharp, J. Mallett, and S. von Harrach. Eclipse timing variations in 7 post-common envelope binaries: an update on recent circumbinary models. *arXiv e-prints*, art. arXiv:2507.06748, July 2025. doi: 10.48550/arXiv.2507.06748.

Thomas A. Reichardt, Orsola De Marco, Roberto Iaconi, Christopher A. Tout, and Daniel J. Price. Extending common envelope simulations from Roche lobe overflow to the nebular phase. *Monthly Notices of the Royal Astronomical Society*, 484(1):631–647, March 2019. doi: 10.1093/mnras/sty3485.

Thomas A. Reichardt, Orsola De Marco, Roberto Iaconi, Luke Chamandy, and Daniel J. Price. The impact of recombination energy on simulations of the common-envelope binary interaction. *Monthly Notices of the Royal Astronomical Society*, 494(4):5333–5349, June 2020. doi: 10.1093/mnras/staa937.

Paul M. Ricker and Ronald E. Taam. The Interaction of Stellar Objects within a Common Envelope. *Astrophysical Journal Letters*, 672(1):L41, January 2008. doi: 10.1086/526343.

Paul M. Ricker and Ronald E. Taam. An AMR Study of the Common-envelope Phase of Binary Evolution. *Astrophysical Journal*, 746(1):74, February 2012. doi: 10.1088/0004-637X/746/1/74.

Paul M. Ricker, Frank X. Timmes, Ronald E. Taam, and Ronald F. Webbink. Common envelope evolution of massive stars. In Lidia M. Oskinova, Enrico Bozzo, Tomasz Bulik, and Douglas R. Gies, editors, *High-mass X-ray Binaries: Illuminating the Passage from Massive Binaries to Merging Compact Objects*, volume 346 of *IAU Symposium*, pages 449–454, December 2019. doi: 10.1017/S1743921318007433.

Friedrich K. Röpke and Orsola De Marco. Simulations of common-envelope evolution in binary stellar systems: physical models and numerical techniques. *Living Reviews in Computational Astrophysics*, 9(1):2, December 2023. doi: 10.1007/s41115-023-00017-x.

Dongsu Ryu and Ethan T. Vishniac. The Growth of Linear Perturbations of Adiabatic Shock Waves. *Astrophysical Journal*, 313:820, February 1987. doi: 10.1086/165021.

Christian Sand, Sebastian T. Ohlmann, Fabian R. N. Schneider, Rüdiger Pakmor, and Friedrich K. Röpke. Common-envelope evolution with an asymptotic giant branch star. *Astronomy & Astrophysics*, 644:A60, December 2020. doi: 10.1051/0004-6361/202038992.

Eric L. Sandquist, Ronald E. Taam, Xingming Chen, Peter Bodenheimer, and Andreas Burkert. Double Core Evolution. X. Through the Envelope Ejection Phase. *Astrophysical Journal*, 500 (2):909–922, June 1998. doi: 10.1086/305778.

D. R. G. Schleicher, S. Dreizler, M. Völschow, R. Banerjee, and F. V. Hessman. Planet formation in post-common-envelope binaries. *Astronomische Nachrichten*, 336(5):458, June 2015. doi: 10.1002/asna.201412184.

Dominik R. G. Schleicher and Stefan Dreizler. Planet formation from the ejecta of common envelopes. *Astronomy & Astrophysics*, 563:A61, March 2014. doi: 10.1051/0004-6361/201322860.

Noam Soker, Aldana Grichener, and Efrat Sabach. Radiating the Hydrogen Recombination Energy during Common Envelope Evolution. *Astrophysical Journal Letters*, 863(1):L14, August 2018. doi: 10.3847/2041-8213/aad736.

Geoffrey Taylor. The Instability of Liquid Surfaces when Accelerated in a Direction Perpendicular to their Planes. I. *Proceedings of the Royal Society of London Series A*, 201(1065): 192–196, March 1950. doi: 10.1098/rspa.1950.0052.

Philippe Thebault and Danilo Bonanni. A complete census of planet-hosting binaries. *arXiv e-prints*, art. arXiv:2506.18759, June 2025. doi: 10.48550/arXiv.2506.18759.

Scott Tremaine. *Dynamics of Planetary Systems*. 2023.

Hans Van Winckel. Binary post-AGB stars as tracers of stellar evolution. *arXiv e-prints*, art. arXiv:1809.00871, September 2018. doi: 10.48550/arXiv.1809.00871.

Andrew Vanderburg, Saul A. Rappaport, Siyi Xu, Ian J. M. Crossfield, Juliette C. Becker, Bruce Gary, Felipe Murgas, Simon Blouin, Thomas G. Kaye, Enric Palle, Carl Melis, Brett M. Morris, Laura Kreidberg, Varoujan Gorjian, Caroline V. Morley, Andrew W. Mann, Hannu Parviainen, Logan A. Pearce, Elisabeth R. Newton, Andreia Carrillo, Ben Zuckerman, Lorne Nelson, Greg Zeimann, Warren R. Brown, René Tronsgaard, Beth Klein, George R. Ricker,

Roland K. Vanderspek, David W. Latham, Sara Seager, Joshua N. Winn, Jon M. Jenkins, Fred C. Adams, Björn Benneke, David Berardo, Lars A. Buchhave, Douglas A. Caldwell, Jessie L. Christiansen, Karen A. Collins, Knicole D. Colón, Tansu Daylan, John Doty, Alexandra E. Doyle, Diana Dragomir, Courtney Dressing, Patrick Dufour, Akihiko Fukui, Ana Glidden, Natalia M. Guerrero, Xueying Guo, Kevin Heng, Andreea I. Henriksen, Chelsea X. Huang, Lisa Kaltenegger, Stephen R. Kane, John A. Lewis, Jack J. Lissauer, Farisa Morales, Norio Narita, Joshua Pepper, Mark E. Rose, Jeffrey C. Smith, Keivan G. Stassun, and Liang Yu. A giant planet candidate transiting a white dwarf. *Nature*, 585 (7825):363–367, September 2020. doi: 10.1038/s41586-020-2713-y.

Dimitri Veras. Post-main-sequence planetary system evolution. *Royal Society Open Science*, 3: 150571, February 2016. doi: 10.1098/rsos.150571.

Dimitri Veras. Planetary Systems Around White Dwarfs. In *Oxford Research Encyclopedia of Planetary Science*, page 1. 2021. doi: 10.1093/acrefore/9780190647926.013.238.

Dimitri Veras and Christopher A. Tout. The great escape - II. Exoplanet ejection from dying multiple-star systems. *Monthly Notices of the Royal Astronomical Society*, 422(2):1648–1664, May 2012. doi: 10.1111/j.1365-2966.2012.20741.x.

Dimitri Veras, Mark C. Wyatt, Alexander J. Mustill, Amy Bonsor, and John J. Eldridge. The great escape: how exoplanets and smaller bodies desert dying stars. *Monthly Notices of the Royal Astronomical Society*, 417(3):2104–2123, November 2011. doi: 10.1111/j.1365-2966.2011.19393.x.

Dimitri Veras, John D. Hadjidemetriou, and Christopher A. Tout. An exoplanet's response to anisotropic stellar mass loss during birth and death. *Monthly Notices of the Royal Astronomical Society*, 435(3):2416–2430, November 2013. doi: 10.1093/mnras/stt1451.

Marco Vetter, Friedrich K. Röpke, Fabian R. N. Schneider, Rüdiger Pakmor, Sebastian T. Ohlmann, Mike Y. M. Lau, and Robert Andrassy. From spherical stars to disk-like structures: 3D common-envelope evolution of massive binaries beyond inspiral. *Astronomy & Astrophysics*, 691:A244, November 2024. doi: 10.1051/0004-6361/202451579.

M. Völschow, R. Banerjee, and F. V. Hessman. Second generation planet formation in NN Serpentis? *Astronomy & Astrophysics*, 562:A19, February 2014. doi: 10.1051/0004-6361/201322111.

M. Völschow, D. R. G. Schleicher, V. Perdelwitz, and R. Banerjee. Eclipsing time variations in close binary systems: Planetary hypothesis vs. Applegate mechanism. *Astronomy & Astrophysics*, 587:A34, March 2016. doi: 10.1051/0004-6361/201527333.

R. F. Webbink. Double white dwarfs as progenitors of R Coronae Borealis stars and type I supernovae. *Astrophysical Journal*, 277:355–360, February 1984. doi: 10.1086/161701.

E. C. Wilson and J. Nordhaus. The role of convection in determining the ejection efficiency of common envelope interactions. *Monthly Notices of the Royal Astronomical Society*, 485(4): 4492–4501, June 2019. doi: 10.1093/mnras/stz601.

E. C. Wilson and J. Nordhaus. Convection and spin-up during common envelope evolution: the formation of short-period double white dwarfs. *Monthly Notices of the Royal Astronomical Society*, 497(2):1895–1903, September 2020. doi: 10.1093/mnras/staa2088.

E. C. Wilson and J. Nordhaus. Convection reconciles the difference in efficiencies between low-mass and high-mass common envelopes. *Monthly Notices of the Royal Astronomical Society*, 516(2):2189–2195, October 2022. doi: 10.1093/mnras/stac2300.

A. Wolszczan and D. A. Frail. A planetary system around the millisecond pulsar PSR1257 + 12. *Nature*, 355(6356):145–147, January 1992. doi: 10.1038/355145a0.

Zepei Xing, Santiago Torres, Ylva Götberg, Alessandro A. Trani, Valeriya Korol, and Jorge Cuadra. Combining REBOUND and MESA: dynamical evolution of planets orbiting interacting binaries. *Monthly Notices of the Royal Astronomical Society*, 537(1):285–292, February 2025. doi: 10.1093/mnras/stae2820.

Harold W. Yorke, Peter Bodenheimer, and Ronald E. Taam. Double Core Evolution. VIII. The Spiral-in of a Main-Sequence Star through the Envelope of an Asymptotic Giant Branch Companion. *Astrophysical Journal*, 451:308, September 1995. doi: 10.1086/176220.

M. Zorotovic and M. R. Schreiber. Origin of apparent period variations in eclipsing post-common-envelope binaries. *Astronomy & Astrophysics*, 549:A95, January 2013. doi: 10.1051/0004-6361/201220321.